UNIVERSIDAD NACIONAL AUTÓNOMA DE MÉXICO

PROGRAMA DE POSGRADO EN ASTROFÍSICA

INSTITUTO DE RADIOASTRONOMÍA Y ASTROFÍSICA

LOW SURFACE BRIGHTNESS GALAXIES IN THE ILLUSTRIS-TNG SIMULATION

PARA OPTAR POR EL GRADO DE
DOCTOR EN CIENCIAS (ASTROFÍSICA)

PRESENTA
LUIS ENRIQUE PÉREZ MONTAÑO

TUTOR
DR. BERNARDO CERVANTES SODI
IRyA

Morelia, México. Marzo de 2023

"The most I know about Astronomy, the most I believe in Good..."
Heber Doust Curtis

To those who were with me since the beginning of this adventure, to those who arrived, and those who left...

Aknowledgements

- To God, for all the blessings he has given me throughout my life, because he has allowed me to get to this day, and because he has never left me alone in this great adventure of life.

- To my parents, Sandra and Alejandro, and my sister Raquel, for all their support even far away from home.

- To my grand parents, Sergio, Ofelia, Everardo and Marcelina. Because even with the difficulties we have gone through as a family, they never stop giving me their love.

- To Bernardo Cervantes Sodi and Vicente Rodriguez Gómez, for their total support from the first day we met, and for all the trust placed in me during the completion of this work. For their guidance trough these years, and in addition to being excellent advisors, they have become strong collaborators and valuable friends.

- To Annalisa Pillepich, the Max Planck Institute for Astronomy, and the Max Planck Computing and Data Facility, for the facilities granted for access to computational resources, essential for the development of this work.

- To Yannick Bahé, Qirong Zhu, Yetli Rosas-Guevara, Gaspar Galaz and Miguel Aragón-Calvo, as well as the evaluating committee assigned for the defense of this thesis, Ricardo Chávez Murillo, Simon Kemp and Rosa González, for their very useful comments that allowed the improvement of the quality of this work.

- To the National Council of Science and Technology (CONACyT), for the support received through these years of postgraduate studies through their scholarship program.

- To the Support Program for Research and Technological Innovation Projects (PAPIIT) with reference number IA103520 from Dirección General de Asuntos del Personal Académico (DGAPA- UNAM), for the financial support provided during the completion of this project.

- To my second family in Puebla, my girlfriend Elda Vela, my friends Yessica Espinoza, José Alfredo Letras and Sergio Carranza. To Prof. Jorge Eduardo Araiza Rivera and his beloved family. Because despite the distance, for many years they have given me their support at important moments, and because they are a role model of discipline and constant work.

- To the wonderful third family I've done in Morelia, Natalia Osorio, Rudy Rivera, Rubén Guerrero, Palmira Jimenez and Solanyely Ramírez. And the ones who flew away chasing their dreams, Alejandro López Vázquez and Anibal Sierra Morales.

- To the Institute of Radioastronomy and Astrophysics, for providing me all the scientific tools, resources and support needed to be here today.

Contents

List of Figures

List of Tables

Abstract

We explore the nature of low surface brightness galaxies (LSBGs) in the hydrodynamic cosmological simulation TNG100 of the Illustris project, selecting a sample of LSBGs with an $r-$band central surface brightness $\mu > 22.0$ mag/arcsec^2 at $z = 0$ over a wide range of stellar masses ($M* = 10^9 - 10^{12}$M$_\odot$). Even when some state-of-the-art cosmological simulations have been employed in the past to study the galaxy population of LSBGs, this is the first time a complete study is performed employing TNG100 not only in a particular example, but extending the robustness of our results with the employment of a large sample of simulated galaxies. We found that, as a population, LSBGs are systematically less massive and more extended than high surface brightness galaxies (HSBGs), displaying mostly late-type morphologies according to a kinematic criterion. At fixed stellar mass, we find that LSBGs have systematically higher stellar specific angular momentum and halo spin parameter values when compared with HSBGs, as suggested by previous works reinforcing the importance of the high angular momentum and the spin parameter in the determination of galaxy properties such as gas fractions and characteristic sizes, as well as the spatial distribution of star formation processes and black hole accretion rates. We tracked the evolution of these quantities back in time, finding that the spin parameters λ of the haloes hosting LSBGs and HSBGs exhibit a clear bifurcation at $z \sim 2$, finding an interesting cause-consequence relation in which the change in the spin parameter causes a similar separation in the evolutionary tracks of the other properties, such as galactic angular momentum and effective radius, resulted in the values observed at $z = 0$. Putting all these results together in a cosmological context, we can provide a good explanation for the global properties observed in LSBGs, which are in good agreement with one of the two main mechanisms proposed to form LSBGs in the literature, in which the higher values of specific angular momentum and halo spin parameter seem to be responsible for their extended nature.

Based on the premise that the differences in the surface brightness can be not only a consequence of variations in the halo spin parameter, but also variations in their density profiles, we contrast these differences in λ with other properties of the dark matter halos hosting LSBGs and comparing them with the ones hosting HSBGs. We found no significant differences in the halo concentration index c_{200} of both population of galaxies, but we found that most of the galaxies in our sample are found in halos with spherical geometries, with a larger departure from spherical halos in HSBGs than in the case of LSBGs. We also found that the angular momentum vectors of the stellar (j_*) and dark (j_{200}) components are strongly aligned in the case of LSBGs, in agreement with previous theoretical studies. This result could be interpreted as follows: aligned components will favor a scenario in which the total angular momentum is highly conserved, while a misalignment will imply that most of the total specific angular momentum will be 'lost' due to the angular momentum components pointing in opposite directions.

A limited number of studies related with the connection between the properties of LSBGs and the environment around them can be found in the literature. Most of these studies are biased to study the environment at one of the following scales: going from the smallest scales comparable with galaxy halos, LSBGs within galaxy groups, or the characterization of the large-scale structure of the Universe. This limitation makes difficult to find an overlap between the main conclusions of such studies, but in this work, we employ TNG100 together with other tools to study the environment covering the previously mentioned scales, which allowed us to have a wider perspective of the environment around these galaxies. We characterized the environment in which LSBGs reside by studying their relative abundance within groups, finding a lack of LSBGs at the center of galaxy clusters, specially at high masses, implying that LSBGs are

either not formed in the center of galaxy clusters, or they are destroyed once they reach the central regions. We study the overdensity field finding that LSBGs with spiral morphology are preferentially found in low-density environments, while elliptical LSBGs are more abundant in high-density environments, where mergers, tidal interactions and ram-pressure stripping phenomena are responsible for their nature. We complement this study by computing the two-point correlation function $\xi(r)$, finding that LSBGs are less clustered than HSBGs, reflected in the amplitude of $\xi(r)$. These changes in the amplitude of $\xi(r)$ are mainly due to the fact that spiral LSBGs are the ones that dominate the low-density regime, whereas elliptical LSBGs are more likely to reside in high-density environments, mainly on scales comparable with the so-called 'one-halo' term (i.e. LSBGs are less clustered within a given halo). We finally explored the large scale structure around the galaxies in our sample, finding no significant differences in the distance to the closest large-scale structure pattern of the cosmic web, but in counted exceptions. This suggests that the large-scale structure of the Universe has not a strong impact on the mechanisms that favor the evolution of LSBGs. By contrast, the local environment comparable with the size of galaxy clusters seems to have a stronger impact, mostly driven by the presence or absence of important interaction phenomena, such as galaxy mergers and tidal stripping, as well as stellar and gas accretion. Our results are able to complement previous studies, providing a better understanding not only of the secular processes that form LSBGs, but also on the impact of the environment in which these galaxies are formed, and at which scales are the ones that have a greater impact on the mechanisms that give origin to this type of galaxies.

Publications

Main papers of thesis work:

1. **The formation of low surface brightness galaxies in the IllustrisTNG simulation.**
Authors: **L.E. Pérez-Montaño**, V. Rodriguez-Gomez, B. Cervantes Sodi, Q. Zhu, A. Pillepich, M. Vogelsberger and L. Hernquist. Monthly Notices of the Royal Astronomical Society, Volume 514, Issue 4, pp. 5840-5852 (2022).

2. **Environmental effects on Low Surface Brightness Galaxies in the IllustrisTNG simulation**
Authors: **L.E. Pérez-Montaño**, B. Cervantes Sodi, V. Rodriguez-Gomez, T.B.D, in preparation.

Collaborative papers related to thesis topic:

1. **Giant Low Surface Brightness Galaxies in TNG100.**
Authors: Q. Zhu, **L.E. Pérez-Montaño**, V. Rodriguez-Gomez, B. Cervantes Sodi, J. Zjupa, F. Marinacci, M. Vogelsberger and L. Hernquist (submitted).

2. **Galactic angular momentum in the IllustrisTNG simulation – I. Connection to morphology, halo spin, and black hole mass.**
Authors: V. Rodriguez-Gomez, S. Genel, S. M. Fall, A. Pillepich, M. Huertas-Company, D. Nelson, **L.E. Pérez-Montaño**, F. Marinacci, R. Pakmor, V. Springel, M. Vogelsberger and L. Hernquist. Monthly Notices of the Royal Astronomical Society, Volume 512, Issue 4, pp. 5978-5994 (2022).

3. **On the environment of low surface brightness galaxies at different scales.**
Authors: **L.E. Pérez-Montaño** and B. Cervantes Sodi. Monthly Notices of the Royal Astronomical Society, Volume 490, Issue 3, pp. 3772-3785 (2019).

Chapter 1

Introduction

1.1 How to classify galaxies?

In a general way, galaxies could be defined as an association of stars, gas, dust, and dark matter interacting under the action of gravity. These objects are observed in the sky as diffuse, extended objects with different sizes and morphologies. The easiest and most common way to classify galaxies is the one introduced by Hubble (1926), who proposed a classification based on their physical shape, considering their symmetry and the brightness of their inner region. This way to classify galaxies is also known as *The Hubble Sequence*, in which galaxies are divided into two main types:

i) Elliptical galaxies, characterized by an spherical/elipsoidal form.
ii) Spiral galaxies, identified by a disk structure with the presence of spiral arms and a central bulge. Spiral galaxies could also be sub-classified according to the presence or absence of stellar bars.

This Hubble Sequence can be visualized in Fig. 1.1 in which objects in the left-hand side are known as 'early-type' galaxies, while in the right-hand side we find the 'late-type' galaxies. This denomination was, at the beginning, based on the idea that this scenario represented an evolutionary scheme of galaxies, in which elliptical galaxies evolve becoming spiral-like galaxies. Nowadays it has been discarded that the Hubble's sequence corresponds to an evolutionary scheme, but the astronomers keep this 'convention' up to date when refering to 'early-type' (ellipticals) or 'late-type' (spirals) galaxies. It should be highlighted that irregular galaxies were not included in the original Hubble Sequence. An "upgraded" version of the Hubble's sequence was developed by de Vaucouleurs (1959), which includes an extended description to the original notation of Hubble's original sequence but considering other morphological characteristics: galactic bars, stellar rings, the geometry of spiral arms and the size of the central bulge.

Even when both classifications are commonly invoked when galaxy classifications are required, galaxies are presented in a wide range of physical and observational properties, such as their stellar mass, color, luminosity, interstellar medium density, size, and more. Taking this into account, it is convenient to replace these qualitative measurements with quantitative ones to understand the physics of galactic structure. Some of these quantitative properties are found to be directly related with their morphology. For example the infrared emission of the stellar populations varies with their morphology as a consequence of the ages of their stars (Pahre et al., 2004), given that the stars in early-type galaxies are older than in the case of late-type galaxies. Similarly the fraction of the infrared emission due to the dust goes from 10% for early-type galaxies to 90% in late-type galaxies, due to the increasing number of dust particles and PAHs (Polycyclic Aromatic Hydrocarbons). Moreover, when analyzing the color of galaxies, it has been observed that early-type galaxies are redder than late-type galaxies given that spiral galaxies tend to have more recent star formation than ellipticals.

A detailed discussion related with the dependence of these quantitative properties of galaxies and their dependence with morphology is highlighted in a review by Roberts & Haynes (1994), in which the

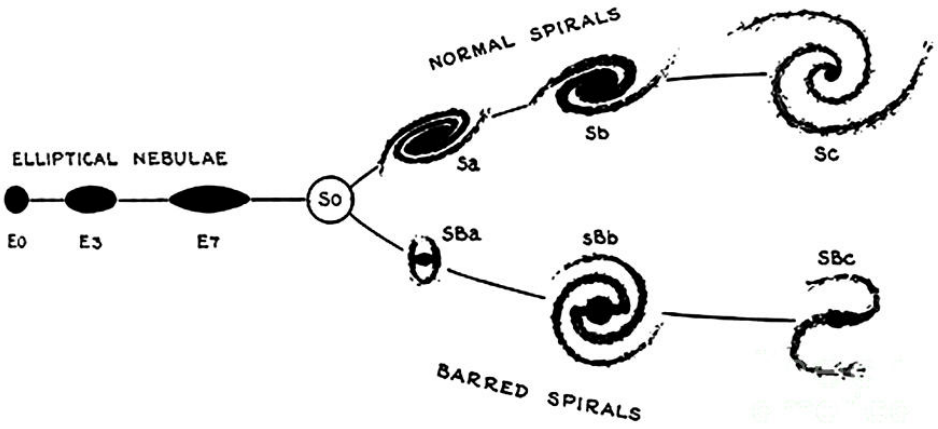

Figure 1.1: Basic scheme of the Hubble Sequence. [Credit: R.G. Abraham, Institute of Astronomy, University of Cambridge, UK.]

authors perform a complete census of the galaxy population in a flux-limited sample which include three main galaxy types: elliptical (E's), spirals (S's) and lenticular (S0's) galaxies. The main conclusions of this review are presented in Fig. 1.2. The first and second row, shows the linear radius $R_{\rm lin}$ and the B-band luminosity L_B as function of the morphological type, in which the morphology sequence is ordered, from left to right, from early-type to late-type galaxies. We observe a variation in the median (filled symbols) size and luminosity, where spiral galaxies tend to become larger and brighter as they "become" later. However elliptical galaxies are systematically larger and brighter than most of those with spiral morphology, while late-type dwarfs (Scd-Im) become smaller and fainter. Analogously the third row of Fig. 1.2 shows the variation in the total HI mass with morphology, in which it is observed that E's and S0's galaxies contain proportionately lower HI masses with respect to spirals, and the distribution of HI content is wider than in the case of spirals, indicating that some E's and S0's can be as "gas-rich" as some Sb-Sc galaxies, mainly in their outskirts, probably as a result of tidal interactions or the infall of a dwarf companion. Finally the fourth row of Fig. 1.2 shows the color index $(B-V)$ vs morphology, in which E and S0 galaxies are clearly redder than their spiral counterparts with a monotonic trend from red to blue galaxies, which is a measure of the past and present star formation activity.

However, galaxies can be classified not only by their morphology and the properties associated to it. Even when the Hubble's Sequence is a very useful and common tool, there are many other ways in which galaxies could be classified, especially if we consider only observational data. These observations are strongly influenced by the wavelength in which the instruments are calibrated to observe, and the information of the physical phenomena that can be extracted from them. For example, according to the number of stars that are formed within galaxies in a given time-scale, that is, their Star Formation Rate (SFR), galaxies can be classified as *Star Forming* or *quiescent*. To do so, it is common to employ the H_α lines, which are good tracers of photoionized regions associated to young stars emitting UV photons, as well as the infrared emission around hot stars. Another way to classify galaxies is according to their emission spectra, which combined with the observed emission of their inner regions, allows us to identify *Active Galactic Nuclei* (AGNs). It is well known that most galaxies host a supermassive black hole at their center[1], and when gas around this compact object falls towards it due to the gravity, it forms and accretion disk. The gas is heated and emits a huge amount of energy reflected in a very luminous component with high variability, present in a very short time scale. These AGNs can be identified not only by their optical luminosity or the strength and the width of their emission lines, but also by the emission associated to the different components of AGNs, such as the hot corona (X-ray emission at 64

[1]This may not be true, especially for the case of dwarf galaxies. Some dwarfs with $M_* \gtrsim 10^7 {\rm M}_\odot$ have been reported with black hole detections. A detailed review on this can be found in Reines (2022).

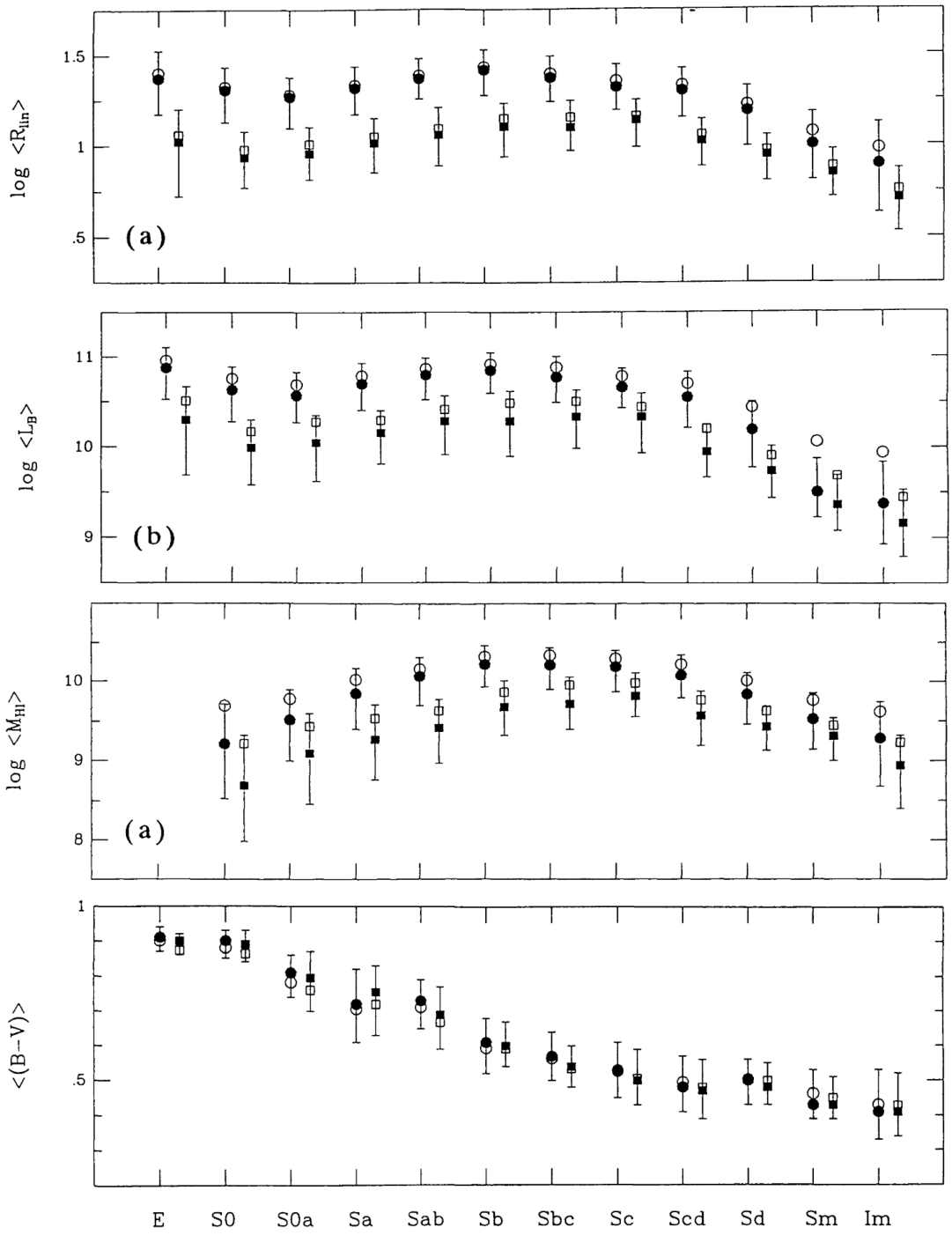

Figure 1.2: Galaxy parameters vs morphological type of the galaxies in the two galaxy samples employed by Roberts & Haynes (1994), which include galaxies of the 'Third Reference Catalogue of Bright Galaxies' (de Vaucouleurs et al., 1991), the 'Uppsala General Catalogue' (Nilson, 1973) and a private catalog. Filled and open symbols represent the median and mean values of the given property, respectively, and the error bars indicate the 25^{th} and 75^{th} percentiles. [Credit: Roberts & Haynes (1994)]

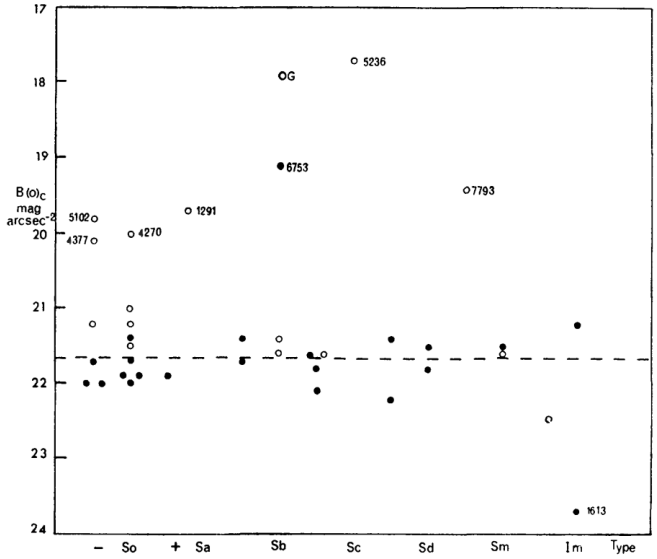

Figure 1.3: Central surface brightness of the galaxies in the galaxy sample of Freeman (1970). Dotted-line indicates the $\mu_B = 21.6$ mag arcsec^{-2} threshold. [Credit: Freeman (1970)]

keV), the torus mainly composed by dust (infrared), and the radio emission due to the collimated jets, formed by relativistic particles interacting with the circumgalactic medium.

In the current work, we will focus on a particular way to characterize galaxies related with a property associated to extended sources. This quantity is known as the "surface brightness", which is generally defined as the luminosity per unit of area (delimited by a aperture) of an extended source. In this chapter, we will provide a detailed description of how the surface brightness of a galaxy is defined, and the main differences associated with the different sub-types of galaxies that can be identified based on their surface brightness.

1.2 Surface Brightness

For the case of spiral galaxies, the brightness distribution $I(R)$ typically exhibits two main components: first, a component to the bulge that can be described as a potential profile of the form

$$\log(I) \propto R^{1/n}, \tag{1.1}$$

in which n is known as *Sérsic's index*, and it's equal to 4 for a classical spheroidal bulge (also known as *de Vaucouleurs' profile*), and takes values between 1-2 if we consider a pseudo-bulge. On the other hand, the brightness of the component associated to the disk follows an exponential profile

$$I(R) = I_0 e^{-\alpha R}, \tag{1.2}$$

where I_0 is a constant, and α the scale-length of the disk. In a general form, we can define the 'central' surface brightness as the apparent magnitude enclosed by a given aperture centered on an extended source, such as a galaxy or a nebula, per unit of area. Considering that magnitudes in astronomy are defined over a logarithmic scale, the central surface brightness density μ can be observationally obtained in its general form as

$$\mu = m + 2.5 \log_{10} A, \tag{1.3}$$

m being the apparent magnitude of the object of interest, and A, the effective area subtended by the object in the sky plane, in units of arcsec^{-2}. Contrary to the case of stars, which are observed as point sources, galaxies distribute their brightness over larger areas. Therefore, assuming that a star and a galaxy have the same apparent magnitude, this later will be more difficult to detect. One of the advantages of defining the central surface brightness, is that eq. 1.3 can be applied to any extended object regardless of its morphology, i.e., implementing eq. 1.3 does not restrict the identification of LSBGs to disk galaxies, as also early-type and irregular galaxies can fall into the surface brightness range that defines LSBGs.

The existence of low surface brightness galaxies (LSBGs) was first speculated by Disney (1976) after Freeman (1970) reported that the majority of the galaxies in his sample, in which all of them were spirals with measurable disk brightness, shared very nearly the same surface brightness in the $B-$band, with values around $\mu_B = 21.65$ mag arcsec^{-2}, independently of the morphology and the absolute magnitude of such galaxies, as indicated in Fig. 1.3. Moreover, this central surface brightness was found to be independent of the distance. Disney (1976) argued that this finding was due to a severe selection bias, and that there should be galaxies with lower surface brightness, comparable to that of the night sky. Later observational work (McGaugh, Bothun & Schombert 1995) confirmed the existence of such galaxies, popularizing the term 'LSBG' for galaxies fainter than a specified central surface brightness value. It is important to point out that Freeman (1970) employed an inward extrapolation of the exponential profile in eq. 1.2 rather than the central surface brightness of eq. 1.3, but the $\mu_B = 21.65$ mag arcsec^{-2} threshold is still the canonical value employed throughout the literature to identify the LSBGs population. In the present work, we will not restrict ourselves to objects with exponential light profiles, but rather include all light profiles in a general operational definition of LSBGs, as presented in sec. 2.2, where the central surface brightness is computed within the effective radii of the galaxy; in this way, including galaxies of all morphological types.

1.3 Main properties of LSBGs

1.3.1 Angular Momentum and Spin Parameter

Since the early 50's, it is well known that rotation in galaxies is a key parameter in cosmology (von Weizsäcker 1951; Gamow 1952) towards the understanding of the initial conditions involved in galaxy formation. It has been suggested that angular momentum could have been imprinted to early proto-galaxies from the interaction with gravitational tides coming from any other massive close system, according to the *Acquisition theory* proposed by Hoyle (1951).

Following Hoyle (1951); Peebles (1971) and Efstathiou & Barnes (1984), suppose an early Universe in which proto-galaxies acquire angular momentum via tidal torques exerted by other proto-galaxies, and let Q be the cuadrupole of a system drawn from a multipole expansion of a given mass distribution. If another proto-galaxy of mass M at a distance r on the direction θ (with respect to the z axis) produces a tidal force over the system, then the exerted torque is given by

$$\tau = \frac{3}{4}\frac{GMQ}{r^3}\sin 2\theta = \frac{dL}{dt}, \tag{1.4}$$

in which we observe that all the terms in eq. 1.4 are constant. Therefore, the torque τ is also a constant and the angular momentum is given by

$$L(t) = \tau t. \tag{1.5}$$

The values found for L are important because it corresponds to the amount of angular momentum imparted to the galaxy in this acquisition model. An auxiliary quantity that allows us to measure the angular momentum of a galaxy is known as the *Spin Parameter*, which quantifies the rotational support of a system, as the ratio between the centripetal and gravitational acceleration. Let

$$\lambda^2 \sim \frac{\text{centripetal acceleration}}{\text{gravitational acceleration}} = \frac{v^2}{r}\frac{r^2}{GM}. \tag{1.6}$$

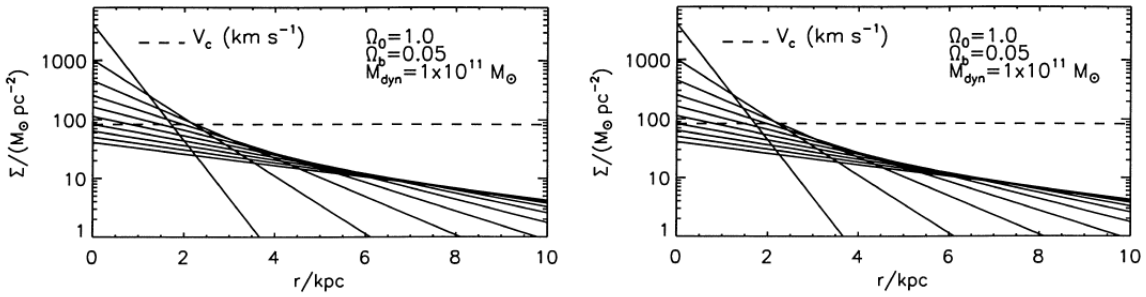

Figure 1.4: $\Sigma - r$ relation computed by Jimenez et al. (1998), for disk galaxies immersed in DM halos of different mass. From the top to bottom, the solid lines correspond to $\lambda = 0.01$ to 0.1, in steps of 0.01. It can be observed that, the higher the value of λ, the lower the slope in the $\Sigma - r$ relation, that is, galaxies with high λ have lower stellar densities and larger radii. At fixed circular velocity (indicated by the dashed line), the higher the radius, the higher the angular momentum, which is characterized by the spin parameter. [Credit: Jimenez et al. (1998)]

If M is the dynamical mass of the system, multiplying and dividing this expression by M^4G, and considering that the angular momentum and gravitational energy are $L = Mrv$ and $E = \frac{GM^2}{r}$, respectively, then eq. 1.6 can be written as

$$\lambda = \frac{L|E|^{1/2}}{GM^{5/2}}. \tag{1.7}$$

This definition was initially proposed by Peebles (1971) employing numerical models in which, the larger the cutoff radius in which stellar particles are considered part of a given system, the larger is the value of λ. This allows us to conclude that an important fraction of the angular momentum of the halo is transferred to the disk during the galaxy formation process.

In a hierarchical galaxy formation model, the halo growth is not affected by the baryonic components, but they do affect how the halo is assembled, such that the cooling gas is accumulated in the center of each halo until it produces an independent and self-gravitating system, capable of forming stars. In galaxy formation models for disk systems, such as Mo, Mao & White (1998), where the mass and angular momentum of the stellar component are a constant fraction of that of the halo, for a thin disk supported by rotation and with an exponential density profile embedded in a DM halo with an isothermal density profile, galaxy properties such as the mass of the disk M_d, the central surface density Σ_0 and the scale radius R_d depend on the mass and angular momentum fractions, the Hubble function $H(z)$ and the spin parameter λ. In particular, at fixed z stellar disks are ~ 2 times larger and 25% less dense in galaxies with large spin parameter ($\lambda \gtrsim 0.05$).

It has been found that LSBGs differ from their 'High' Surface Brightness counterparts (HSBGs) because they are formed within halos with high spin parameter, and as a consequence, the low surface brightness is a consequence of the low stellar density of the disk due to their high spin parameter. Jimenez et al. (1998), employing semi-analytical models of galaxy formation, found that the properties of LSBGs such as their color, chemical abundances and brightness profile are well adjusted by those models in which the spin parameter is higher than in HSBGs. Fig. 1.4 shows the surface density of a disk at $z = 0.7$ for two halos of different mass. Solid lines correspond to the $\Sigma - r$ relation for different values of the spin parameter, from 0.01 to 0.1. It is observed clearly that halos with high λ have a lower surface density and larger radii, such as the case of LSBGs. Given that $\Sigma_0 \propto \lambda^{-2}$, as found by Mo, Mao & White (1998), some authors such as Jimenez et al. (1998) suggest $\lambda > 0.06$ for LSBGs. Therefore, a variation in λ between 0.04 and 0.1 corresponds to a factor of 6.25 in Σ_0, equivalent to 2 mag in surface brightness above the standard threshold of Freeman (1970), i.e. $\mu_B \sim 23.6$ mag arcsec^{-2}.

With the aid of idealized hidrodynamical simulations, Kim & Lee (2013) investigated the correlation between the gas and stellar surface densities on a galactic disc and the spin parameter of the halo. Fig. 1.5 shows the results of those simulations for a galaxy in a halo of $2.3 \times 10^{11} M_{\odot}$ over an evolution time of 1.49 Gyrs. Colored scale corresponds to the surface density of the gas of a galaxy, for different values of the spin parameter. This figure shows clearly that the higher the value of λ, the larger the size of the disk, indicating that a galaxy within a halo with high angular momentum spreads its components over a larger area. For a fixed baryonic fraction $f_b = (M_* + M_{gas})/M_{tot}$, those galaxies with high spin parameters re-distribute their stars up to larger radii, and as a consequence, their surface brightness is lower.

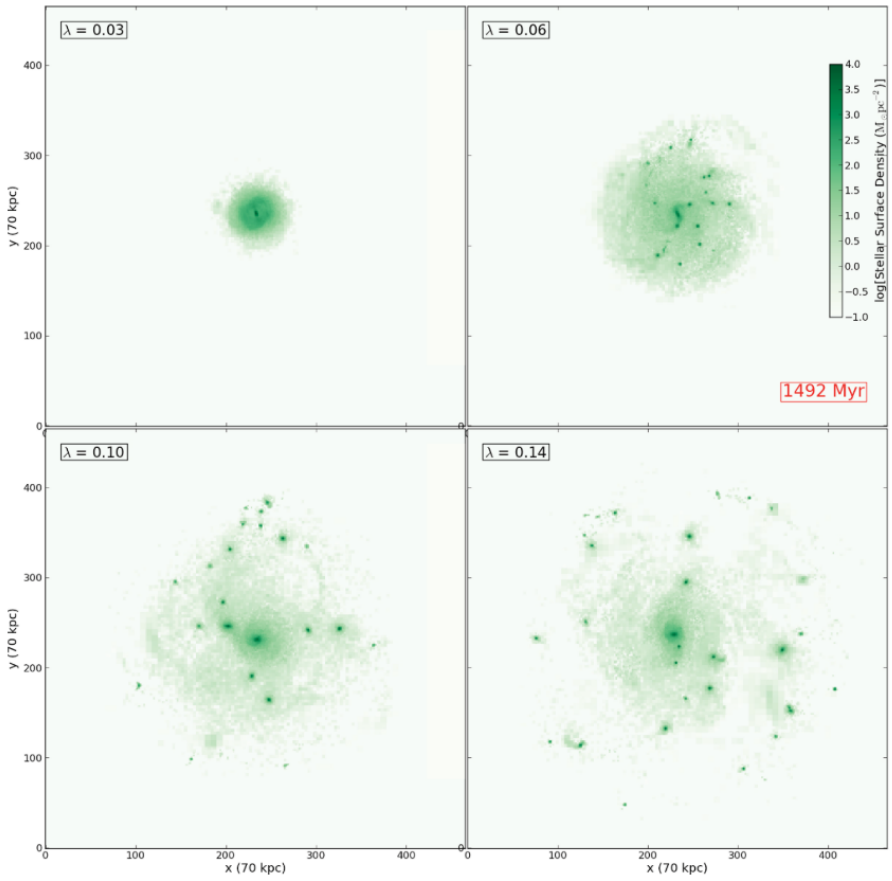

Figure 1.5: Idealized simulations that show the surface density map for 4 galaxies with different spin parameter values ($\lambda = 0.03, 0.06, 0.1, 0.14$). It is observed that for a fixed baryonic mass fraction, the larger the value of λ, galaxies spread their stars over a wider area. [Credit: Kim & Lee (2013)]

Aditionaly, Kim & Lee (2013) found a correlation between the mean stellar surface density Σ_* and the cut-off radius R_c, defined as the distance where the stellar density drops below 0.1 $M_{\odot} pc^{-2}$. The left-hand panel of Fig. 1.6, shows the azimuthaly averaged stellar surface density as a function of the radius, for galaxies with four different values of λ. It is observed that the cut-off radius of these galaxies is larger for galaxies with higher spin parameter. Moreover, the right-hand panel of Fig. 1.6 shows that the cut-off radius (red-colored lines) is increased, and the stellar surface density (blue-colored lines) decreases, for increasing values of the spin parameter, independently of the baryonic fraction within each halo, represented by dashed and dotted lines.

More recently, Pérez-Montaño & Cervantes Sodi (2019) constructed a volume-limited sample of

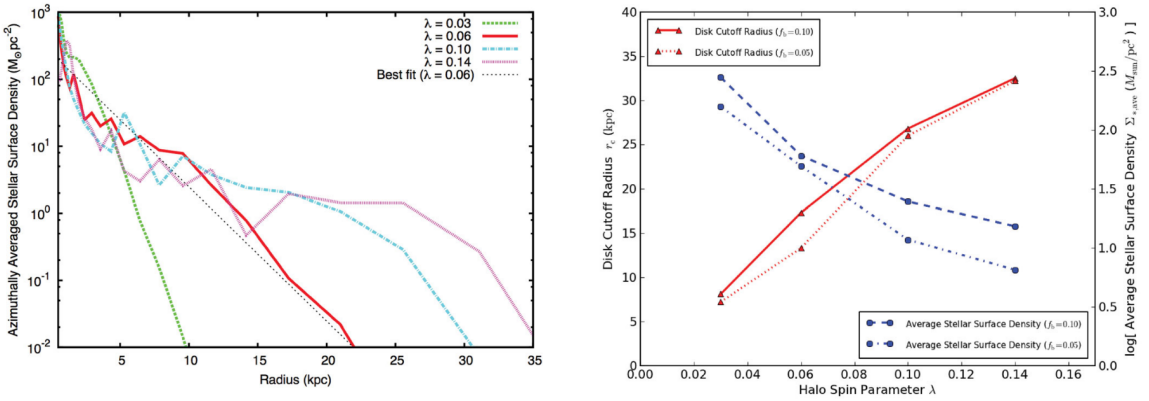

Figure 1.6: *Left panel:* Mean stellar surface density for different values of λ. For high values of the spin parameter, the stellar density drops below a critical value of 0.1 $M_\odot$ pc^{-2} at larger radii. *Right panel:* Correlations with λ for different baryonic mass fractions. Red and blue lines indicate the cut-off radius and the mean stellar density, respectively. The higher the value of λ, the larger the cut-off radius and the lower the stellar surface density. [Credit: Kim & Lee (2013)]

galaxies drawn from the SDSS DR7, including galaxies with an r-band absolute magnitude brighter than -19.8 mag, within a redshift range of $0.01 < z < 0.1$, and nearly face-on to avoid dust extinction. In such work, we calculated the stellar specific angular momentum j_* of the galaxies following the Romanowsky & Fall (2012) models for a bulge+disk decomposition, in which rotation velocities were obtained adopting a Tully-Fisher relation. At fixed stellar mass, we found that LSBGs have larger values of j_* when compared to HSBGs, as shown in Fig. 1.7. Moreover, we employed j_* as a proxy of the specific angular momentum of the dark matter component to estimate the spin parameter of the halos in which LSBGs reside, with an equivalent definition for λ proposed by Hernandez & Cervantes-Sodi (2006), which depends on the rotation velocity, the specific angular momentum and the DM halo mass. Five different and independent estimations of the halo mass are employed to calculate λ, finding that LSBGs present systematically higher spin parameters (about a factor of $1.6 - 2$) than HSBGs, regardless the estimation employed. Fig. 1.8 shows the resulting distributions of λ for LSBGs (red) and HSBGs (black) for four of the five different estimations employed in the volume-limited sample of Pérez-Montaño & Cervantes Sodi (2019), in which we observe that LSBGs present systematically higher values of their spin parameter than HSBGs. We repeated this procedure over a control sample which includes direct HI kinematic data drawn from ALFALFA (Haynes et al. 2018), finding similar trends. In a recent work performed by Salinas & Galaz (2021), the authors studied the differences in the specific angular momentum and the spin parameter of LSBGs and HSBGs drawn from SPARC (Lelli, McGaugh, & Schombert 2016b). SPARC includes well-resolved rotation curves as well as the gas distribution through the galaxies, allowing the dark matter halos to be easily adjusted. The authors fitted the dark matter halos to three different halo mass models: a NFW (Navarro, Frenk, & White 1996), an Einasto (Einasto 1965) and a DC14 (Di Cintio et al. 2014) profile. Then they implemented two different models to compute the specific angular momentum of the disks. The first assumes that the specific angular momentum of the disk is equal to the halo (classic disk formation model), and the second is a biased collapse model in which the stellar-to-halo angular momentum ratio f_j correlates with the star formation efficiency $f_* = M_*/M_h$. In the latter model, Salinas & Galaz (2021) found that the spin parameter distribution of LSBGs peaks at higher values (about a factor of 2, as found in Pérez-Montaño & Cervantes Sodi 2019) when compared to HSBGs.

1.3.2 Gas Content

For the case of spiral galaxies, the *Tully-Fisher Relation* (Tully & Fisher 1977) is a scaling relation between the maximum rotation velocity v_{max} and the luminosity L of a given galaxy expressed as

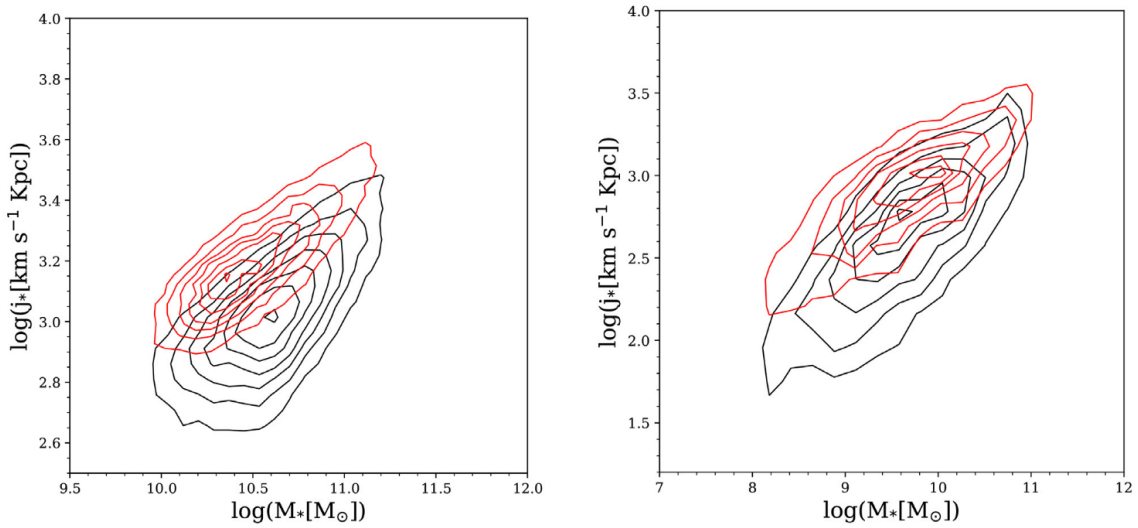

Figure 1.7: *Left panel:* Density contours of the specific angular momentum j_* as a function of stellar mass M_* for LSBGs (red) and HSBGs (black) galaxies in a volume-limited sample. *Right panel:* Same density contours but for a control sample of galaxies with similar stellar mass distribution, in which velocities are drawn directly from HI kinematic data. [Credit: Pérez-Montaño & Cervantes Sodi (2019)]

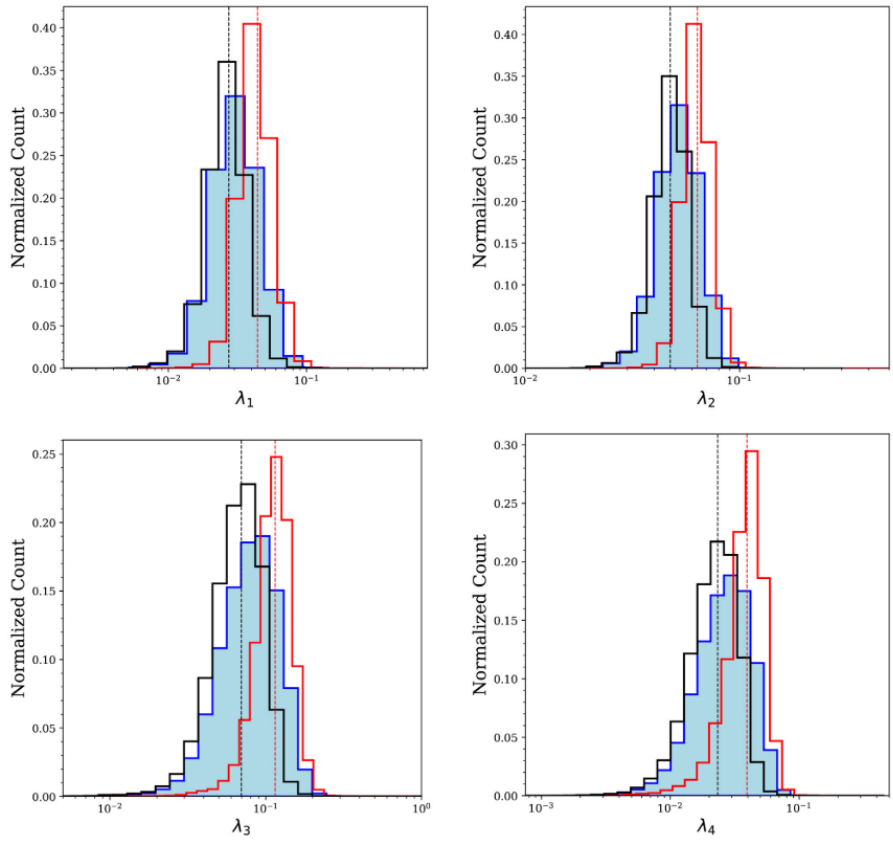

Figure 1.8: Spin distributions for a volume-limited sample, for four different dark matter halo mass estimations. The dashed line corresponds to the mean value of λ for LSBGs (red) and HSBGs (black). The blue-shaded region corresponds to the full distribution of λ. [Credit:Pérez-Montaño & Cervantes Sodi (2019)]

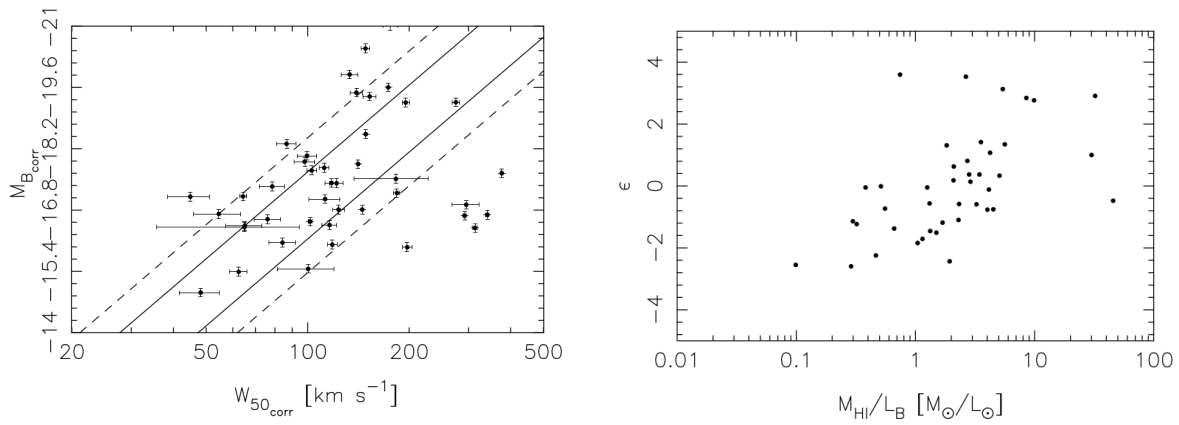

Figure 1.9: *Left panel:* Tully-Fisher relation of the galaxies in the LSBGs sample of O'Neil et al. (2000). Solid and dashed lines represent the 1σ and 2σ fits to a Tully-Fisher relation. *Right panel:* Correlation found between the residuals ε around the Tully-Fisher relation and the HI gas fraction. [Credit: O'Neil et al. (2000)]

$$L \propto v^{\alpha}{}_{max}, \tag{1.8}$$

where the slope α typically takes a value of ~ 4. This is a very useful relationship in order to calculate the luminosity of a galaxy by its rotation velocity only, which does not depend on the distance at which the galaxy is located. Therefore the Tully-Fisher relation can be employed to determine the distance to a galaxy, without considering the Hubble-Lemaitre's law $v = H_0 d$. In a cosmological context, the galaxy rotation velocity is determined by the mass of the dark matter halo in which such galaxies reside, making the existence of a Tully-Fisher relation a consequence of the existence of a link between visible and dark matter mass.

For LSBGs, especially with spiral morphologies, it has been shown that these galaxies exhibit a larger dispersion around this relation when compared with other galaxies. In a study performed by O'Neil et al. (2000), the authors found that most of the galaxies in their LSBGs sample have a large dispersion around the Tully-Fisher relation, and that these residuals ε are correlated with gas fractions. Assuming that the spatial distributions of HI and stars are similar, these LSBGs are found in a regime in which there are no strong episodes of star formation. The left-hand panel of Fig. 1.9 shows the absolute B magnitude as a function of the HI equivalent width w_{50}, which is associated to the rotation velocity of the galaxy. The right-hand panel of Fig. 1.9 shows the residuals of the Tully-Fisher relation as a function of the gas fraction, in which a correlation between them is observed. From these two figures, it can be inferred that there is a huge reservoir of non-processed gas, and therefore, the gravitational well does not correspond to the luminosity. This does not mean that LSBGs do not satisfy the Tully-Fisher relation, but implies that the stellar component is not the only one that contributes to the total mass that produces the gravitational well associated to a given circular velocity. If the gas component mass is added to the stellar mass, then the dispersion around the Tully-Fisher relation decreases, and this gives rise to the so-called *Baryonic Tully-Fisher Relation* (Gurovich et al. 2004; Lelli, McGaugh, & Schombert 2016a). This large dispersion found in LSBGs around the stellar Tully-Fisher relation indicates that these galaxies have large amounts of baryonic content still in the form of non-star forming gas.

On another note, Huang et al. (2012) employed HI measurements drawn from the ALFALFA $\alpha.40$ (Haynes et al. 2011) galaxy catalog, finding that for galaxies with stellar masses $M_* \lesssim 10^{10.5}\mathrm{M}_\odot$, galaxies with higher gas fractions reside preferentially in dark matter halos with high spin parameter. Fig. 1.10 shows the gas fraction f_{gas} as a function of the stellar mass, in which the colormap corresponds to the mean value of the spin parameter on each $f_{\mathrm{gas}} - M_*$ bin. The galaxy sample employed in such study

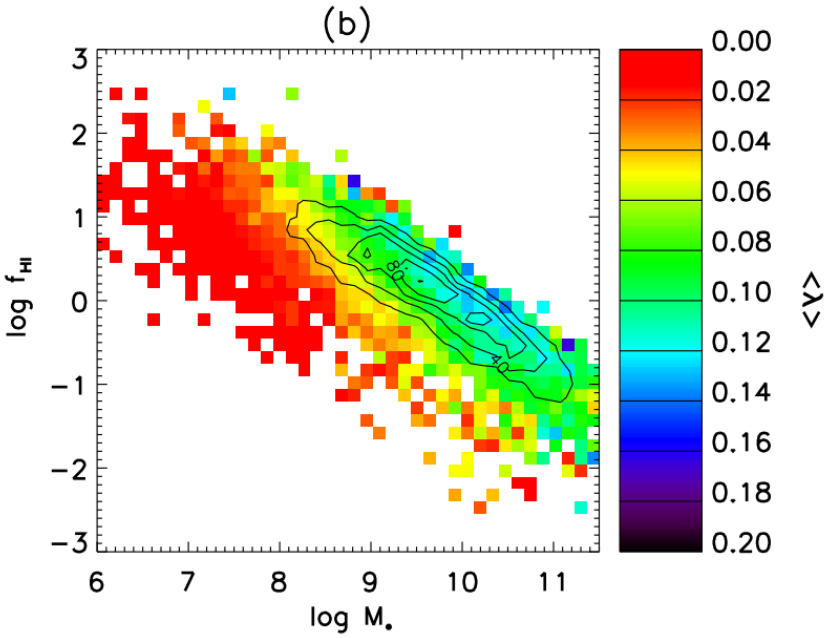

Figure 1.10: The $f_{\rm gas} - M_*$ map for galaxies in the ALFALFA $\alpha.40$ galaxy catalog. Color-coded squares indicate the mean value of λ in each map bin. Below $10^{10.5}$M$_\odot$ the gas fraction increases when increasing the spin parameter, at a given stellar mass. The galaxy sample employed includes gas-rich spirals, in which the spin parameter is obtained using the Hernandez & Cervantes-Sodi (2006) approach for spiral galaxies. [Credit: Huang et al. (2012)]

includes mostly gas-rich spirals, in which the spin parameter is calculated employing the Hernandez & Cervantes-Sodi (2006) aproximation, which considers an isothermal virialized halo, an exponential density profile for the stellar disk and perfect conservation of angular momentum between the stellar and dark matter components, besides a Tully-Fisher relation. In this plot, we observe a strong correlation between the gas content and the value of λ, such that at fixed stellar mass, the gas fraction increases with increasing λ. More recently, Lutz et al. (2018) employed a sample of gas-rich galaxies drawn from the H$_{\rm I}$ 'eXtreme' (H$_{\rm IX}$) galaxy survey (Lutz et al. 2017), and demonstrated the existence of a link between angular momentum and HI gas content, finding that HI gas-rich galaxies tend to live in halos with high angular momentum, as is the case of the high-spin galaxy population in the Huang et al. (2012) sample and the early work by Cervantes-Sodi & Hernández (2009).

1.3.3 Dark Matter Halos

Under the assumption of an underlying dark matter halo, responsible of establishing the dynamics of the baryonic components, it is well known that the dynamics of galaxies is dominated by the dark matter halo. When studying the rotation curve of LSBGs, it has been observed that these galaxies are dominated by dark matter at all radii. Pickering et al. (1997) presented a set of observations of high HI mass in four LSBGs performed by employing the VLA telescope, in which the authors found that the rotation curves of these galaxies exhibit a slow rising, and the maximum velocity is considerably high (more than 200 km/s), which indicates a high dynamical mass. Fig. 1.11 shows the resultant rotation curves of these four gas rich LSBGs, in which the contribution of the HI component, the bulge, the disk and the halo are represented by the dashed, dotted, dash-dotted and triple-dot-dashed lines, respectively. The solid line corresponds to the sum of the three components. We can observe that the component associated to the halo is always the dominant one in all cases, even in the inner regions. These galaxies represented the first evidence of massive galaxies that are dominated by dark matter at all radii. In Pérez-Montaño

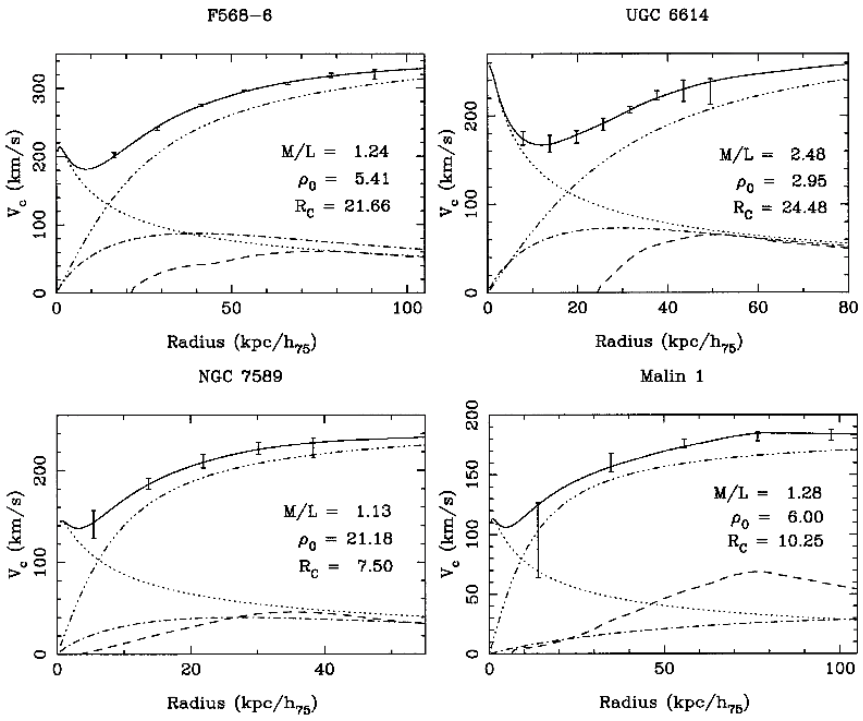

Figure 1.11: Rotation curves of four giant LSBGs studied by Pickering et al. (1997), in which the contributions of the different components of the galaxy are observed: The bulge (dotted line), the disk (dash-dotted line) and the halo (triple-dot-dashed line). [Credit: Pickering et al. (1997)]

& Cervantes Sodi (2019) we employed five different estimations of the dark matter halo mass for the galaxies in our volume-limited sample, finding that the stellar-to-halo mass fraction in LSBGs is lower than for HSBGs, with a difference reaching up to $\sim$ 22%, in agreement with previous observational findings. Fig. 1.12 shows five different 'box' plots enclosing 50% of the data. Error bars correspond to 1.5 the inter-quartile range (IQR) of the distribution. Inside each box, solid and dashed lines correspond to the mean and median values of each distribution. Independently of the method employed to calculate the stellar-to-halo mass fraction, the results are qualitatively consistent.

In recent years (e.g., Kuzio de Naray & Spekkens 2011) the observation of LSBGs dominated by dark matter has been an indication that these galaxies reside preferentially in halos whose density profile $\rho(r)$ is flattened towards the center (so-called *core halo*), which seems to contradict the ΛCDM model in which the haloes exhibit a pronounced steepness (so-called *cusp halo*) [2]. To solve this, it has been proposed that the high baryonic content in early epochs combined with the stellar feedback can modify the shape of these halos. Moreover, baryons are capable of transporting angular momentum and re-distributing the dark matter, and galaxies with massive disks can modify the shape of the gravitational well produced by the halo, favouring the formation of a *core* profile, rather than a *cusp* (Kazantzidis, Abadi, & Navarro 2010). However, the stellar disks in LSBGs do not seem massive enough to modify the density profile. To solve this apparent inconsistency Pontzen & Governato (2012) proposed the following model: it is possible that LSBGs have had more baryonic content in the early stages of their evolution, that is suppressed by the stellar feedback due to a high star formation efficiency, preventing the formation of bulges (which are commonly missing in LSBGs) and converting an initially *cusp* halo into a *core*. Therefore, according to these authors the existence of LSBGs within a ΛCDM cosmology is possible due to the strong impact of the baryonic component and the feedback during the different stages of their formation. In that case, it is expected to find differences in the star formation histories

[2] This is better known as *The Cusp-Core Problem*

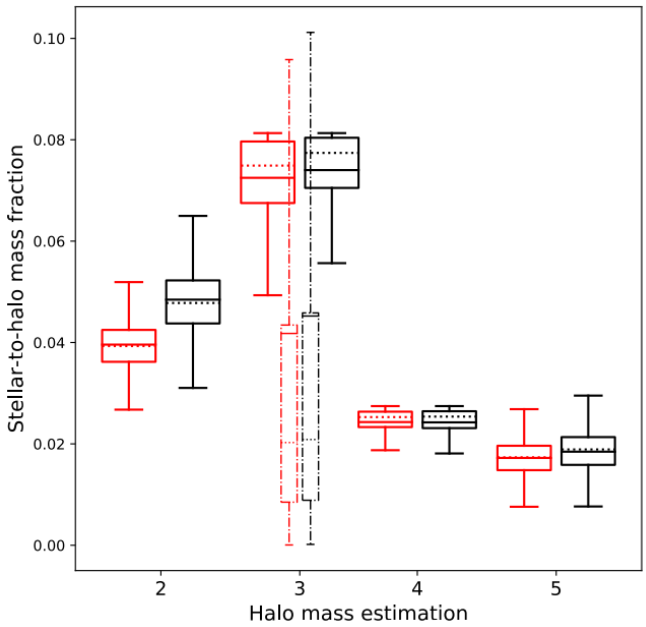

Figure 1.12: Mean (solid lines) and median (dotted lines) for the stellar-to- halo mass ratio distributions of LSBGs and HSBGs of a volume-limited sample, corresponding to five dark matter halo mass estimators. Error bars indicate 1.5 times the inter-quartile range of the corresponding distribution. [Credit: Pérez-Montaño & Cervantes Sodi (2019)]

at the center of LSBGs and HSBGs, the former showing strong 'starbursts' capable of transforming a *cusp* profile into a *core*. However, Boissier et al. (2003) found that the star formation histories of LSBGs do not exhibit such starburst at early epochs, instead showing a relatively constant star formation rate across the cosmic time[3]. Therefore, strong episodes of star formation at early epochs may not be the mechanism responsible for the *corification* of DM halos in LSBGs.

1.3.4 Environment

The environment around LSBGs has been studied in the past, but most of these studies are mainly focused on either small or large scale environments, especially due to the technical limitations that naturally arise in observational studies. However, the relative isolation in which LSBGs are found is a common result in most of these studies. For example, Bothun et al. (1993) found that the average distance between LSBGs and their closest neighbour was about 1.7 times larger than the same statistic for their HSBGs counterparts. Rosenbaum et al. (2009) employed a sample of galaxies at $z \leq 0.1$ drawn from the SDSS DR4 to compare the number density of neighbour galaxies around LSBGs, finding that these objects are found in more isolated environments than HSBGs within scales going from 2-5 Mpc, comparable with the characteristic size of galaxy groups. Fig. 1.13 shows the mean number of galaxies within a sphere of radius r for galaxies between $0.01 \leq z \leq 0.055$ (left-hand panel) and $0.055 \leq z \leq 0.1$ (right-hand panel), in which we observe that, regardless of the redshift range studied, the number of neighbour galaxies is systematically lower for LSBGs than for HSBGs. Similarly, Galaz et al. (2011) found that LSBGs tend to lack neighboring galaxies, and the percentage of galaxies without neighbours at $r < 0.5$ Mpc in their sample is about 76% and 70% for LSBGs and HSBGs, respectively. According to the authors, this particularly has a huge impact on galaxy evolution. Even when there is no distinction in the specific star formation rates between LSBGs and HSBGs, Galaz et al. (2011) found that interacting HSBGs form 'twice the number of' the stars than interacting LSBGs, showing the difficulty in low-density stellar disks

[3]This latter result will be discussed in detail in Chapter 4

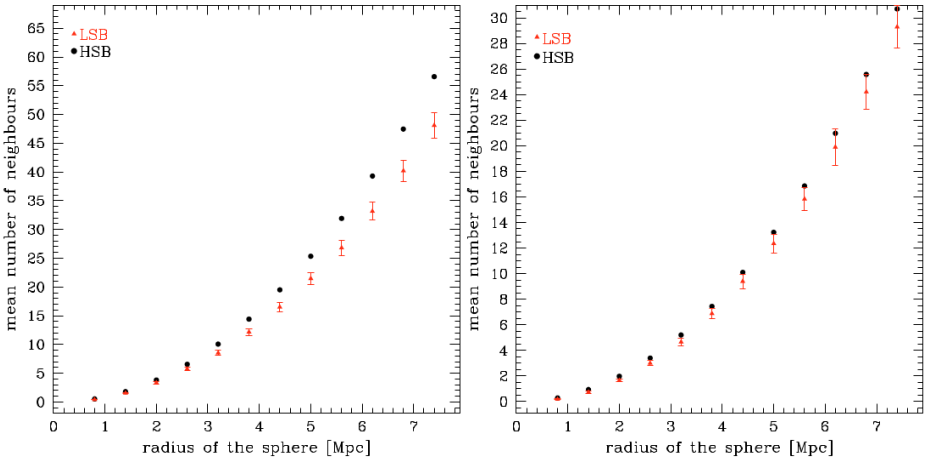

Figure 1.13: *Left:* Mean value of the number of neighbour galaxies for LSBGs (red) and HSBGs (black) for galaxies with $0.01 \leq z \leq 0.055$. *Right:* Same figure, but for galaxies with $0.055 \leq z \leq 0.1$. In both cases, it is observed that LSBGs tend to be found in more isolated environments than HSBGs. [Credit: Rosenbaum et al. (2009)]

within massive dark matter halos (as in the case of LSBGs) to amplify and propagate perturbations due to close companions. In Pérez-Montaño & Cervantes Sodi (2019) it is found that the fraction of isolated central LSBGs is higher than the fraction of isolated HSBGs, showing that the former are most likely to inhabit more isolated environments.

In a set of high-resolution N-body simulations performed by Wang et al. (2011), a mild but significant correlation between the spin parameter and the environment in which galaxies reside is found. This trend is not surprising given that, as mentioned in 1.3.1, the angular momentum is generated by tidal forces. The left-hand panel of Fig. 1.14 shows that λ increases when the tidal field t_1, defined as the magnitude of the tidal force along the direction of $\vec{t_1}$, is more intense. Analogously, the right-hand panel of Fig. 1.14 shows that the spin parameter is also increased when the local overdensity $\delta = (\rho - \bar{\rho})/\bar{\rho}$ is higher. Therefore a denser environment implies a stronger gravitational interaction, reflected in a high angular momentum of the halo, suggesting that the spin parameter is originated from tidal torque, rather than from random mergers. However, the authors found that the correlation between halo spins and tidal field is weaker than predicted, suggesting that this relation is not well understood. In a recent study performed by Martin et al. (2019) employing a sample of simulated galaxies drawn from Hoizon AGN (Dubois, et al. 2014) the authors study the spatial distribution of LSBGs finding that these galaxies are found in high density environments than HSBGs, but LSBGs having lower spin parameters than HSBGs, which contradicts the results of Wang et al. (2011). We point out that in Martin et al. (2019) the authors do not do a strict control over the masses, as other studies (including this one) do. Therefore, we attempt to quantitatively characterize different environments in order to provide an answer to this contradiction. The findings in Martin et al. (2019) are also in contrast Interestingly, these findings seem to be in contrast with the findings of Pérez-Montaño & Cervantes Sodi (2019), who find marginal but statistically significant differences between LSBGs and HSBGs, showing that LSBGs are found in lower density environments. This apparent contradiction could be explained as follows: even when denser environments increase the angular momentum of the halo in which these galaxies reside, these interactions can also lead to the 'ripping' of less massive, gas-rich galaxies falling onto a massive one, as mentioned in Kulier et al. (2020). Another possibility is that galaxies in lower density environments experience less drag and hence dissipate less angular momentum, allowing them to remain with higher angular momentum after several Gyr. Therefore, LSBGs may not be just galaxies formed in isolated environments, but they might also be missing in high density environments due to their fragile structure and their proclivity to be destroyed by close encounters with massive neighbours.

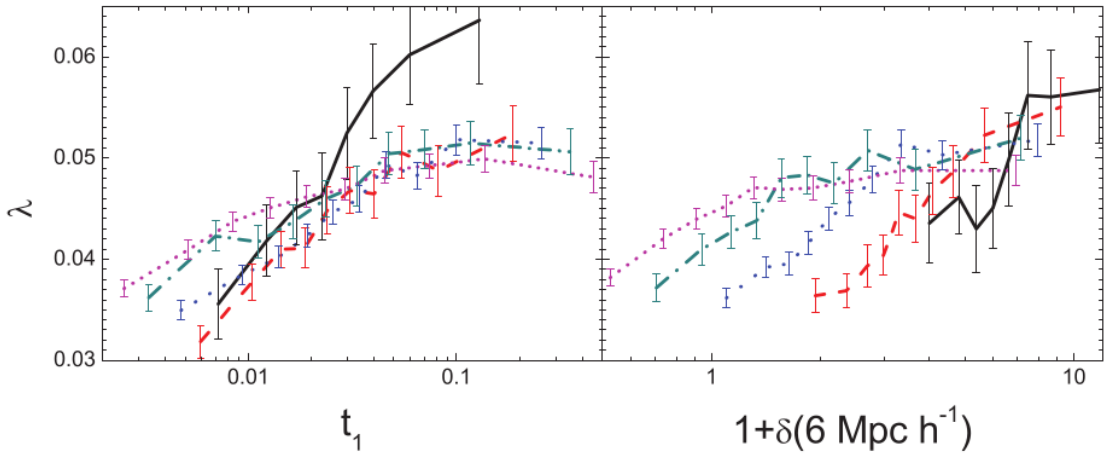

Figure 1.14: Spin parameter λ as a function of the tidal force field t_1(left) and local overdensity δ (right). In both cases, each colored line represents different dark matter halo mass intervals, going from $10^{12} - 10^{14.5} M_\odot$ for five different bins of 0.5 dex width, represented in magenta, turquoise, blue, red and black, respectively. [Credit: Wang et al. (2011)].

Very few works have made emphasis on the study of the large-scale environment of LSBGs, especially from the observational point of view. Rosenbaum et al. (2009) suggested that LSBGs are formed originally in low-density structures and later are displaced to the outer part of filaments and walls of the large-scale structure. Fig. 1.15 shows a slice of a 3D map of SDSS DR4 objects, in which the large-scale structure of the Universe can be appreciated. Green points correspond lo HSBGs while the black ones represent LSBGs. In this diagram we observe that the latter seem to be found preferentially in the outer regions of high density environments such as the external parts of filaments and clusters. Pérez-Montaño & Cervantes Sodi (2019) found that a significant fraction of LSBGs ($\sim$ 60%) is preferentially found in filaments, rather than other large-scale structures, and that early-type LSBGs are further away from the their nearest filament than HSBGs. This difference might arise if LSBGs are formed in low-density regions (e.g. voids), and then these systems migrate to the outer regions of the filaments, where they are observed now. In Ceccarelli et al. (2012), the authors found that there is a strong systematic drop in the LSBG fraction when moving away from the center of voids, whereas the fraction of HSBGs increases. Moreover, the transformation of quiescent LSBGs into star-forming HSBGs is possibly due to the gas arriving from the void interior as consequence of void expansion.

It is important to highlight that the results of the previously mentioned works show contrasting results and most of them are not compatible with each other. Therefore, it is important to explore the influence of the environment using different ways of quantifying it at different scales. This can provide a better perspective on the origin of these inconsistencies, and will allow a much more complete and detailed study of the impact of the environment on the formation of LSBGs, as well as a better understanding of the main phenomena that play a fundamental role in determining the evolutionary path that these galaxies follow, until they become LSBGs.

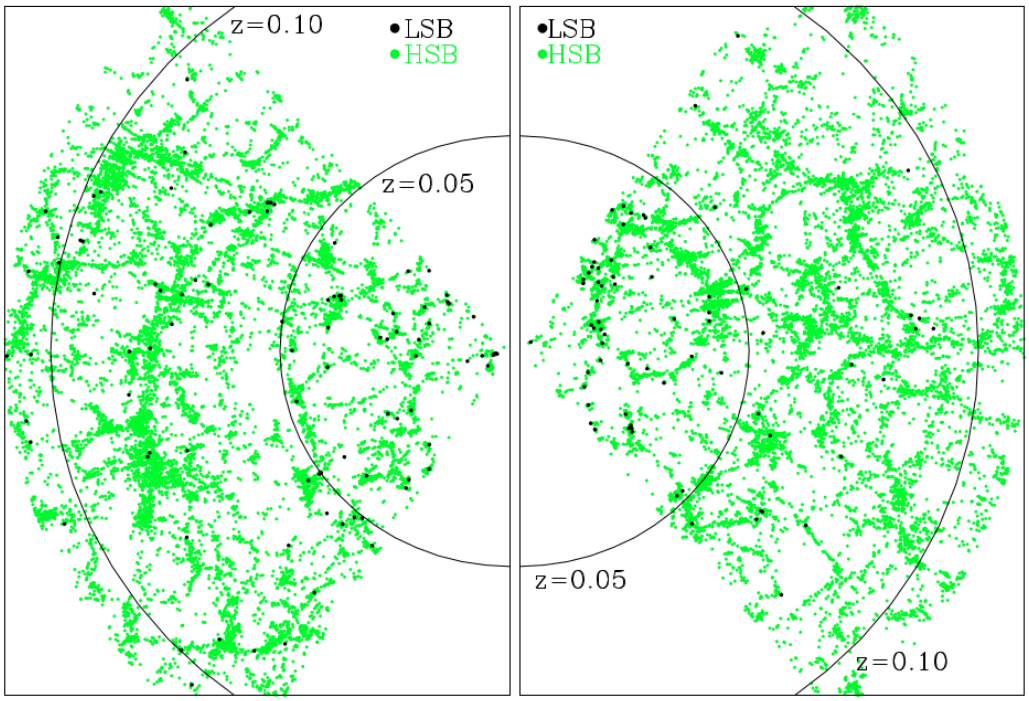

Figure 1.15: Spatial distribution of SDSS DR4 galaxies. Black points correspond to LSBGs, which are located in the outer parts of the filamentary structure [Credit: Rosenbaum et al. (2009)]

1.4 Formation and Evolution of LSBGs in Cosmological Simulations

Given the faint nature of LSBGs, observational studies are considerably biased to objects in the local Universe (no further than $z = 0.1$), so any observational clue on the formation of these kind of objects at high redshift, if any, could be hardly observed even with the most sophisticated instruments[4]. Additionally, the "Tolman's test" (Tolman 1930, 1934) highlights that, due to the expansion of the Universe, the surface brightness of an extended source decreases with z as

$$\mu(z) = \mu(z = 0) + 10\log(1 + z), \tag{1.9}$$

implying that, for example, a galaxy with $z = 1$ has a dimming of surface brightness of 3. Therefore, a galaxy with μ =23 mag arcsec^{-2} would be barely undetectable. In order to understand how LSBGs arise within a cosmological context, including the effects of mergers, environment, and more realistic and diverse formation histories, the use of cosmological hydrodynamical simulations has gained interest in recent years (see Somerville & Davé 2015; Vogelsberger et al. 2020).

Martin et al. (2019) employed HorizonAGN (Dubois, et al. 2014) to study how LSBGs, HSBGs, and UDGs[5] evolve with time. They found that LSBGs and HSBGs are formed from the same population of objects, but LSBGs evolve faster, especially at $z \sim 1$, where LSBGs have lost large amounts of star-forming gas[6] due to ram-pressure stripping and tidal forces, affecting their evolution especially at lower redshifts. These authors argue that LSBGs progenitors form stars more rapidly at early epochs, and after $z \sim 1$, tidal perturbations broaden their stellar distributions spatially, heating the gas and creating the

[4]LSBGs could be identified at high z with modern instruments like JWST, but it is not its main goal. However, JWST observations could be complemented with new upcoming galaxy surveys such as the Legacy Survey of Space and Time (LSST), which will be useful for that purpose.

[5] *Ultra Diffuse Galaxies*

[6]Defined as those gas cells dense enough to form stars, i.e., with $n_{\text{gas cell}} > 0.1$ cm^{-3}.

diffuse extended LSBGs seen today. They also found that 'classic' LSBGs[7] and HSBGs have very similar star formation histories, with the real distinctions emerging between HSBGs and UDGs. The evolution in the effective radius is steady with time, indicating that it is unlikely that the large radii of LSBGs seen nowadays are the result of single violent events at early epochs. The formation mechanisms that produce LSBGs act to both increase the effective radii of their progenitors and drive the steady loss of star-forming gas, producing systems with low SFR and older stellar populations and as a consequence, galaxies with low surface brightness. Fig. 1.16 shows the redshift evolution of LSBGs and HSBGs in the star-forming gas fraction vs effective radius plane found by Martin et al. (2019), in which we observe that the main progenitors of the different galaxy populations are very similar at high redshift ($z \sim 3$), sharing essentially identical effective radii and star-forming gas fractions (should not be confused with, for example, warm gas.) in the early Universe, indicating that LSBGs emerge from a common population of progenitors as HSBGs. Both LSBGs and HSBGs undergo very few actual mergers at low redshift, when the effective radii and star-forming gas fractions change significantly. Galaxy mergers, therefore, are unlikely to be the principal driver of LSBGs evolution over cosmic time. In fact, tidal interactions are likely to be the primary mechanism that drives LSBGs evolution and causes these systems to both expand and lose their reservoir of star-forming gas over cosmic time. Tidal interactions exerted on the gas can remove it from the galaxy and quench star formation, especially for low-mass galaxies.

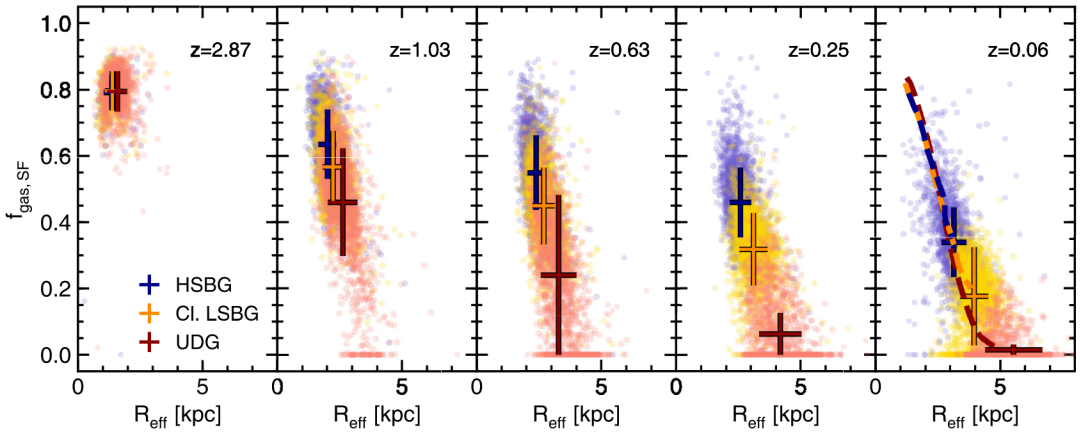

Figure 1.16: Redshift evolution of the star-forming gas fraction and effective radii of the progenitors of HSBGs (blue), 'classic' LSBGs (orange), and UDGs (red). The error bars in each panel show the median values and 1σ dispersions for the distributions of the different galaxy populations at each redshift. The dashed lines in the right-hand panel indicate the average locii followed by the main progenitors of HSBGs, LSBGs,and UDGs in the f_{gas}–R_{eff} plane over cosmic time [Credit: Martin et al. (2019)]

In another study performed by Di Cintio et al. (2019), the authors investigated the origin of LSBGs with stellar masses in the range $10^{9.5-10} M_{\odot}$, employing 12 galaxies drawn from the NIHAO zoom-in cosmological simulation (Wang et al. 2015). They found that their simulated LSBGs share some particular properties with observed ones, having large HI reservoirs, extended star formation histories and large effective radii ($R_e \gtrsim 4$ kpc). Galaxies with low surface brightness show more extended stellar disks, small or no central bulges, and ongoing star formation in the outskirts of the disks. Moreover, they showed that LSBGs are formed inside DM halos with $\lambda > 0.04$, and their density profiles are shallower, as a result of the ejection of baryons by stellar feedback. The authors found that mergers seem to play a fundamental role shaping the final surface brightness of galaxies. Certain merger configurations are able to add angular momentum to the galaxy, and as a result, the surface brightness is decreased, for example, galaxies that had coplanar mergers have their total angular momentum increased and as a consequence, the effective radius is increased. On the other hand, perpendicular mergers remove angular momentum efficiently from the previously existent disk, creating galaxy populations whose properties are similar

[7]Defined by the authors as galaxies with $23 < \mu_r < 24$ mag arcsec^{-2}.

to HSBGs. The direction in which the gas falls into these galaxies during their formation is also a key parameter in the determination of the properties of LSBGs. Fig. 1.17 shows the evolution of two examples, creating an LSBG (top) and an HSBG (bottom). A coplanar merger is identified at $z \sim 4$, resulting in an increase of the effective radius and decreasing density, similar to the case of LSBGs (top-right panel). Similarly, a perpendicular merger is identified for the case of HSBGs, resulting in more compact objects with high surface densities (bottom-right panel). With mergers and accretion driving new episodes of star formation, important differences would be found in the distribution of newly-formed stars. Their young stellar population form throughout the disk, from the inner regions to the outskirts as a result of the flat HI gas surface density profile, implying higher gas densities at large radii for the case of LSBGs.

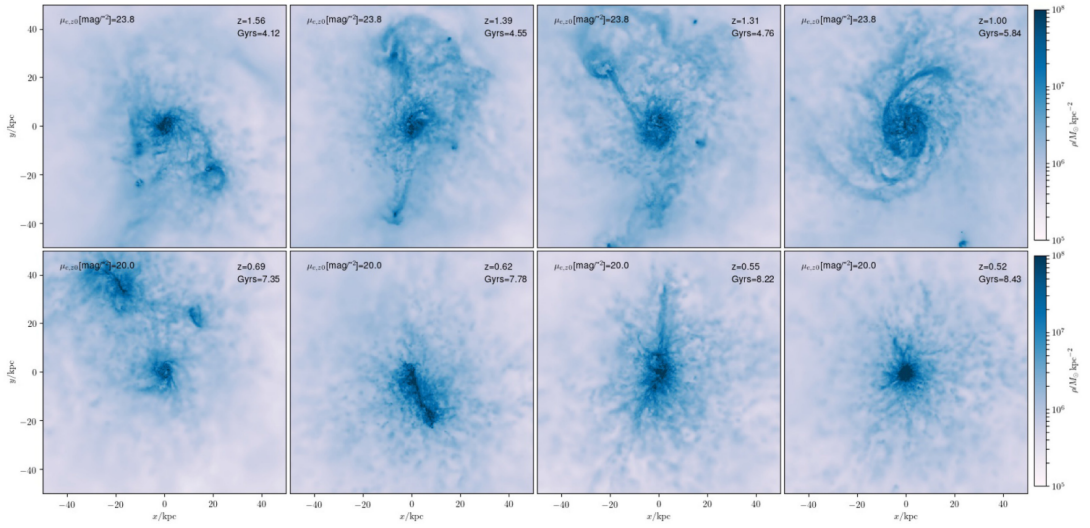

Figure 1.17: Snapshots of gas density during and after the largest merger of two representative galaxies. In the LSBG case, a coplanar merger can be identified at $t \sim 4$Gyr, which adds angular momentum to the disk and whose final product is a large-sized, low μ object (top-right panel). For the HSBG, a perpendicular merger can be observed at t $\sim$ 7.5 Gyr. This orbital configuration removes angular momentum from the existing disk and results in a compact, high μ galaxy just after the merger (bottom-right panel) [Credit: Di Cintio et al. (2019)]

In Kulier et al. (2020), the properties of LSBGs with $M_* > 10^{9.5}$ were studied employing the EAGLE cosmological simulation (Schaye, et al. 2015; Crain, et al. 2015; McAlpine, et al. 2016). These authors found that LSBGs are more isolated systems than HSBGs, and their proposed formation scenario points to galaxies with high angular momentum corresponding to the most extended LSBGs that are built-up via mergers, in which galaxies with $\sim 10^{11} M_\odot$ exhibit extended stellar halos around them. Galaxies that have experienced more mergers tend to exhibit larger faint components in their outer parts, and the importance of this effect depends on how much stellar mass the mergers contribute. The authors also pointed out that LSBGs and HSBGs of similar stellar mass are formed in DM halos of similar mass, but the former inhabit more concentrated halos, with higher spin parameter, and being more gas-rich than HSBGs. Fig. 1.18 presents a summary of these findings, where LSBGs (blue) and HSBGs (red) are segregated according to a B-band selection criterion. The authors conclude that LSBGs with little contribution of mergers represent the dominant type of galaxies with masses between $10^{9.5-10.5}$M$_\odot$, and they are formed as a combination of both in-situ star formation and 'tiny' mergers.

While mergers typically transform galaxies into spheroids, some of them instead build up a rotationally supported extended disk, this being the main mechanism to form 'giant' LSBGs. Fig. 1.19 shows the evolution of the 'circularity' $\epsilon_*(R)$, for different stellar mass fractions accreted via mergers. The circularity is defined as the ratio between the component of the angular momentum which is perpendicular to the

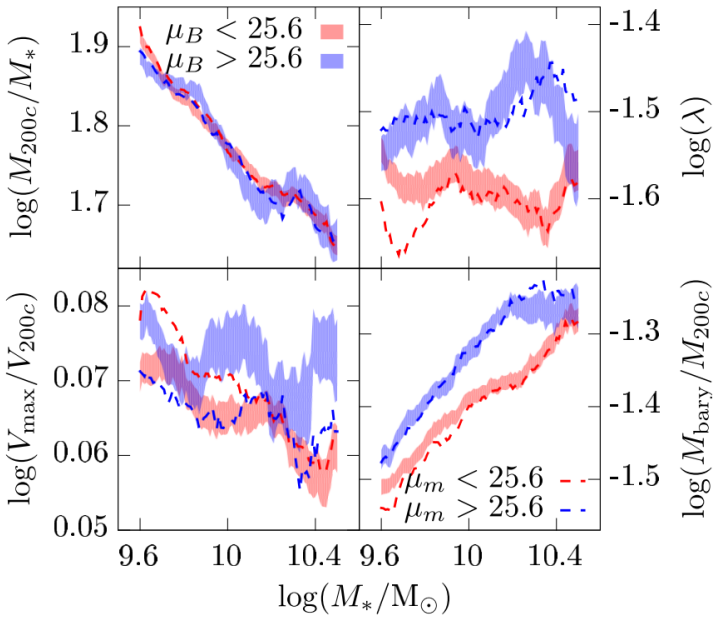

Figure 1.18: Mean value of the dark matter halo properties studied in Kulier et al. (2020), namely the halo-to-stellar mass fraction (top left), the halo spin parameter (top right), the halo concentration index (bottom left) and the baryonic-to-halo mass fraction (bottom right), as a function galaxy stellar mass. Blue and red bands represent the error around the mean for LSBGs and HSBGs, respectively. [Credit: Kulier et al. (2020)]

disk and the angular momentum of a circular orbit whose kinetic energy is equal to the binding energy at radius R[8]. Each row represents three different bins of $\Delta M_{ex}/M_*$, and mergers between $z = 0.5$ (solid line) and $z = 0$ (dashed line) are plotted. Each color corresponds to different ranges of the median orbital circularity at the 28 mag arcsec^{-2} isophote. It is observed that low-mass galaxies (left-hand panels) have not changed their kinematic profiles significantly, keeping their circularity nearly equal since $z = 0.5$. However, for galaxies with high M_* (right-hand panels), the buildup of rotationally-supported disks in the outer regions of galaxies can be observed (stars with $\epsilon_* > 0.5$). This effect is even more notorious when high mass galaxies with high fractions of accreted stellar mass are considered, as observed in the bottom-right panel of Fig. 1.19.

In a recent study employing IllustrisTNG (Nelson, et al. 2018; Pillepich et al. 2018; Springel et al. 2018), Zhu, et al. (2018) reported an analog of the giant LSBG 'Malin 1' (Bothun, et al. 1987), which reproduces very accurately many features of this specific object, such as stellar ages, metallicity and rotation curves. Employing the TNG100 run, the authors found that this galaxy has a stellar radius of ∼100 kpc, and that this galaxy is mainly formed by an encounter of two galaxies, in which a massive one is disturbed by a less massive gas-rich galaxy. The extended stellar disk is a result of hot gas cooling, triggered by a huge amount of gas coming from an in-falling galaxy over it. Fig. 1.20 shows how the extended disk is formed after $z = 0.3$, when the merger event occurred. This formation mechanism could explain the observed properties of Malin 1, such as its extended disk, which normally is not well explained by the current ΛCDM galaxy formation theory[9]. In an upcoming work (Zhu, Pérez-Montaño, et al. in prep.), we explore deeper the origin of these 'giant' LSBGs in a larger sample of simulated galaxies, finding that giant LSBGs are found with different morphologies, from the most disk-dominated systems to massive ellipticals, but all of them found in massive halos with large halo spin parameter.

[8] Described in detail in chapter 2

[9] We must remind ourselves that the ΛCDM paradigm for galaxy formation and evolution is incomplete, and therefore, is reasonable to find inconsistencies and contradictions with observations given that the model itself is an approximation of reality.

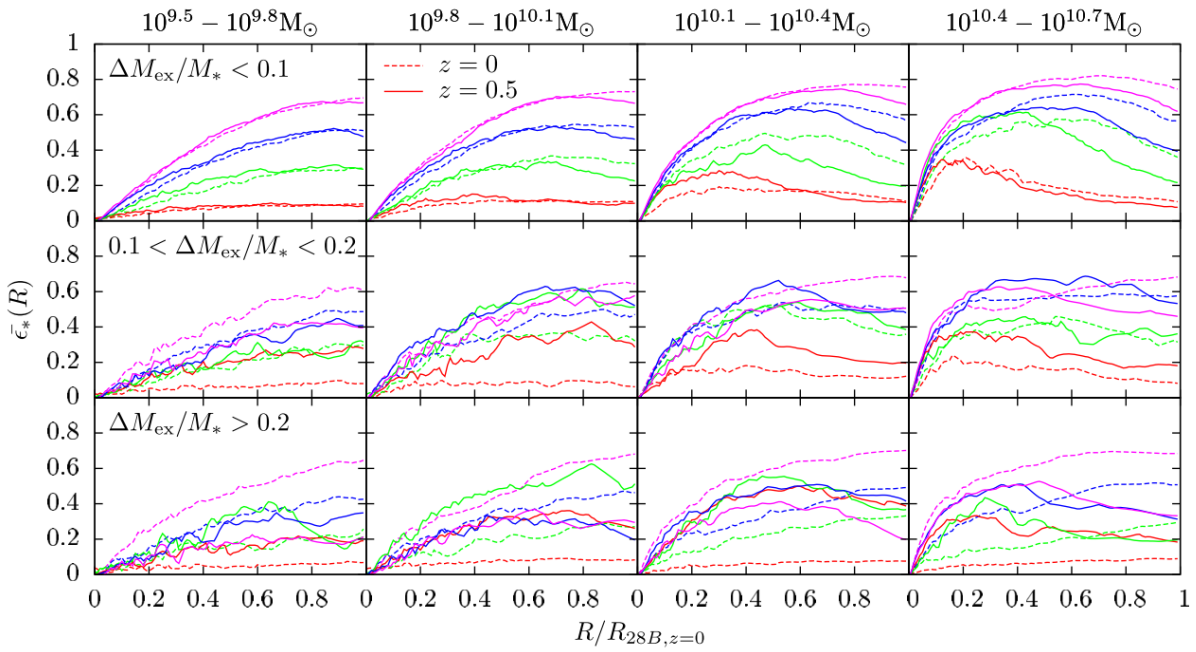

Figure 1.19: The evolution of $\epsilon_*(R)$ for galaxies with different accreted stellar mass fractions. Galaxies in each panel are binned in four different ranges of the median orbital circularity at the 28 mag arcsec^{-2} isophote, namely 0−0.2 (red), 0.2−0.4 (green), 0.4−0.6 (blue) and 0.6−0.8 (magenta). For galaxies with a significant merger contribution, a stronger change in kinematic morphology is observed, with some galaxies becoming more rotation-dominated in the outer regions. [Credit: Kulier et al. (2020)]

In this study, is found that aligned mergers promote the formation of extended disks, and the isolated environment allows these galaxies to survive across cosmic time. Moreover, the distribution of r_{5th}, defined as the distance to the 5th nearest neighbour, shows that these giant LSBGs are mostly located in isolated environments.

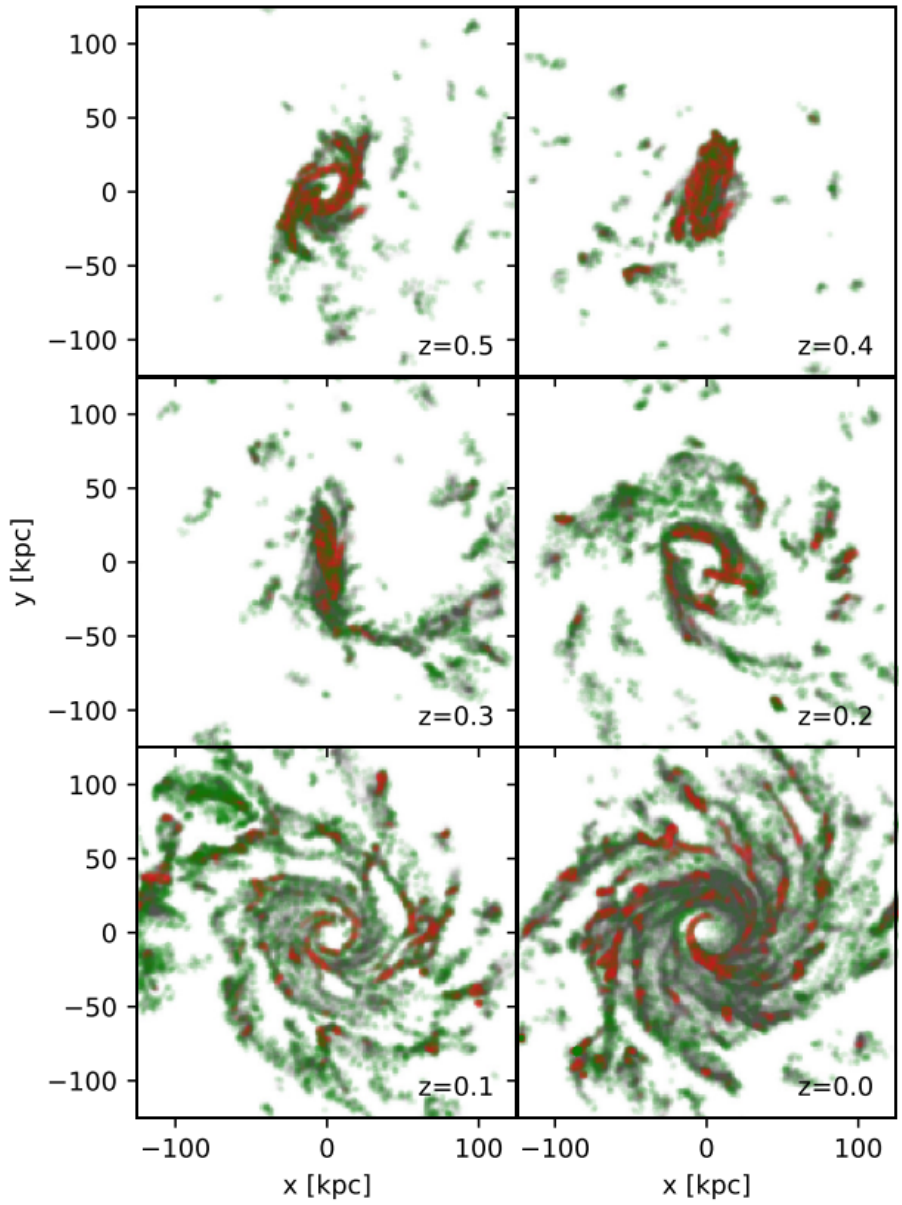

Figure 1.20: The formation of an extended stellar disk in a Malin 1 analogue found in TNG100. Grey, green and red cells correspond to cold, warm and star-forming gas, respectively. [Credit: Zhu, et al. (2018)]

Chapter 2

Sample Description

In this chapter, we fully describe the main characteristics of the TNG simulations and how they compare with the original model of Illustris. We also describe the selection criteria for the sample and the methodology employed to compute the central surface brightness of the galaxies in our sample, which allow us to segregate them into samples of LSBGs and HSBGs to study their main properties and their evolution.

2.1 The Illustris/Illustris TNG project

The Illustris project (Genel, et al. 2014; Vogelsberger et al. 2014; Nelson, et al. 2015) is a set of state-of-the-art cosmological, hydrodynamical simulations, which incorporates the dynamics of dark matter particles together with hydrodynamical processes related with baryons coupled to the different dark matter structures, adopting a fiducial physical model that includes star formation and evolution, primordial metal-line cooling, gas recycling, chemical enrichment, stellar supernovae feedback and SMBH with their associated feedback. Cosmological simulations of galaxy formation are performed within a cosmological model and start from specific initial conditions. The leading model for structure formation assumes dark matter is cold, with negligible random motions when decoupled from other matter, collisionless dark matter, and dark energy represented by a cosmological constant. Initial conditions specify the perturbations imposed on top of a homogeneous expanding background. Inflation predicts Gaussian perturbations which are specified by the power spectrum $P(|K|)$, and once the linear density fluctuation field has been specified, dark matter positions and velocities are assigned along with baryon density, velocity and temperature fields. A full overview of the metodology of cosmological simulations is available in Vogelsberger et al. (2020). An overview poster of the Illustris project can be visualized in Fig. 2.1.

The largest and most complete calculation in terms of implemented physics, Illustris-I (or simply 'The Illustris simulation') follows the dynamics of gas coupled with dark matter with a quasi-Lagrangian treatment employing the moving-mesh code `AREPO` (Springel 2010; Pakmor et al. 2016), within a cubic cosmological volume of 106.6 Mpc per side. The simulation follows 1820^3 DM particles and approximately 1820^3 resolution elements, in which the mass of a DM particle is $m_{\rm DM} = 6.26 \times 10^6 {\rm M}_\odot$ and the typical mass of a baryonic resolution element is $m_{\rm baryon} = 1.26 \times 10^6 {\rm M}_\odot$. `AREPO` allows an adaptative dynamical discretization of the hydrodynamical equations, such that every point of the grid in which equations are solved, are coupled with the gas and therefore, moving together with it. The galaxy formation model included in Illustris is based on a standard ΛCDM cosmology drawn from WMAP-9 (Hinshaw, et al. 2013) with $\Omega_m = 0.2726$,$\Omega_b = 0.0456$,$\Omega_\Lambda = 0.7274$ and $H_0 = 70.4$ km/s Mpc^{-1}. The simulation runs over 136 *snapshots* covering a redshift range of $z = 127 - 0$, and includes the following astrophysical processes:

- Gas cooling and photoionization: The gas cooling is calculated as a function of the density, temperature, metallicity, UV radiation and active galactic nuclei (AGN). The UV background is

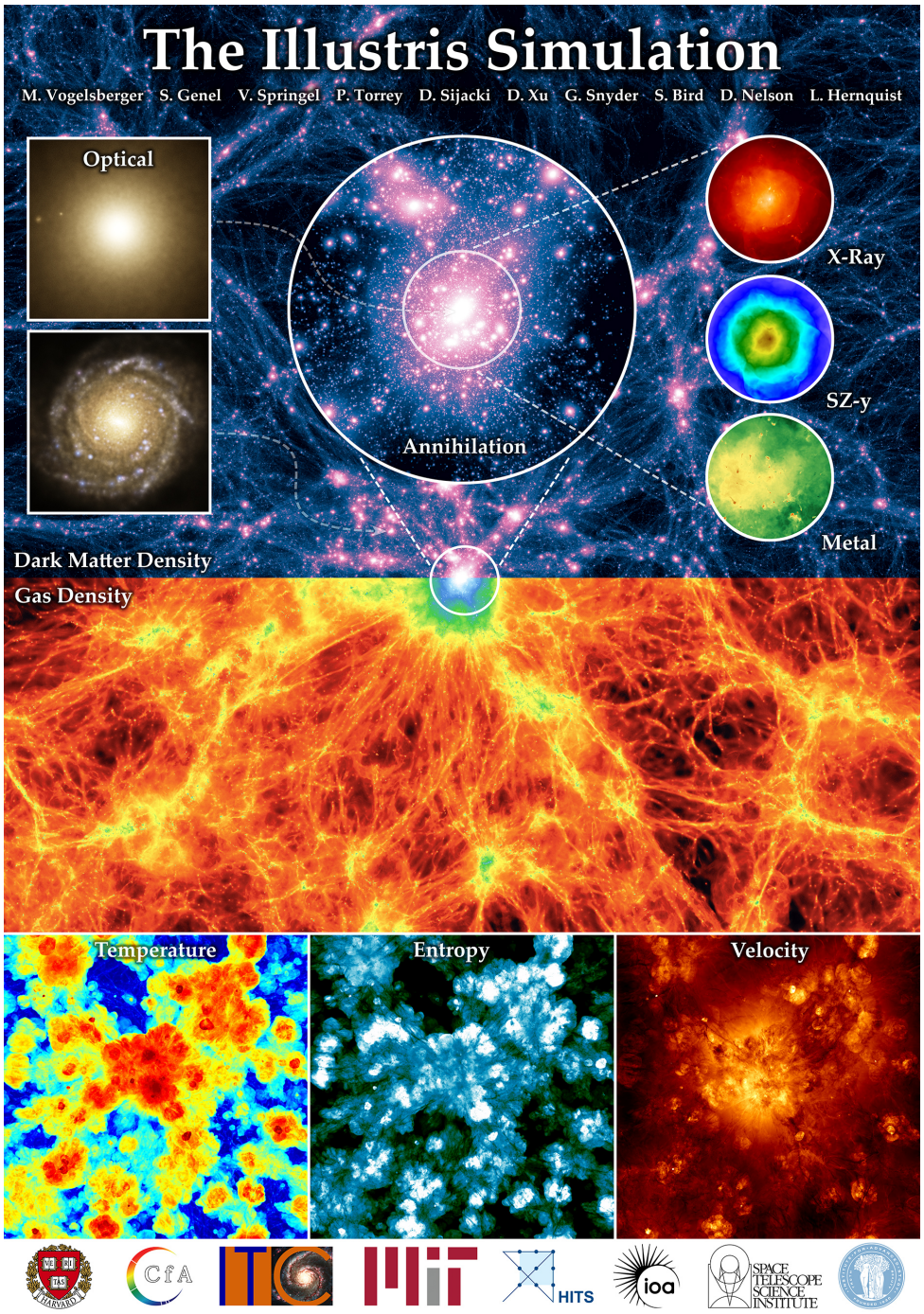

Figure 2.1: Illustris simulation overview poster. The figure shows 2D projections of the large-scale dark matter (top) and gas density (middle), while the lower three panels show gas temperature, entropy, and velocity at the same redshift. Centered on the most massive cluster, the circular insets show four predicted observables. The two galaxy insets highlight a central elliptical and a spiral disk satellite. [Credit: Vogelsberger et al. (2014)]

spatially uniform and is a function of time (Katz, Weinberg, & Hernquist 1996; Wiersma, Schaye, & Smith 2009).

- Star formation and Interstellar medium: Star formation is given stochastically following a Kennicutt-Schmidt law, with a Chabrier initial mass funcition (Chabrier 2003).
- Stellar evolution: The different stellar populations return mass to the interstellar medium through stellar winds and supernovae, associated with SN Ia, SN II and AGB stars (Wiersma et al. 2009; Few et al. 2012).
- Stellar feedback: A kinematic treatment is employed to generate winds with velocities that scale with the local velocity dispersion of the dark matter, whereas the chemical enrichment is such that only 40% of metals in the interstellar medium are expelled trough these winds (Navarro & White 1993; Springel & Hernquist 2003)
- Black Holes: The feedback from super massive black holes (SMBH) considers the radiation field from AGNs, that heats the surrounding gas modifying its ionization status and its cooling rate (Di Matteo, Springel, & Hernquist 2005; Springel et al. 2005c; Booth & Schaye 2009; Dubois et al. 2012).

2.1.1 Improvements of TNG with respect to the 'original' Illustris

The IllustrisTNG simulation (herafter, TNG, Nelson, et al. 2018; Pillepich et al. 2018; Springel et al. 2018) is a set of 18 magneto-hydrodynamical simulations that constitute the upgraded version of the original Illustris formation model, which vary in size, resolution and complexity of the physical processes involved, namely:

- Formation, growth, and SMBH feedback: In the low-accretion state, a kinematic model of AGN feedback that produces winds impulsed by black holes is employed (Weinberger, et al. 2017), replacing the original "bubble" model from Sijacki, et al. (2007). Additionally, the initial mass of black holes is increased from 1 to $8.5 \times 10^5 h^{-1}$ $M_\odot$. The new feedback model is responsible for the quenching of galaxies that reside within halos of intermediate/high mass ($\sim 10^{12} - 10^{14}$ $M_\odot$), and the formation of a galaxy population of red and quenched galaxies at late epochs.
- Galactic Winds: In the original model, the initial direction of the particles coming from winds had a "bipolar winds" focus, in which the particles were expelled along a preferential direction. In the new model, an initial velocity is assigned to the wind particles in random directions, i.e. isotropic winds that naturally propagate in the direction of least resistance. The TNG model launches wind particles with an initial velocity that scales with the velocity dispersion of the local dark matter particles. Besides, the TNG model introduces an additional factor dependent on z for the wind velocities, and establishes a minimum velocity for these winds. Finally, the TNG model includes two modifications that affect the energy of the wind: a given fraction of this energy is thermal energy, and the energy of the wind depends on the metallicity of the gas cells, in such a way that galactic winds are weaker in environments with more metallicity. High metallicities imply higher energy losses due to cooling (Schaye, et al. , 2015; Martizzi, Faucher-Giguère, & Quataert, 2015), directly affecting the energy injected into the ISM. This new term introduced in the TNG model implies that the winds in low-mass galaxies are stronger than in the original Illustris model.
- Stellar evolution and chemical enrichment: In the TNG model it is assumed that AGB stars have $1 - 8$ $M_\odot$, while supernovae are originated from stars with $8 - 100$ $M_\odot$ (in the original model, the minimum mass was 6 $M_\odot$). Moreover, in TNG the mass range of AGB stars that produce metals is extended from $1 - 6$ $M_\odot$ in the original model to $1 - 7.5$ $M_\odot$ in TNG, for different metallicities. The different mass fractions of metals returned to the interstellar medium through SNs between the two models are due to changes in the production of metals.

The simulation employs a *Friends-of-Friends* (FoF, Davis, et al. 1985) algorithm to identify the dark matter halos with a minimum of 32 particles with a linking length $b = 0.2$, resulting in an average enclosed

density of ~ 180 times the "global" density, which is the value predicted by the spherical collapse model (see e.g. Mo, van den Bosch, & White 2010). The FoF algorithm is run on the dark matter particles, and the other particle types (gas, stars and BHs) are attached to the same groups as their nearest DM particle. The halo mass M_{200} corresponds to the mass contained within a spherical region that encloses 200 times the critical density of the Universe at that time. Each halo contains subhalos, identified with the `SUBFIND` algorithm (Springel, et al. 2001; Dolag, et al. 2009). Each subhalo has a well-defined mass based on the particles gravitationally bounded to it.

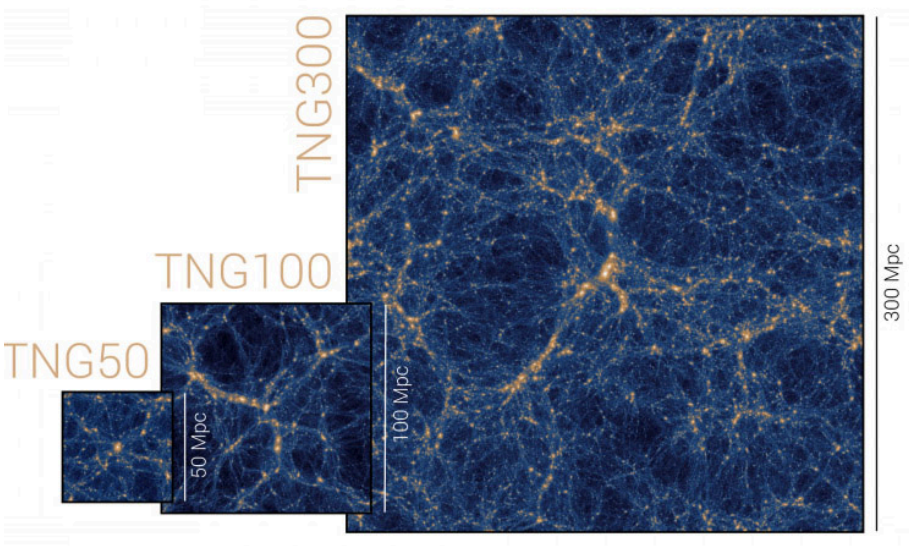

Run Name	$L_{\rm box}$ [com Mpc]	$N_{\rm GAS}$ -	$N_{\rm DM}$ -	$m_{\rm baryon}$ [$M_\odot$]	$m_{\rm DM}$ [$M_\odot$]	$\epsilon^{z=0}_{\rm DM,stars}$ [pc]	$\epsilon_{\rm gas,min}$ [phys pc]	$\bar{r}_{\rm cell,SF}$ [com pc]	CPU Time [Mh]	$N_{\rm cores}$ -
TNG50(-1)	51.7	2160^3	2160^3	8.5×10^4	4.5×10^5	288	72	140	~ 130	16 320
TNG100(-1)	110.7	1820^3	1820^3	1.4×10^6	7.5×10^6	738	190	355	18.0	10 752
TNG300(-1)	302.6	2500^3	2500^3	1.1×10^7	5.9×10^7	1477	370	715	34.9	24 000

Figure 2.2: *Top:* Comparison of the size of the different boxes employed in the TNG runs. Each box shows the projected dark matter denisty at a given snapshot. [Credit: Nelson D., et al., 2019, Computational Astrophysics and Cosmology, Volume 6, Issue 1, article id. 2, 29 pp.] *Bottom:* Physical and numerical parameters of the IllustrisTNG series, TNG100 and TNG300, including the box side-length, the initial number of gas cells and dark matter particles, the baryonic mass resolution, the DM particle mass, the gravitational softening of the collisionless component, the minimum comoving value of the adaptive gas gravitational softenings, and the average cell size of star-forming gas across the simulated volumes. [Credit: Pillepich et al. (2019)]

TNG employs boxes of different size: 50, 100 and 300 Mpc per side, namely TNG50, TNG100 and TNG300, respectively, each one with 99 *snapshots* running from $z = 20$ to $z = 0$, in a way in which it is possible to study galaxy formation at different scales, includying the formation of large galaxy clusters (TNG300) as well as the gas structures around a specific galaxy (TNG50). Fig. 2.2 shows a comparative chart of the different box sizes employed in TNG. Each box runs three different simulations at different resolution levels (2×455^3, 910^3 and 1820^3 particles), allowing a clear analysis on how the resolution impacts the output, and consequently the interpretation of the results. The TNG simulation aims to improve the deficiencies of the original Illustris model (such as the feedback model), allowing to obtain smaller galaxies, comparable with those found in large galaxy surveys, as well as expanding the scope of large volume simulations with higher resolution, and the inclusion of new physical processes involved such as magnetohydrodynamics (MHD). The TNG model is based on a cosmology drawn from The Planck Collaboration (The Planck Collaboration 2016), in which $\Omega_m = 0.31$, $\Omega_\Lambda = 0.69$, $\Omega_b = 0.0486$ and $h =$

0.677.

2.2 Sample construction

In the current work, we employed the TNG100 run at its highest resolution level (1820^3 particles), taking data output of the snapshot corresponding to $z = 0$, in order to obtain a sample of simulated galaxies that roughly corresponds to nowadays observed galaxies. Using TNG100 allows us to study well-resolved galaxies to treat them as individual objects, rather than analyze them as part of large galaxy clusters (TNG300), without considering any current substructure within them (TNG50). We employed the data of the stellar component (`parttype == 'stars'`) for each subhalo, considering galaxies with $10^9 < M_* < 10^{12}\mathrm{M}_\odot$, given that median stellar sizes in TNG100 are not well covered below 10^9 $\mathrm{M}_\odot$ (Pillepich et al. 2019), due to the few stellar particles that define a disk, and this would strongly affect the fraction of LSBGs found at the low-mass end. We then segregate our galaxy sample between LSBGs and HSBGs by computing the surface brightness as follows:

1. Taking the corresponding mass, velocity and position of each particle in a given galaxy, we calculate the specific stellar angular momentum j_* as

$$\vec{j_*} = \frac{\vec{J}}{M} = \frac{\sum_i m_i \vec{r_i} \times \vec{v_i}}{\sum_i m_i}, \tag{2.1}$$

   where m_i, $\vec{r_i}$ and $\vec{v_i}$ are the mass, the 3D position and the 3D velocity of the i-th stellar particle in the galaxy. This allows us to obtain both, the magnitude and the direction of j_*.

2. We orient the galaxy as *face-on*, by projecting each particle position vector along de z axis, which is taken to be parallel to the direction of $\vec{j_*}$.

3. We calculate the cumulative distribution of the r band luminosity of the particles in the galaxy, as a function of the projected distance r of each stellar particle to the center of the subhalo, and then we applied a linear interpolation over the cumulative distribution to obtain the effective radius $r_{50,r}$, defined as the radius that contains half of the luminosity (or equivalently, the flux).

4. We calculate the apparent magnitude m_r considering the flux of all the particles within $r_{50,r}$, assuming that the galaxies are located at $z = 0.0485$ [1]. This value of z allows us to match synthetic images with galaxy surveys such as SDSS (York et al. 2000) and Pan-STARRS (Chambers et al. 2016). Finally, we obtain the central surface brightness of the galaxy μ_r following Zhong et al. (2008) and Bakos & Trujillo (2012) as

$$\mu_r = m_r + 2.5 \log(\pi r_{50,r}^2). \tag{2.2}$$

Traditionally the segregation between LSBGs and HSBGs is done according to the criteria established by Freeman (1970), with a canonical value of $\mu_B = 21.65$ mag arcsec^{-2}. However, it is always possible to perform this segregation employing other filters centered at different wavelengths. Particularly, different observational (e.g., Zhong et al. 2008; Bakos & Trujillo 2012) and theoretical (Di Cintio et al. 2019) studies have adopted the SDSS r-band in which to apply their selection criterion, given that this band allows a good mapping of the "underlying" stellar population, rather than recent star formation processes associated with the B-band. In this work, we employ the r-band in which to define our selection criterion, adopting a $\mu_r = 22.0$ mag arcsec^{-2} limit, as done by Di Cintio et al. (2019), which in our sample roughly corresponds to the classical threshold of $\mu_B = 21.65$ mag arcsec^{-2} established by Freeman (1970). The

[1] At this redshift, the effect of a K-correction on the apparent magnitude is negligible (about 0.04).

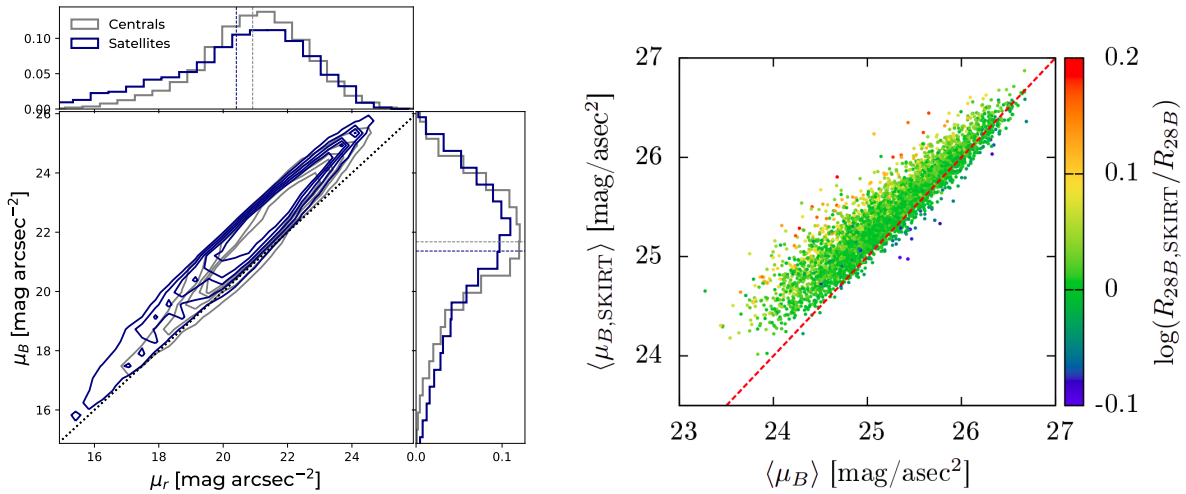

Figure 2.3: *Left:* The $\mu_B - \mu_r$ plane for galaxies with $M_* > 10^9$ M$_\odot$ in our simulated sample. *Right:* B-band surface brightness comparison including dust attenuation (y-axis) and dust-free emission (x-axis) computed for galaxies in the EAGLE cosmological simulation. [Credit: Kulier et al. (2020)]

left-hand panel of Fig. 2.3 shows the $\mu_B - \mu_r$ plane, in which galaxies in our sample reside, segregated between centrals (gray) and satellites (blue). No dust attenuation is considered, with fluxes calculated using the stellar population synthesis models by Bruzual & Charlot (2003). In a recent work presented by Kulier et al. (2020), the authors demonstrated that dust attenuation does not play a significant role in the classification of LSBGs, especially when viewed face-on. The right-hand panel of Fig. 2.3 shows the comparison between the surface brightness calculated by considering dust-free emission (x-axis) and dust attenuation (y-axis). We observe that there is a trend such that bright galaxies are more strongly affected by dust extinction, but the effect is nevertheless not strong enough to significantly change the segregation of galaxies by surface brightness.

Our full simulated sample consists of 22,554 galaxies, including 5,814 LSBGs and 16,740 HSBGs. Figure 2.4 shows the synthetic images of two galaxies in our sample, obtained by following the prescription of Rodríguez-Gómez et al. (2019). The left-hand panel corresponds to a randomly selected LSBG, while the right-hand panel shows an HSBG with similar stellar mass ($\sim 10^{10}$ M$_\odot$). We can clearly note that galaxies classified as LSBGs are more diffuse and extended objects than HSBGs.

2.2.1 Morphological properties of LSBGs

In order to segregate our sample into spiral and elliptical galaxies, we consider a kinematic criterion based on the importance of ordered rotation in the structure of the galaxy. Visual segregation like traditional bulge-to-disk decompositions drawn from photometric data are based on assumptions regarding the shape of the brightness profile of disks (usually assumed to be exponential) and spheroids (usually assumed to follow de Vaucouleurs or Sérsic profiles). These assumptions are weakly fulfilled in simulated galaxies, and kinematic decompositions can lead to different bulge-to-disk ratios when compared to photometric ones. The parameter κ_{rot} (Sales et al. 2010; Rodriguez-Gomez, et al. 2017) is defined as the ratio between the stellar kinetic energy invested into circular motion along the azimuthal component, K_{rot}, and the total stellar kinetic energy, K, i.e.

$$\kappa_{rot} = \frac{K_{rot}}{K}. \tag{2.3}$$

This quantity can be employed as a good estimator of the morphology of the galaxies in our sample. It can be observed in the left-hand panel of Fig.2.5 that κ_{rot} is correlated with the fraction of stars

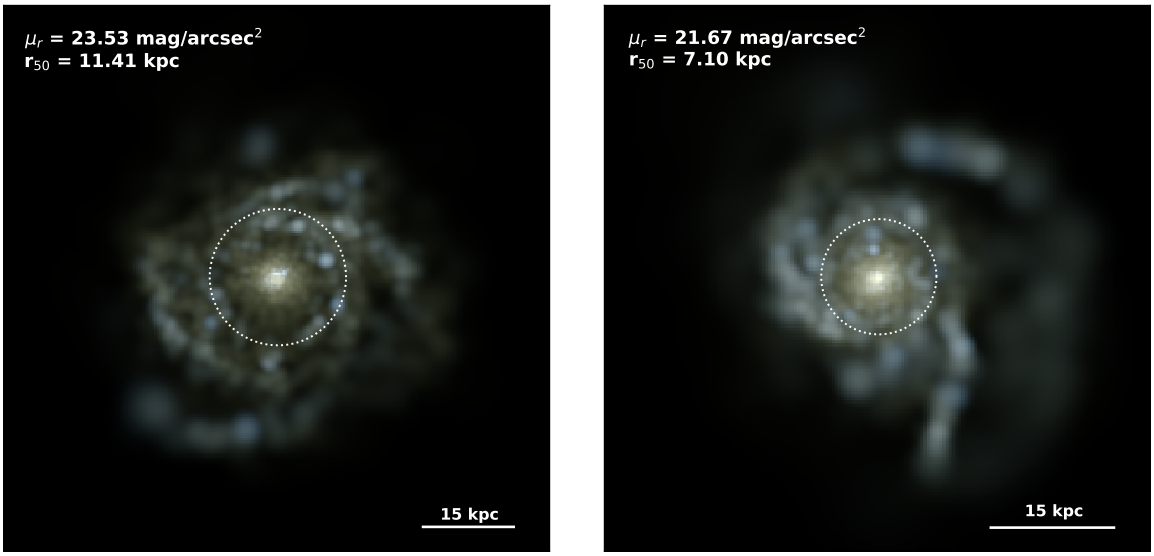

Figure 2.4: Comparison between a randomly selected LSBG (left) and an HSBG (right) of approximately the same stellar mass, $\sim 10^{10}$ $M_\odot$. The upper-left corner of each panel shows the values of the effective surface brightness (μ_r) and the r-band half-light radius (r_{50}). The dotted-line circle encloses the region delimited by r_{50}. We can observe that, despite having a similar mass, the LSBG spreads its stellar content over a larger area and therefore its surface brightness is lower. [Credit: Pérez-Montaño et al. (2022)]

with circularity $\epsilon_j > 0.5$. We remind the reader that the circularity is defined as the ratio between the component of the angular momentum which is perpendicular to the disk j_z and the angular momentum of a circular orbit whose kinetic energy is equal to the binding energy j_{circ}(E). This quantity takes values in the range $-1 < \epsilon_j < 1$, where extreme values correspond to counter-rotating and co-rotating circular orbits. The right-hand panels of Fig. 2.5 show the distribution of ϵ_j for three representative cases of simulated galaxies (Sales, et al. 2012). Top panel corresponds to a galaxy where most of the stars are in nearly circular coplanar orbits, responsible for the peak near $\epsilon_j = 1$. By contrast, bottom panel illustrates a spheroidal galaxy where ordered rotation is less prominent, making the distribution to be broad and centered around $\epsilon_j = 0$. Taken all together, the higher the values of κ_{rot}, the higher the fraction of stars with circularities associated to stars in a rotating disk. In general, $\kappa_{\rm rot}$ values above 0.5 can be considered to correspond to late-type galaxies.

It is worth mentioning that hereafter throughout this work we will refer as "spirals" to those galaxies with the presence of a disk, regardless of the presence of arms and spiral structure. In this study we are interested in those galaxies with a component modeled by an exponential profile supported by rotation. The left panel of Fig. 2.6 shows the resultant effective surface brightness μ_r (measured within one half-light radius) as a function of stellar mass, with the color code representing the median value of $\kappa_{\rm rot}$ of the galaxies within each μ_r – log(M_*) bin. The dashed line at $\mu_r = 22$ mag arcsec^{-2} indicates the limit between LSBGs and HSBGs. Black points correspond to the median value of μ_r and the error bars indicate the 16th to 84th percentile range of the μ_r distribution for the full sample. This figure shows that, for a wide range of masses ($9 \lesssim \log(M_*) \lesssim 11$), LSBGs have a predominantly spiral morphology, while HSBGs show a wide range of morphologies, with ellipticals dominating at higher masses.

2.2.2 Abundance of LSBGs in TNG100

We attempt to study the abundance of LSBGs in our sample, for such purpose, the right panel of Fig. 2.6 shows the fraction of LSBGs at a given stellar mass, including a segregation between central and

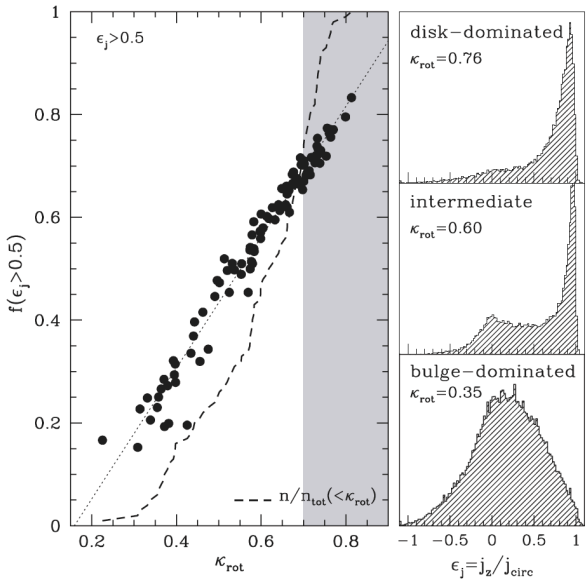

Figure 2.5: Correlation found between the κ_{rot} parameter and the fraction of stars with circularity ϵ_j >0.5. Histograms show the distribution of ϵ_j for galaxies with different values of κ_{rot} [Credit: Sales, et al. (2012)].

satellite galaxies. Central galaxies are defined as the most massive galaxy in a specific FoF group. In all cases we note that there is an important fraction of LSBGs at low masses (up to 40%), which is expected given that these objects are mainly low-mass galaxies as pointed out in previous studies (e.g. Dalcanton et al. 1997; Galaz et al. 2011). However, an upturn in this trend is observed for central galaxies at $\sim 10^{10.5}$ M$_\odot$. A possible explanation for this behaviour is presented with detail in Kulier et al. (2020). These authors argued that stellar mass accreted via mergers contributes a significant fraction of the total stellar mass of these galaxies, but they extend over larger areas as a faint component, thus making an important contribution to the LSBG population.

It should be noted that LSBGs with stellar masses above 10^{12} M$_\odot$ could have very extended components, particularly for the case of central galaxies of groups and clusters, where the inclusion of intra cluster light (ICL) could be determinant in their classification as LSBGs. In our sample we found 15 galaxies with $M_* > 10^{12}$ M$_\odot$ and $r_{50} > 30$ kpc, of which 11 are classified as LSBGs. The 30 kpc threshold is a typical boundary employed to separate the ICL contribution from the main galaxy (Schaye, et al. 2015; Pillepich et al. 2018; Henden, Puchwein, & Sijacki 2020). Even if this population is very small compared with the full sample, this is consistent with the upturn found in the right panel of Fig. 2.6. This could also partially explain the increasing LSBG fraction found by Kulier et al. (2020) at high masses, considering that they computed the surface brightness within even larger apertures, with a possibly large ICL contribution at the massive end. On the other hand, for galaxies with M_* between $10^{11.5}$ and 10^{12} M$_\odot$, we find that the fraction of galaxies with $r_{50} > 30$ kpc is less than 8%, indicating that the rest of our galaxy classification is not particularly affected by the inclusion of the ICL. Therefore, the upcoming analysis will be limited to those galaxies with stellar masses lower than 10^{12} M$_\odot$. These massive and extended galaxies are part of a different galaxy population, namely 'Giant' LSBGs (GLSBGs), which are studied in detail in an upcoming work employing TNG100 (Zhu, Pérez-Montaño, et al. in prep.).

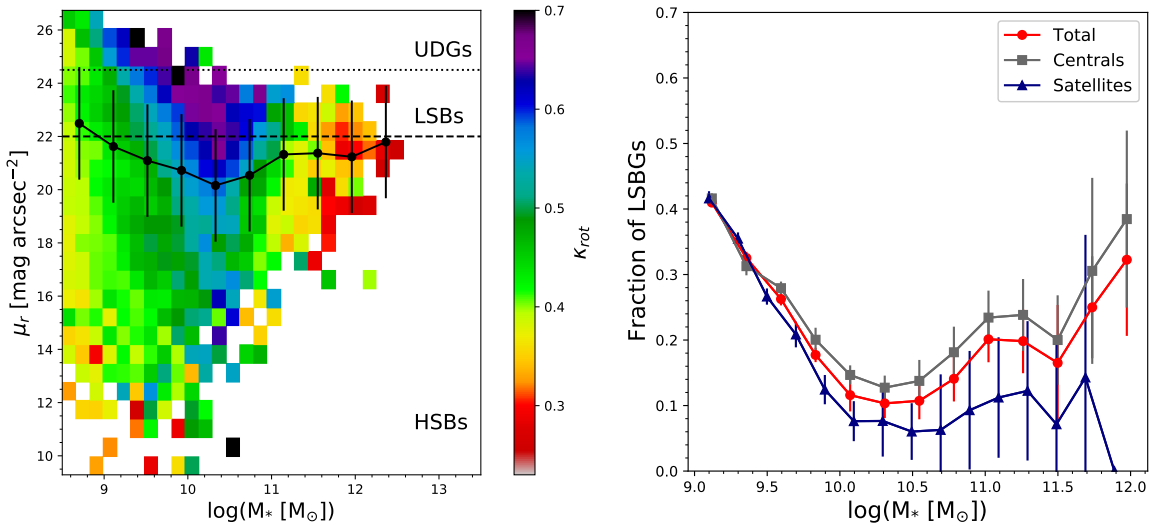

Figure 2.6: *Left Panel:* Surface brightness μ_r as a function of the stellar mass of the galaxies in our synthetic sample, color-coded by their $\kappa_{\rm rot}$ value. We observe that the LSBG population consists mainly of spiral galaxies with stellar masses lower than 10^{11} M$_\odot$, in good agreement with previous works. *Right panel:* Fraction of LSBGs as a function of stellar mass, segregated into centrals (gray squares), satellites (navy triangles), and total (red dots). [Credit: Pérez-Montaño et al. (2022)]

Chapter 3

General properties of LSBGs in TNG100

In this section we explore the nature of LSBGs in the "local" universe, employing our sample of simulated galaxies described in Chapter 2. We compare the global properties of these galaxies with the different trends found in both, observational (Zhong et al. 2008; Galaz et al. 2011; Pérez-Montaño & Cervantes Sodi 2019) and theoretical studies (Martin et al. 2019; Kulier et al. 2020; Di Cintio et al. 2019). These properties include stellar mass, luminosity, SFR, size, angular momentum, spin parameter, gas content and nuclear activity. In the following sections we present a summary of the global statistics of the main properties of galaxies, as well as a comparison with the HSBGs population. We exclude any possible mass-dependence in the interpretation of our results controlling our sample by stellar mass and/or morphology (when needed), such that any difference found in our trends may be attributed to their LSBG nature, rather than their mass or morphology. The main results of this study are published in Pérez-Montaño et al. (2022)

3.1 Global Statistics

We begin our analysis by exploring the distribution of six important physical quantities for our LSBGs and HSBGs sub-samples: the absolute r-band magnitude (M_r), the total stellar mass (M_*), the radius of the sphere containing half of the total stellar mass ($r_{\rm half}$), the projected effective radius containing 50% of the luminosity in the r-band ($r_{50,r}$), the total star formation rate (SFR), and the specific star formation rate (sSFR). Figure 3.1 shows the distributions of these galaxy properties for LSBGs (red coloured) and HSBGs (black coloured), with their mean values reported in Table 3.1, including the corresponding p-value derived from a Kolmogorov–Smirnov (K-S) test to reject the null hypothesis that the distributions were extracted from the same underlying population. Fig. 3.1 shows that LSBGs are on average less massive and fainter than HSBGs, and that HSBGs are less extended than LSBGs, quantified by their half-mass and half-light radii. On average, LSBGs have lower SFRs as one would expect given the empirical correlation between SFR and stellar mass in the galaxy population. However, the sSFR distributions are almost indistinguishable from each other, which indicates that both galaxy types have similar levels of star formation activity.

3.2 Gas content and Star Formation

From this section forward in this chapter, we will focus exclusively on central galaxies, given that for these galaxies the mass and spin parameter of the parent DM halo are well-defined properties that have a direct effect on their formation. We recall that the central galaxy of a group is determined by the SUBFIND algorithm, and usually corresponds to the most massive object. With this convention, our sub-sample

Type	M_r	$\log(M_*)$	log(SFR)	$r_{\rm half}$	$r_{50,r}$
-	*mag*	$M_\odot$	$M_\odot$ yr^{-1}	kpc	kpc
LSB	-18.906	9.515	-0.567	3.562	4.72
HSB	-19.649	9.806	-0.406	2.058	2.188
p-value	$\ll 0.001$	$\ll 0.001$	0.001	$\ll 0.001$	$\ll 0.001$

Table 3.1: Mean values of the general galaxy properties for the synthetic LSBG and HSBG samples, along with the resulting p-values from performing a K-S test for each property.

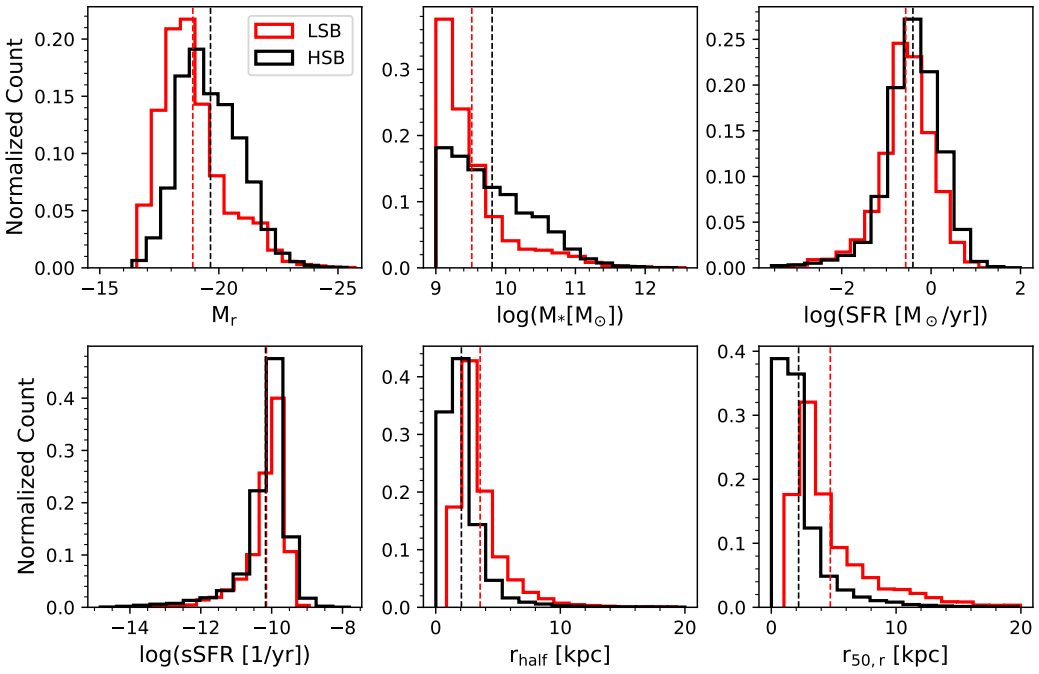

Figure 3.1: Distributions of the six main galaxy properties for LSBGs (red) and HSBGs (black) from the TNG100 simulation at $z = 0$, considering all galaxies with $M_* > 10^9\,M_\odot$. The solid lines show the overall distribution of each galaxy property, while the vertical dotted lines show the corresponding mean values. [Credit: Pérez-Montaño et al. (2022)]

of central galaxies consist of 3,238 LSBGs and 8,997 HSBGs with stellar masses between 10^9 and $10^{12}M_\odot$.

Another interesting property of LSBGs is their high amount gas. Fig. 3.2 shows the distribution of atomic (left-hand), molecular (middle) and neutral (right-hand) gas in LSBGs and HSBGs. From this figure, we can observe that, in all cases, LSBGs contain larger amounts of gas than their HSBGs counterparts. These data are obtained directly from the TNG post-processed data catalogs from Diemer, et al. (2018, 2019) for all the galaxies in the sample as a function of their stellar mass. This catalog contains post-processed modeling of atomic (HI) and molecular (H_2) hydrogen, based on the computing of radial profiles of the gas distribution in each subhalo. This results in the total mass of all the gas cells gravitationally bound to each subhalo. Five different models for the HI/H_2 transitions are included in this catalog, and the modeling was computed on both, a volumetric method and a 2D projection. The galaxy selection in the catalog was designed to be complete for both, stellar and gas mass i.e., galaxies with over a minimum value of stellar mass or gas. For TNG100, this minimum value is $2 \times 10^8 M_\odot$. In the current work, we selected the data according to the Gnedin & Kravtsov (2011) (GK11) model, in which the molecular fraction is given by

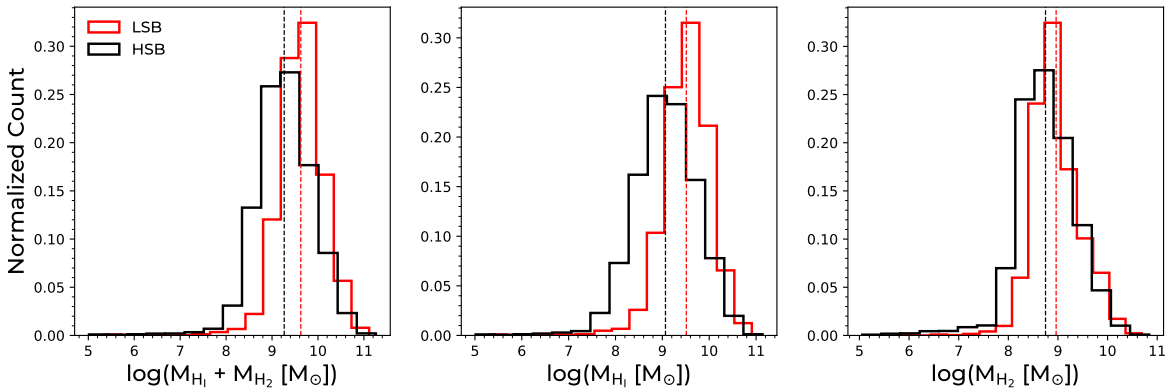

Figure 3.2: Distributions of the atomic, molecular and neutral gas masses of LSBGs and HSBGs in our simulated sample. The solid lines show the overall distribution of each galaxy property, while the vertical dotted lines show the corresponding mean values.

$$f_{mol} = \left(1 + \frac{\Sigma_c}{\Sigma_{HI+H_2}},\right)^{-2}, \tag{3.1}$$

in which the formation of molecular hydrogen is strongly linked to the dependency of the Kennicutt-Schmidt relation on the gas density, the dust-to-gas ratio and far UV radiation flux. Σ_c is a critical surface density threshold that depends only on the UV field strength and the metallicity[1]. This approximation allows us to avoid the arbitrary density and temperature thresholds typically used in star formation recipes in galaxy formation simulations. Figure 3.3 shows the average gas-to-stellar mass fractions for neutral (left), atomic (middle) and molecular (right) gas as a function of stellar mass, for the five different models included in Diemer, et al. (2018, 2019) catalogs.

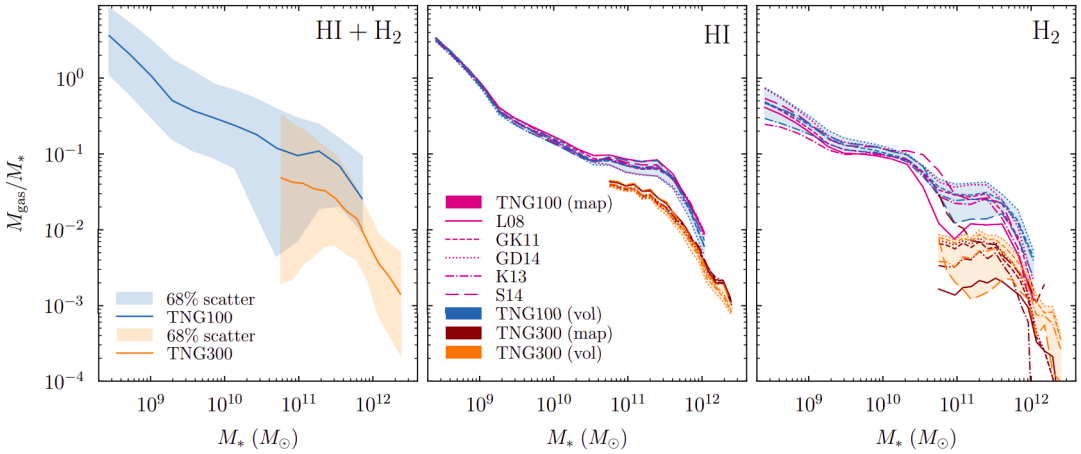

Figure 3.3: Average values of the gas-to-stellar mass fractions in TNG100 computed with the five different models employed in Diemer, et al. (2018, 2019) catalogs. Pink dashed line corresponds to the GK11 model, which is the model employed in the values reported in the current work. [Credit: Diemer, et al. (2018)]

[1]The UV field strength includes two sources: UV background and UV from young stars. Both have an strong impact on the star-formation threshold and the H_2 production rate. Metallicity, on the other hand, is related with the molecular-to-atomic gas transition. Further details available on Gnedin & Kravtsov (2011) and Diemer, et al. (2018).

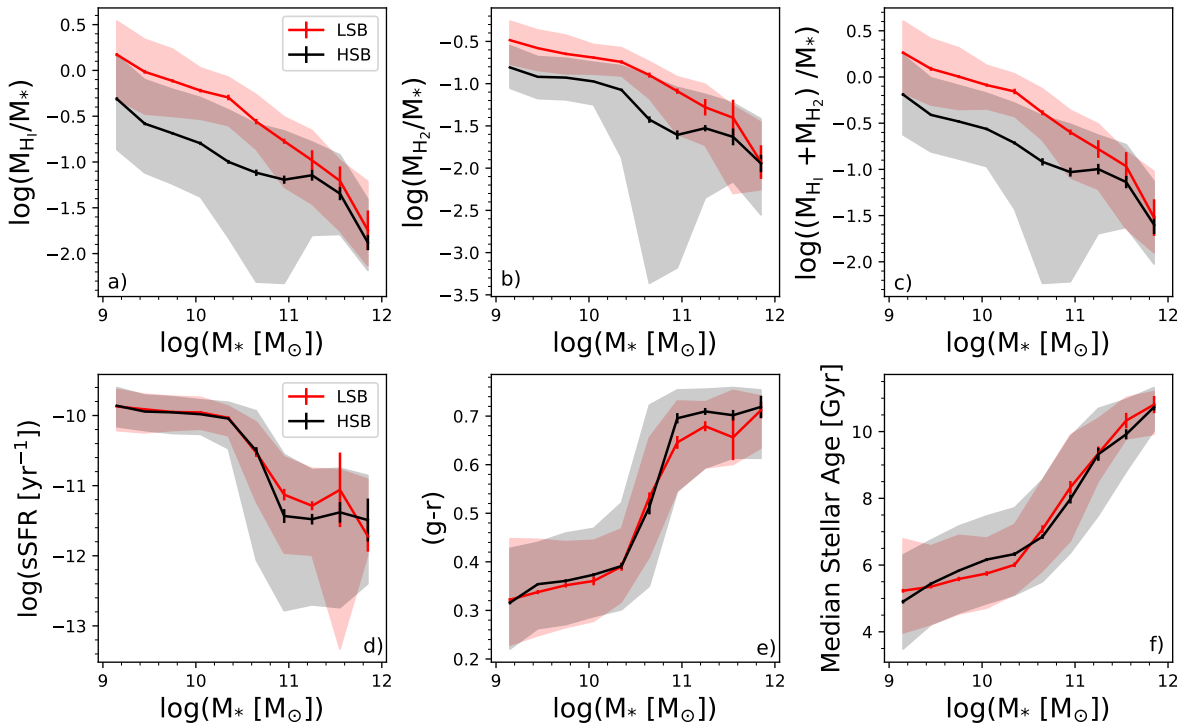

Figure 3.4: Upper panels: Atomic (a), molecular (b) and neutral (c) hydrogen gas content as a function of M_* for central LSBGs (red) and HSBGs (black) at $z = 0$. *Lower panels*: Median values of the sSFR (d), color (e) and median age of the stars (f) as a function of M_*. We can see from this plot that LSBGs present systematically higher gas fractions than HSBGs, with no significant differences between their sSFR, color, and stellar population ages. We note, however, that the sharp transitions at $\log(M_*/\mathrm{M}_\odot) \sim 10.5$ in the distributions of color and sSFR are simply a reflection of the bimodal nature (at fixed stellar mass) of those distributions. [Credit: Pérez-Montaño et al. (2022)]

Given that the stellar mass distributions of LSBGs and HSBGs are different (Fig. 3.1), we explore the differences between the two populations at fixed stellar mass, in order to control for any correlation of the particular property we are analyzing with M_*. In the upper panels of Fig. 3.4 we show the atomic, molecular and neutral gas content (left, middle and right panels, respectively). Solid lines correspond to the median value of the properties presented, whereas the shaded regions enclose the interval between the 16th and 84th percentiles. Furthermore, the error bars represent the dispersion of the median obtained from a bootstrap re-sampling algorithm, in which we performed a thousand random realizations derived from our original data set. Throughout this work, we will keep this convention for subsequent figures. For galaxies with stellar masses lower than $10^{11.5}$ $\mathrm{M}_\odot$, we clearly note that at a fixed stellar mass, LSBGs present higher atomic gas content than their HSB counterparts, in agreement with previous observational studies (e.g. O'Neil et al. 2000; Huang et al. 2012) that report a higher fraction of mass in gas of their total baryonic budget. More recently, Lutz et al. (2018) demonstrated the existence of a link between angular momentum and HI gas content, finding that HI gas-rich galaxies tend to live in halos with high angular momentum, as is the case of the LSBG population in our sample. We will investigate the link between galactic angular momentum and LSBGs in more detail in Section 3.5. Interestingly, when exploring the molecular gas content, our results are in contrast with observational studies such as Matthews & Gao (2001) and Galaz et al. (2008), who found a lack of atomic hydrogen in LSBGs. This difference may be caused either by bias in the observations, or by the methods employed in TNG for modeling the star formation. Additionally, it must be highlighted that these observational studies have only been done for a few galaxies, and not for a population large enough to perform a robust statistical analysis.

To complement these results, on the lower panels of Fig. 3.4 we present three properties related to the star formation history: the specific star formation rate sSFR = SFR/M_*, the integrated colour $(g-r)$ and the median stellar age of the star populations weighted according to the stellar mass (Rodríguez-Gómez, et al. 2016), for which the sample does not exhibit a clear distinction between LSBGs and HSBGs. This is an indication that star formation histories may not be distinguishable between LSBGs and HSBGs, however, the duration of these processes and the distribution of them along the galaxy could be different between them, as we will explore in the Chapter 4. It is important to recall the B-band traces recent star formation activity and therefore, if the identification of LSBGs is performed using a limited surface brightness in this band, this segregation will be biased to objects with recent star formation activity, and therefore, LSBGs classified according to the $B-$ band criterion will present different star formation histories when compared with HSBGs stellar populations. Additionally, if the star formation activity is not restricted to the region within the effective radius but extended to larger areas, the difference in the star formation activity between these two groups of galaxies will be evident only through a resolved exploration. We will make a detailed analysis on this in Chapter 4.

3.3 Super massive black holes and Nuclear Activity in LSBGs

It is well known that mechanisms such as AGN feedback are capable of heating gas and suppressing the star formation processes in galaxies, and some LSBGs are reported to present AGN activity (Das et al. 2006; Galaz et al. 2011). We proceed to explore the effects of AGN feedback employing the masses and accretion rates of the supermassive black holes (BHs) at the centers of LSBGs and HSBGs, as a proxy for the amount of energy ejected by the AGN.

The left panel of Fig. 3.5 shows the median value of $M_{\rm BH}$ as a function of the total stellar mass. We can observe from this plot that, at a fixed stellar mass, the BH masses of LSBGs are systematically lower than those of their high-surface-brightness counterparts, especially for those galaxies with stellar mass $M_* \leq 10^{10.5}$ M$_\odot$. This result is in agreement with some observational studies, such as Subramanian et al. (2016) and Saburova et al. (2021), who found that the BH mass estimation for LSBGs is substantially below the expected value drawn from the $M_{\rm BH} - \sigma$ relation, considering the velocity dispersion of the bulge component. Fig. 3.6 shows an example of the low-mass SMBH found in 'Giant' LSBGs from Saburova et al. (2021). In this plot, the authors show the $M_{\rm BH} - \sigma$ relation for 'giant' LSBGs and compare them to a large sample of "normal" galaxies, in which open and filled circles represent early and late-type galaxies, whereas the green line indicates the regression found by Sahu, Graham, & Davis (2019). Three of the five 'giant' LSBGs (colored symbols) deviate significantly from the regression of Sahu, Graham, & Davis (2019), while one of them lies on the limit of the 1σ range. According to the authors, this can indicate that the presence of the current gas supply to the centers of 'giant' LSBGs leading to AGN activity may be related with the accretion of material, supporting the scenario in which these galaxies are formed from accretion of cold gas from gas-rich satellites, rather than major mergers. It is important to mention that the observational samples employed by Subramanian et al. (2016) and Saburova et al. (2021) are quite small, and do not necessarily represent a robust statistic for the whole galaxy population. Interestingly, at $M_* > 10^{11}$ an upturn in the trend is observed. This could be due to the tight correlation between the mass of the SMBH and of the bulge (Häring & Rix, 2004). Looking at Fig. 2.6, we observe a transition at $M_* > 10^{11}$ between disk-dominated to bulge-dominated galaxies. Therefore, LSBGs with prominent bulges may exhibit larger $M_{\rm BH}$ than HSBGs, and this could explain the upturn in the $M_{\rm BH} - M_*$ plane.

From the theoretical point of view, the trends are in good agreement with the results of Rodriguez-Gomez et al. (2022), who found an anticorrelation between $M_{\rm BH}$ and j_*, which is expected to be higher in LSBGs. In this study also employing the TNG100 simulation, the inverse relation found between halo spin and the SMBH mass seems to be a consequence of high centrifugal acceleration present in faster rotating halos, preventing the gas to flow towards the galactic center and suppressing the accretion of material that feeds the SMBH. Lu et al. (2022) found not only lower BH accretion rates, but also less

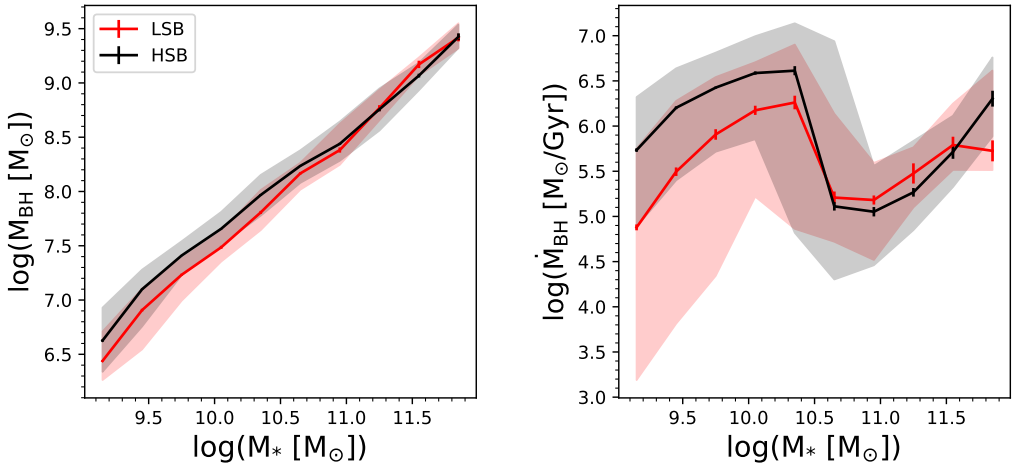

Figure 3.5: Median values of the BH mass (left) and BH accretion rate (right) of the galaxies in our sample. The color convention is the same as in Fig. 3.4. This figure shows that LSBGs host less massive BHs and have lower BH accretion rates than HSBGs (at fixed stellar mass), according to the IllustrisTNG model. Similarly to the color and sSFR distributions (Fig. 3.4), the sharp transition at $\log(M_*/\mathrm{M}_\odot) \sim 10.5$ is due to a bimodality in the distribution of $\dot{M}_{\mathrm{BH}}$ (at fixed M_*) rather than a continuous trend. For M_* larger than $10^{10.5}$, black hole mass and accretion rates are the same for LSBGs and HSBGs. [Credit: Pérez-Montaño et al. (2022)]

star formation activity at the centers of faster spinning haloes, due to the less efficient gas inflow in these systems. Fig. 3.7 shows the correlation found in Rodriguez-Gomez et al. (2022) between BH mass and halo spin for TNG100 galaxies at $z = 0$. In this scenario, BHs tend to "amplify" the effect of the halo spin, such that galaxies with lower j_* are formed at the centers of haloes with low spin parameters, but the lower centrifugal acceleration in such halos results in stronger gas accretion towards the inner parts of the galaxies, contributing to the decrease of j_* via AGN feedback.

On the right panel of Fig. 3.5, the median values of the BH accretion rate ($\dot{M}_{\mathrm{BH}}$) are presented, as a function of stellar mass. We can observe from this plot that LSBGs with $M_* < 10^{10.5}$ $\mathrm{M}_\odot$ present lower accretion rates than HSBGs. Such a trend could be explained by the higher angular momentum exhibited by LSBGs (as we will show in the following section), preventing the gas to flow towards the inner regions of these galaxies to "feed" the central BH. This last result would seem counter-intuitive given that LSBGs present a higher fraction of gas available for accretion to the central black hole, however, the high amount of angular momentum in LSBGs and the large values of the halo spin parameter spread out the distribution of gas and stars away from the center of these galaxies, resulting in lower gas densities in the vicinity of the BH and therefore reducing the amount of gas available and the accretion rate. The accretion rate implemented in TNG follows a Bondi accretion model (Bondi 1952), which depends on the surrounding gas density as

$$\dot{M}_{\mathrm{Bondi}} = \frac{4\pi G^2 M_{\mathrm{BH}}^2 \rho}{c_s^3}, \tag{3.2}$$

where M_{BH} is the BH mass, G the gravitational constant, ρ the density of the gas around the SMBH and c_s the sound speed of the gas. We can observe from eq. 3.2 that, the lower the density in the vicinity of the central BH, the lower will be the accretion rate. Therefore, we can argue that the high angular momentum in LSBGs reduces the density of the gas available for accretion, being responsible for the trend found in Fig. 3.5. Moreover, it has been shown that the presence of a high-mass BH leads to more efficient AGN feedback, disrupting late-time gas accretion. The gas accreted at late times typically has higher specific angular momentum (e.g. Übler et al. 2014), implying that higher BH masses result in lower galactic angular momentum, as previously found by different authors (e.g., Genel et al. 2015;

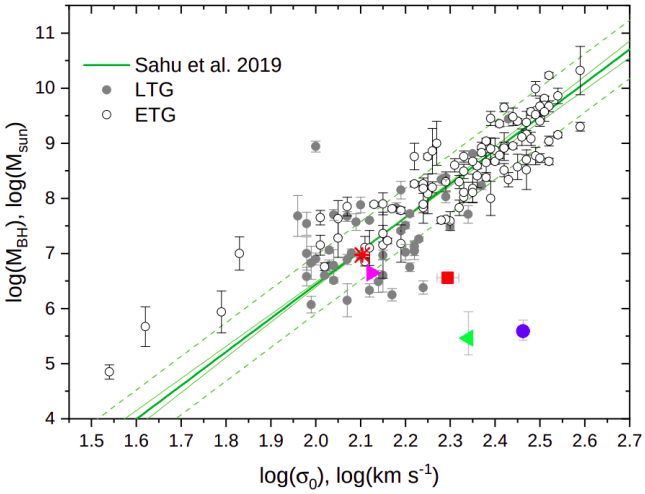

Figure 3.6: The low-mass SMBH found in a sample of giant LSBGs. Colored symbols correspond to five different examples of giant LSBGs. Open and filled circles represent early and late-type galaxies from Sahu, Graham, & Davis (2019), while the green line represents the linear fit to the $M_{\rm BH} - \sigma$ relation drawn by Sahu, Graham, & Davis (2019) considering both types of galaxies. We can observe that giant LSBGs reside systematically under the $M_{\rm BH} - \sigma$ relation, pointing out the low-mass nature of the SMBH at the center of these galaxies. [Credit: Saburova et al. (2021)]

Rodriguez-Gomez et al. 2022) and therefore favoring the formation of HSBG.

It is important to note that the non-monotonic shape of the BH accretion rate found in Fig. 3.5 is due to the different modes of AGN feedback implemented in the simulation (Weinberger, et al. 2017; Zinger et al. 2020). For galaxies in the low-mass regime, where the differences between LSBGs and HSBGs are more noticeable, the 'thermal' mode of AGN feedback is expected to be dominant, which is characterized by higher accretion rates modulated by the central gas density, which is lower for the LSBG population. This 'thermal' mode of AGN feedback is closely related with the 'retention' of angular momentum found in simulated galaxies. Genel et al. (2015) found that, in the presence of galactic winds, the angular momentum increases to a level approximately consistent with angular momentum conservation, such that gas ejected into the galactic wind typically comes back after spending some time in the halo, where it acquires angular momentum. On the other hand, in high-mass galaxies the dominant mode of AGN feedback is the so-called 'kinetic' mode, which is characterized by lower accretion rates, and typically reaches a self-regulated state where the exact value of the local gas density does not play a primary role. As also pointed out by Genel et al. (2015), quasar-mode AGN feedback hardly modifies the galactic angular momentum. Gas accreted onto halos has a higher specific angular momentum, but its accretion is suppressed by a stronger radio-mode feedback, leaving the galaxies with more early accreted baryons, which have lower specific angular momentum.

Finally, the lower occurence of stellar bars present in LSBGs (Honey et al. 2016; Cervantes Sodi & Sánchez García 2017) may also contribute to the low accretion rate and undersized BHs in these galaxies. Stellar bars promote the redistribution of mass and angular momentum between the different components of the galaxies (e.g., Hohl 1971; Weinberg 1985; Sellwood 2000; Athanassoula 2002; Martinez-Valpuesta, Shlosman, & Heller 2006), including the transference of gas towards the center of the galaxies (Shlosman, Frank, & Begelman 1989; Friedli & Benz 1993) that potentially feeds the central black hole. In a recent work, Rosas-Guevara et al. (2020) reported that the median mass of the supermassive BHs hosted by strongly barred galaxies is systematically higher than the ones hosted by unbarred galaxies, employing a simulated sample drawn also from TNG100. This is an indication that these kind of mechanisms prompted by stellar bars might be playing a role in the BH accretion process in our sample. However,

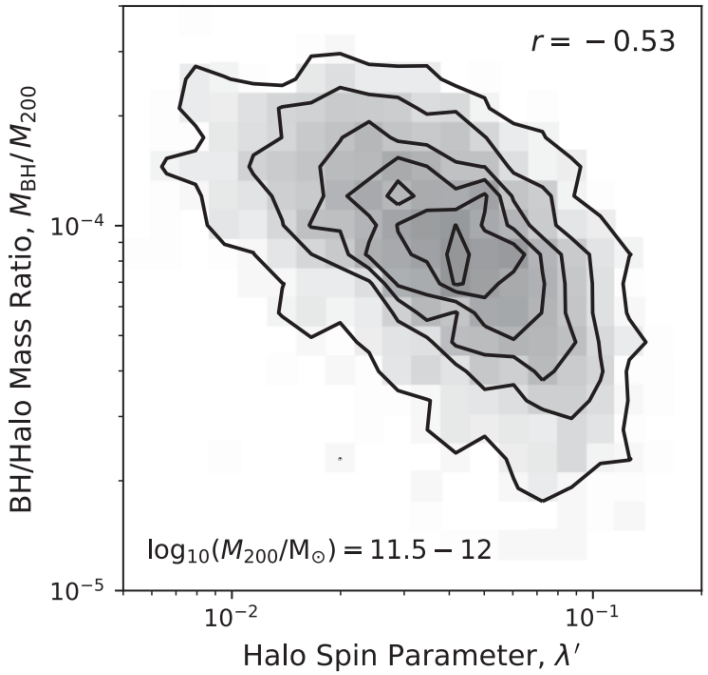

Figure 3.7: The anticorrelation between BH mass (normalized by M_{200}) and halo spin parameter for TNG100 galaxies at $z = 0$. The contours contain 5, 20, 40, 60, 80, and 95 per cent of the galaxies, while the grey-scale shows their overall distribution.[Credit: Rodriguez-Gomez et al. (2022)]

preliminary results of an upcoming work (Chim et al. in prep.) indicate that the fraction of barred galaxies with $M_* > 10^{11}\mathrm{M}_\odot$ in our simulated sample is higher than in HSBGs, which could also explain the upturn found in Fig. 3.5.

3.4 Assembly and mergers

Fig. 3.8 shows a summary of three different properties related with the merging history of the galaxies in our simulated sample. All of these quantities were calculated as described in Rodríguez-Gómez, et al. (2016). In the left-hand panel it is shown the *ex situ* stellar mass fraction, defined as the fraction of stellar mass accreted via mergers. Following the `SUBLINK` algorithim from Rodriguez-Gomez et al. (2015), a stellar particle is considered to have formed *in situ* if the galaxy in which it is formed lies along the 'main progenitor branch' of the galaxy which is currently found (at $z = 0$). Otherwise, the stellar particle is tagged as *ex situ*. The main progenitor is defined as the one with the most massive history behind it. It is important to mention that, for central galaxies, *ex situ* category does not include satellite stellar mass. We note that, in general, LSBGs present slightly higher stellar mass fractions accreted via mergers than HSBGs.

The middle panel of Fig. 3.8 shows the median value of z_{form}, defined as the redshift at which the DM halo gathered half of its final mass. The maximum total mass is not necessarily attained at $z = 0$. We observe from this panel that LSBGs had assembled half of their final mass at lower values of z, indicating that these had assembled their halos at recent epochs when compared with their HSBGs counterpart. This is consistent with what was found by Pérez-Montaño & Cervantes Sodi (2019), who found a similar trend employing a sample of galaxies drawn from the SDSS, meaning that LSBGs could be considered as a sub-population of "younger" objects, or had just experienced a recent "final" major merger, in order to establish half of its total mass. Since the halo assembly time is not directly observable, in Pérez-Montaño & Cervantes Sodi (2019) we employed an auxiliary quantity taken from Lim et al. (2016), who found

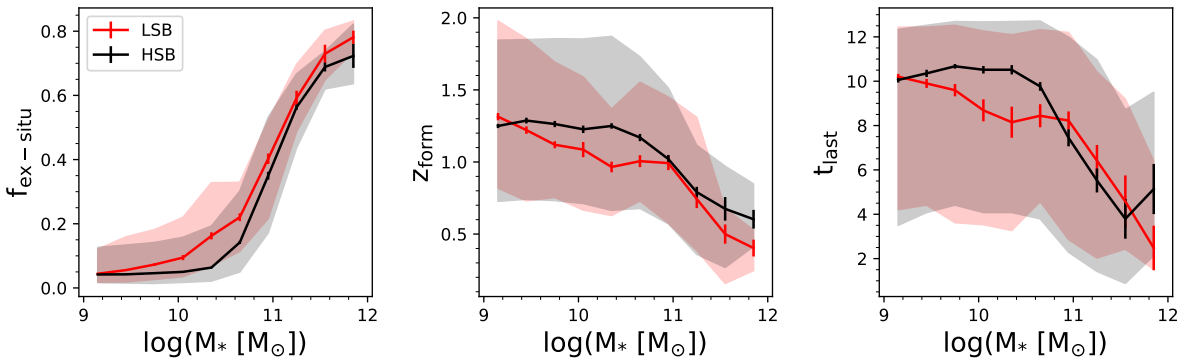

Figure 3.8: Median values of the fraction of the stellar mass accreted via mergers (left), redshift at which half of the final halo mass has assembled $z_{\rm form}$ (middle) and elapsed time since the last major merger $t_{\rm last}$ (right) for all the galaxies in our synthetic sample. This figure supports the idea that galaxy mergers favour the formation of LSBGs, but are probably not the dominant factor. [Credit: Pérez-Montaño et al. (2022)]

a tight correlation between the assembly time and the fraction $f_c \equiv M_{*,c}/M_h$, which can be used as a proxy of $z_{\rm form}$, and where $M_{*,c}$ is the stellar mass of the central galaxy of the group and M_h its halo mass. Finally, the right-hand panel shows the time since the last major merger occurred. Mergers are identified as described in Rodriguez-Gomez et al. (2015), at the time when the secondary progenitor reaches its maximum stellar mass, $t_{\rm max}$, and its checked to has a well defined 'infall' moment, defined as the time in which a satellite galaxy crosses the virial radius of its current host for the last time.. Major mergers are defined as those in which the merger mass ratio, defined as the ratio between the lowest and highest progenitor masses at $t_{\rm max}$ is larger than 1/4. We observe that for a restricted range of stellar masses, occurred between 10^9 and 10^{11} $M_\odot$, LSBGs experienced their last major merger more recently.

All together, the presented results are consistent with many other studies obtained employing simulations. For example, Zhu, et al. (2018) find that the formation of a massive LSBG such as Malin-1 is due to the encounter of a gas-rich massive galaxy with another gas-rich galaxy, but with lower stellar mass. Additionally, Di Cintio et al. (2019) argue that certain merger configurations, such as coplanar mergers, are able to increase the angular momentum of a galaxy, leading to a decrease of its surface brightness. The main conclusion drawn from these works is that mergers could play an important role in the formation of LSBGs, depending on many different factors such as the direction of the merger, the angular momenta of the galaxies prior to the merger, the alignment of the galaxies involved, their gas content, and also their morphologies. Interestingly, our results seem to be in contrast with other studies, such as Martin et al. (2019), who found that both LSBGs and HSBGs undergo very few mergers at low redshift, and therefore mergers are unlikely to be the principal driver of LSBGs evolution over cosmic time. The authors argue, according to their findings, that tidal perturbations and ram-pressure stripping may be the main mechanisms of LSBGs formation at low redshifts, rather than merger phenomena.

3.5 Angular momentum and Spin parameter

One of the most important physical parameters determining the low surface brightness nature of these systems is the galactic angular momentum, which is related to the spin parameter λ of the parent DM halo (e.g. Teklu et al. 2015; Rodriguez-Gomez et al. 2022). In the top-left panel of Fig. 3.9 we show the median value of the stellar specific angular momentum j_* as a function of the stellar mass M_*, in which we observe that LSBGs present systematically higher values of j_* across the entire stellar mass range of the sample, in agreement with findings from observational samples of nearby galaxies (e.g. Pérez-Montaño & Cervantes Sodi 2019; Salinas & Galaz 2021). Interestingly, Martin et al. (2019) found that LSBGs and HSBGs have similar distributions of j_*. We attribute the difference between our result and theirs to the

fact that we are comparing the HSBG and LSBG populations at fixed stellar mass, while they compared the whole galaxy populations without controlling for M_*.

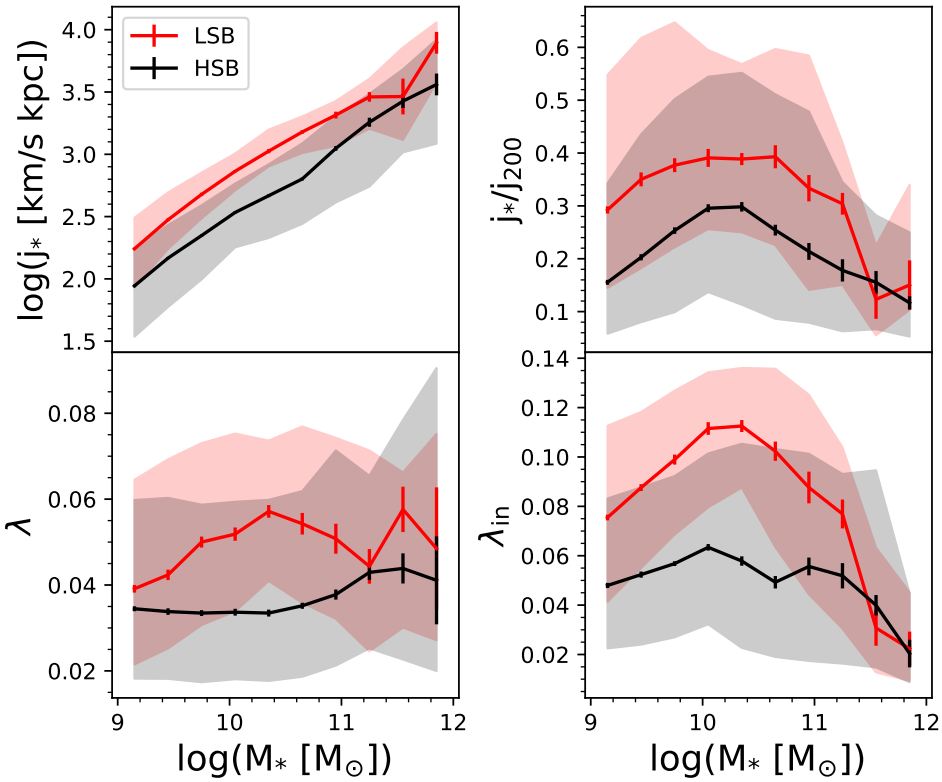

Figure 3.9: Median values of the stellar specific angular momentum j_* (top-left), angular momentum retention fraction j_*/j_{200} (top-right), halo spin parameter λ (bottom-left), and *inner* halo spin parameter (bottom-right) as a function of stellar mass M_*, shown for all the galaxies in our sample. This figure shows that LSBGs have systematically higher stellar specific angular momentum than HSBGs (at fixed stellar mass), as a result of forming inside faster-spinning DM haloes and 'retaining' a larger fraction of their specific angular momentum. [Credit: Pérez-Montaño et al. (2022)]

In the bottom-left panel of Fig. 3.9 we plot the median value of the halo spin parameter λ, computed using a proxy for the Peebles (1971) definition proposed by Bullock, et al. (2001), so that eq. 1.7 could be re-written as

$$\lambda = \frac{j_{200}}{\sqrt{2} R_{200} v_{200}}, \tag{3.3}$$

where j_{200} is the specific angular momentum of all the components within R_{200}, R_{200} is the radius where the mean density is 200 times the critical density of the Universe, and v_{200} is the circular velocity at $R = R_{200}$. From this, we note that LSBGs have higher values of λ, in agreement with the classical picture where LSBGs are formed within haloes with high values of the spin parameter (Dalcanton et al. 1997; Boissier et al. 2003; Kim & Lee 2013; Pérez-Montaño & Cervantes Sodi 2019). The bottom-right panel of Fig. 3.9 shows the median value for the spin parameter in the inner part of the halo $\lambda_{\rm in}$, computed within a radius equal to $R = 0.1\ R_{200}$. This quantity is important because the stellar morphology of a galaxy is more closely connected to $\lambda_{\rm in}$ than to the value obtained for the whole configuration (Zavala et al. 2016). The difference in $\lambda_{\rm in}$ between LSBGs and HSBGs appears to be more significant than the difference in λ, being LSBGs the ones with higher spin parameter. It is important to note that the $\lambda_{\rm in}$ values measured directly from a hydrodynamic simulation should be interpreted with caution, since the

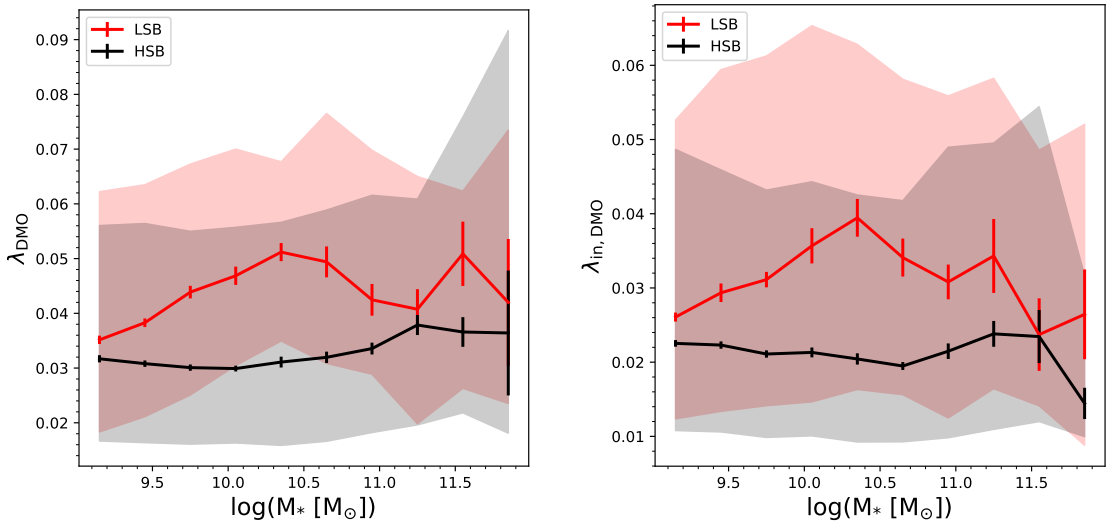

Figure 3.10: Median values of the halo spin parameter λ (bottom-left), and *inner* halo spin parameter (bottom-right) as a function of stellar mass M_* obtained by matching the halos of TNG100 with their DM-only counterpart.

baryonic component of the galaxy contributes significantly to the measured value of the spin parameter at the innermost parts of the DM halo, enlarging the values of $\lambda_{\rm in}$ by a factor of ~ 2.

In order to exclude a possible 'back reaction' effect of baryons on the DM halo spin, we have repeated this analysis by matching haloes from TNG100 to their counterparts from an analogous DM-only simulation, following the methodology described in Rodriguez-Gomez, et al. (2017), i.e., for each subhalo, the 'matched' subhalo candidates in the DM-only simulation are defined as those which have at least one DM particle in common. For each subhalo, the merit function

$$\chi = \sum_j (R_{j,\rm FP}^{-\alpha} + R_{j,\rm DMO}^{-\alpha}) \tag{3.4}$$

is calculated, where $R_{j,\rm FP}^{-\alpha}$ and $R_{j,\rm DMO}^{-\alpha}$ are the binding energy ranks[2] of the jth DM particles in the full-physics (FP) and DM-only (DMO) runs, and the sum is carried out over all common DM particles. The same matching procedure is applied in reverse, by matching subhaloes from the DMO simulation to their counterparts in the FP run. Those subhaloes with a bijective match are stored in the matching catalogs. Further details on the matched halo catalogs are available in Rodriguez-Gomez, et al. (2017). We found no significant differences on the values of the total spin parameter shown in the bottom-left panel of Fig. 3.9 with the values shown in the left-hand panel of Fig. 3.10, which shows the same trend presented in the bottom-left panel of Fig. 3.9, but considering the spin parameter drawn from the DM-only simulation, $\lambda_{\rm DMO}$.

Following a similar procedure, if we instead use $\lambda_{\rm in}$ values from matched haloes in the DM-only simulation, we find that the $\lambda_{\rm in}$ values decrease by a factor of $\sim$2–3 and the differences between LSBGs and HSBGs become comparable to those for the total halo spin, as shown on the right panel of Fig. 3.10. The behaviour of our sample is qualitatively consistent with the results by Kulier et al. (2020) using the EAGLE simulation as we can observe in the top, right-hand panel of Fig. 1.18, in which clearly LSBGs exhibit higher spin parameter than HSBGs, at fixed stellar mass.

[2]The energy rank is a number that represents how gravitationally bound the particles are. Is not a physical quantity, but a "ranking" such that particles are ordered not by mass, but by binding energy.

In the work of Fall (1983) and its subsequent revisions (Romanowsky & Fall 2012; Fall & Romanowsky 2013), it is shown that both elliptical and spiral galaxies follow roughly parallel tracks on the $j_* - M_*$ plane, with the latter having a specific stellar angular momentum about 5 times larger than the former at a fixed stellar mass. Additionally, it has been found, using hydrodynamical simulations (Kimm et al. 2011; Stewart et al. 2013; Zjupa & Springel 2017) that the specific angular momentum of the baryonic component of the galaxies is higher than that of the DM component. Teklu et al. (2015) and Zavala et al. (2016) found a correlation between j_* and j_{200}, with a strong dependence with the morphology of the galaxies, with disk-dominated systems retaining a higher amount of angular momentum, as described by Fall & Romanowsky (2013). Using the Illustris simulation, Genel et al. (2015) found that, for spiral galaxies, the retention of angular momentum (j_*/j_{200}) is consistent with 100%, whereas for early-type galaxies it is only 10-30%. Similarly, using the TNG100 simulation, Rodriguez-Gomez et al. (2022) found retention fractions of 50–60% for late types and 10–20% for early types.

With these results in mind, we then explored whether there is a difference in the retention fraction of angular momentum between the two sub-samples in our study. The top-right panel of Fig. 3.9 shows the median value of j_*/j_{200} as a function of the stellar mass. We note that throughout the full range of stellar masses explored, LSBGs retain a higher amount of angular momentum than HSBGs. Recently, Rodriguez-Gomez et al. (2022) showed that the angular momentum retention fraction is a strong function of κ_{rot}, as observed in Fig. 3.11 while being mostly independent of stellar mass for the individual morphological types. Given that the LSBGs of our sample are mostly late-type (as seen in Fig. 2.6), the systematically higher values of j_*/j_{200} are mostly a result of their morphology, rather than their intrinsic low surface brightness. The difference between LSBGs and HSBGs in the retained fraction of angular momentum by the stellar component, combined with the higher values of the halo spin parameter, could be important in the formation of LSBGs.

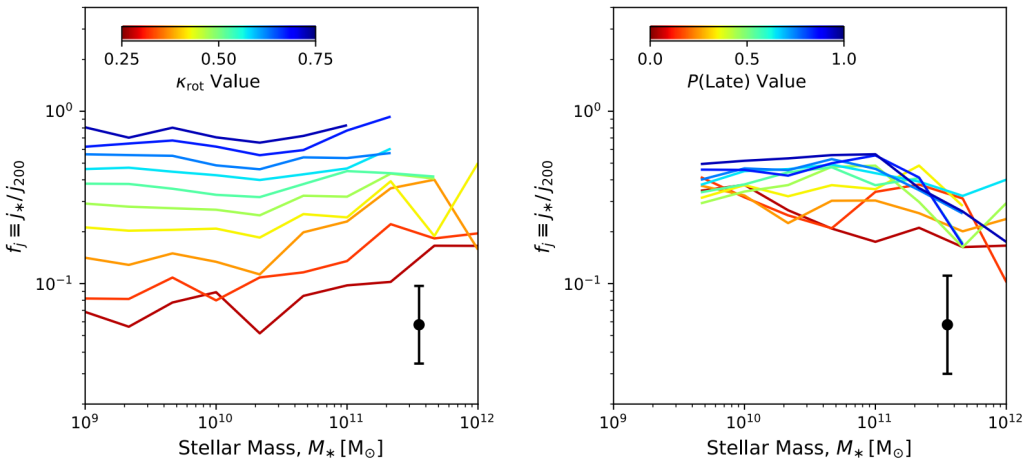

Figure 3.11: The specific angular momentum retention fraction ($f_j = j_*/j_{200}$) plotted against stellar mass for IllustrisTNG central galaxies at $z = 0$. The different colored lines correspond to different actual values of κ_{rot} (left) compared to a visual-like classification P(Late) (right). [Credit: Rodriguez-Gomez et al. (2022)]

3.6 Halo properties and Baryon content

We continue our study by analyzing the DM content of LSBGs, and how their baryonic and stellar content differs from that of HSBGs. We perform a similar exercise to that in the previous sections, studying the median values of the stellar-to-halo and baryonic-to-halo mass ratios, M_*/M_{200}, in a similar way as Kulier et al. (2020). The left-hand panel of Fig. 3.12 shows the median values of M_*/M_{200} (where M_{200} is the total mass within R_{200}) as a function of stellar mass, in which we observe that LSBGs

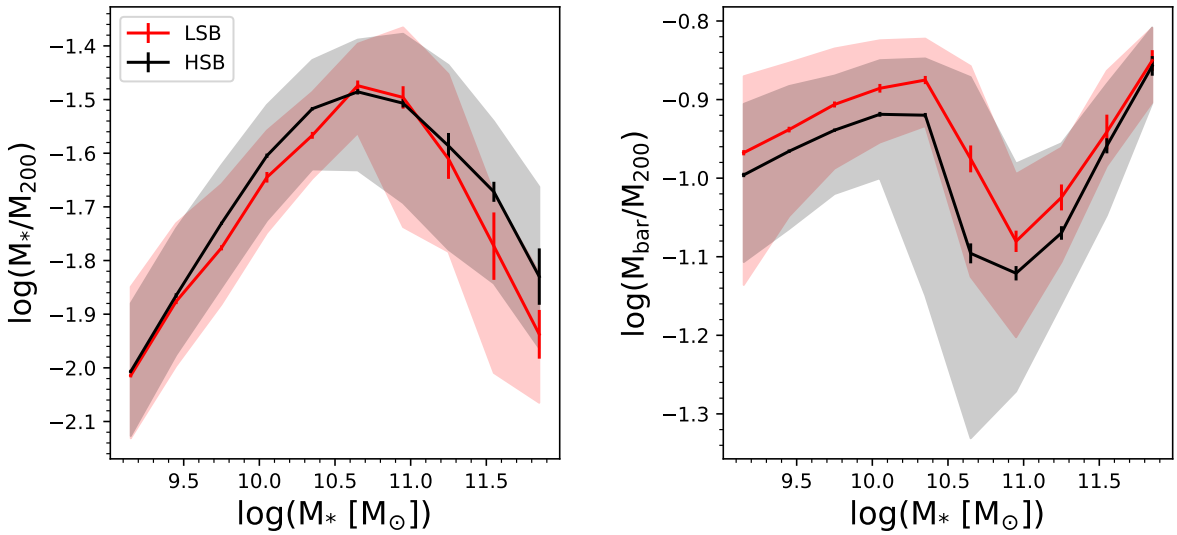

Figure 3.12: Median values of the stellar-to-halo (left) and baryonic-to-halo (right) mass ratios as a function of stellar mass, shown for all central LSBGs and HSBGs at $z = 0$. At fixed stellar mass, LSBGs are formed within slightly more massive DM haloes with higher gas content than those hosting HSBGs. We also note that the joint distribution of $M_{\rm bar}/M_{200}$ and M_* is bimodal, resulting in a sharp transition at $\log(M_*/{\rm M}_\odot) \sim 10.5$. [Credit: Pérez-Montaño et al. (2022)]

present a marginally smaller stellar-to-halo mass fraction compared to HSBGs. To complement this analysis, the left-hand panel of Fig. 3.13 shows a set of isocontours for different fractions of LSBGs in a given $M_*/M_{200} - M*$ bin, obtained by dividing the parameter space into 10×10 bins, and applying a spline kernel to get a smooth transition, requiring at least fifteen galaxies per bin to estimate the LSBGs fraction. This plot shows a systematic increase of the fraction of LSBGs with stellar mass of the galaxies, but also a dependence on the stellar-to-halo mass fraction; at fixed stellar mass, the fraction of LSBGs decreases with increasing values of M_*/M_{200}. This is another way to visualize our previous conclusion, in which LSBGs are more dark-matter dominated systems when compared with the HSBGs population, in good agreement with previous studies (Pickering et al. 1997; McGaugh, Rubin, & de Blok 2001; Pérez-Montaño & Cervantes Sodi 2019) mentioned in chapter 1.

Analogously, the right-hand panel of Fig. 3.12 shows the median value of the baryonic-to-halo mass ratio, where $M_{\rm bar} = M_* + M_{\rm gas}$. We can observe that, for galaxies with stellar masses up to 10^{11} M$_\odot$, LSBGs have higher baryonic-to-halo mass ratio than HSBGs, similar to the trend presented by Kulier et al. (2020). These authors found no difference in the stellar-to-halo mass ratio, but found a clear difference in the baryonic-to-halo mass ratio between LSBGs and HSBGs. They argued that, given that LSBGs are formed within haloes with similar mass at fixed stellar mass, the excess in the baryonic budget must consist of gas. As we did before, the right-hand panel of Fig. 3.13 show similar isocontours of the LSBGs fraction, but in the $M_{bar}/M_{200} - M_*$ plane. We can observe that, in the region in which most of the galaxies are located, we do observe that the fraction of LSBGs increases for galaxies with higher baryonic content, at fixed stellar mass. From this, we can conclude that most of the baryonic-excess has not been converted yet into stars in LSBGs.

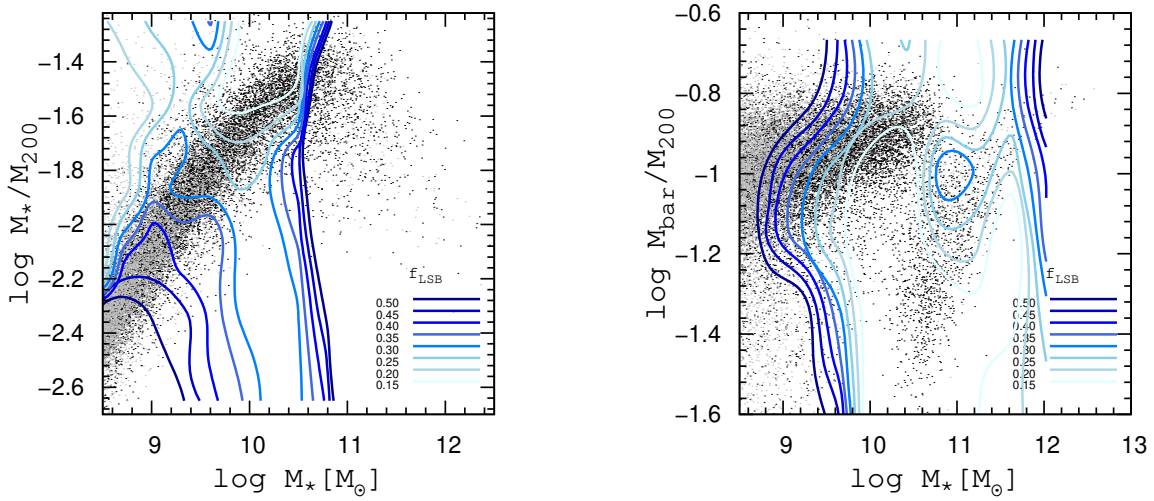

Figure 3.13: *Left panel*: LSBGs fraction f_{LSB} iso-contours in the M_*/M_{200} - M_* plane. Contours denote regions of constant f_{LSB}. *Right panel*: Same as before, but for the galaxies in the M_{bar}/M_{200} - M_* plane. These two combined support the idea that LSB galaxies are strongly dominated by DM, and they probably evolve more slowly than their HSB counterparts. [Credit: Luis Enrique Pérez-Montaño]

Chapter 4

Redshift Evolution of LSBGs

In this section we study the evolution of the galaxies in our sample using the `SubLink` merger trees (Rodriguez-Gomez et al. 2015) for the LSBGs and HSBGs selected at $z = 0$. We first describe briefly the algorithm employed in TNG to characterize the merger trees, includying a brief description of the `SUBLINK` algorithm. Then we track the redshift evolution of the main properties studied in Sections 3.1 and 3.5, and then follow their resolved star formation histories (SFHs). Throughout this section we select galaxies in three different stellar mass ranges, centred at 10^9, 10^{10} and 10^{11} $M_\odot$, at $z = 0$.

4.1 Merger Trees

As was mentioned in Chapter 2, the semi-analytic approach employed in the different galaxy formation models is an attempt to describe the formation history of galaxies and gas within dark matter halos, including hydrodynamics, star formation, supernova/AGN feedback, stellar population synthesis and galaxy merging. Within the currently accepted ΛCDM cosmology, the assembly of dark matter halos is given by merging small clumps to form larger objects. Galaxies initially form in their own halo and are traced as they are incorporated into larger haloes and eventually, merge with other galaxies. A halo of given mass may have a variety of merging histories, and the properties of galaxies that form within this halo presumably depend, to some extent, on the details of this history. This merging history can be traced in cosmological simulations and stored in what we know as "Merger Trees", which involves tracing the masses of progentor haloes and the redshifts at which they merge to form larger haloes. Fig. 4.1 provides an illustrative example of how halo merger histories are traced back in time employing high resolution $N-$body simulations. This figure illustrates the evolution of a dark matter halo of $8.9\times10^{14}M_\odot$ at $z = 0$ corresponding to an example of the so-called Brightest Cluster Galaxies (BCGs), which are the very luminous galaxies that inhabit the cores of rich galaxy clusters. The halo of interest is located at the top of the plot while all its progenitors are plotted backwards in time. The size of the symbols scales with stellar mass, color-coded by galaxy $B - V$ color. In this case, the evolution of the BCG can be characterized by a series of accretion events of smaller objects that do not introduce major changes in the identity of the BCG itself.

For galaxies in TNG, the code for creating subhalo merger trees has been featured in the *Sussing Merger Trees* comparison project (Srisawat et al. 2013; Avila et al. 2014; Lee et al. 2014), where it is refered as `SUBLINK`. This algorithm is fully descibed in detail in Rodriguez-Gomez et al. (2015), however, in this section a brief summary of how the algorithm works is presented. `SUBLINK` employs a methdology similar to the one described in Springel et al. (2005c) and Boylan-Kolchin et al. (2009), with sligth modifications in the determination of descendants and a different definition of the *first progenitor*. Merger trees can be constructed for different particle types, such as dark matter, stars and star-forming gas. Two varieties of merger trees are defined in `SUBLINK`:

1. DM-only: Follow exclusively the dark matter particles of a simulation.

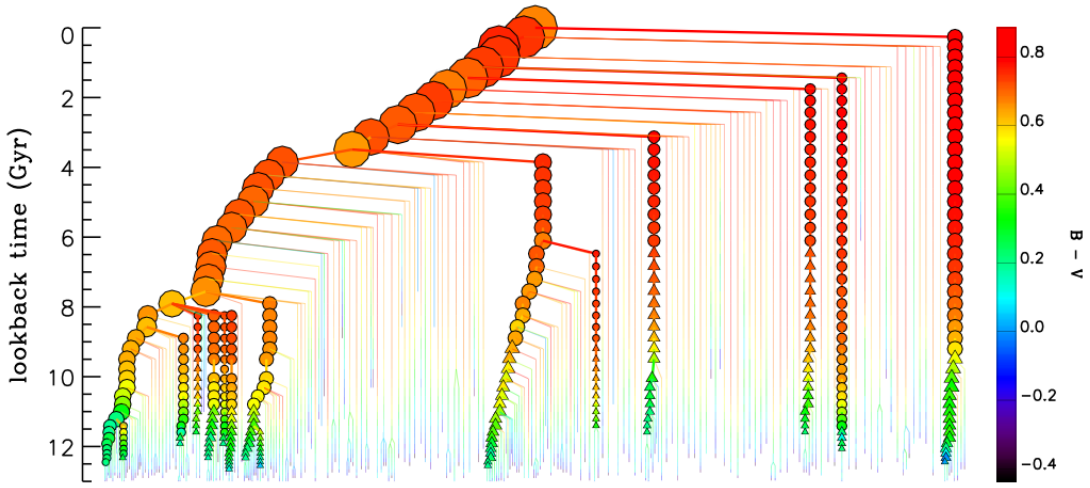

Figure 4.1: Merger history of an example of BCGs with a given dark matter halo mass of $8.9\times10^{14}\mathrm{M}_{\odot}$ at $z = 0$. Symbols are colour-coded by the galaxy $B - V$ colour, and their sizes scale with the stellar mass. Circles correspond to galaxies that reside in the FoF group inhabited by the main branch, while triangles represent galaxies that have not yet joined this FoF group.[Credit: De Lucia & Blaizot (2007)]

2. Baryonic: Follow the star particles plus the star-forming gas elements in the simulation[1].

It is important to point out that following a gas cell is not completely equivalent to following collisionless stellar or DM particles. Therefore, `SUBLINK` assumes that star-forming gas cells typically found in central denser regions of subhalos are able to preserve their 'identity' over a few snapshots, adding valuable information when determining the descendant of a given subhalo. Including star-forming gas together with stellar particles is very useful to construct robust merger trees at high redshifts, where galaxies have huge amounts of gas.

For each subhalo, a *unique* descendant is assigned as an approximation of the hierarchical buildup structure in ΛCDM cosmogonies. At a given snapshot, those subhalos that have common particles with another specific subhalo in the following snapshot are identified as 'descendant candidates'. The unique descendant of the subhalo in question is defined as the descendant candidate with the highest 'score', which is based on the merit function

$$\chi = \sum_{j} (R_j^{-1}), \tag{4.1}$$

where R_j denotes the binding energy rank of particles from a given subhalo which are also found in the descendant subhalo. In the case of baryonic merger trees, the mass of the resolution elements m_j must be included in eq. 4.1 such that $R_j^{-1} \rightarrow m_j R_j^{-1}$. The unique descendant of the subhalo in question is defined as the descendant candidate with the highest score. It is important to point out that an exponent of -1 in eq. 4.1 allows the algorithm to follow subhaloes more robustly in major merger scenarios, particularly when three or more objects of comparable sizes and densities are interacting.

We say that a subhalo A is a progenitor of subhalo B if and only if B is the descendant of A, in this sense, note that a single subhalo can have many progenitors, but at most a single descendant, as it is established in the hierarchical buildup of structure in the Universe. Once all the descendant connections have been made, the first progenitor of each subhalo is defined as the one with the 'most massive history' behind it, removing the arbitrariness in defining the first progenitor as simply 'the most massive' object, which is subject to noise when, for example, the two largest progenitors have similar masses. As a result,

[1]Defined as those gas cells with hydrogen particle density above 0.13 cm^{-3}

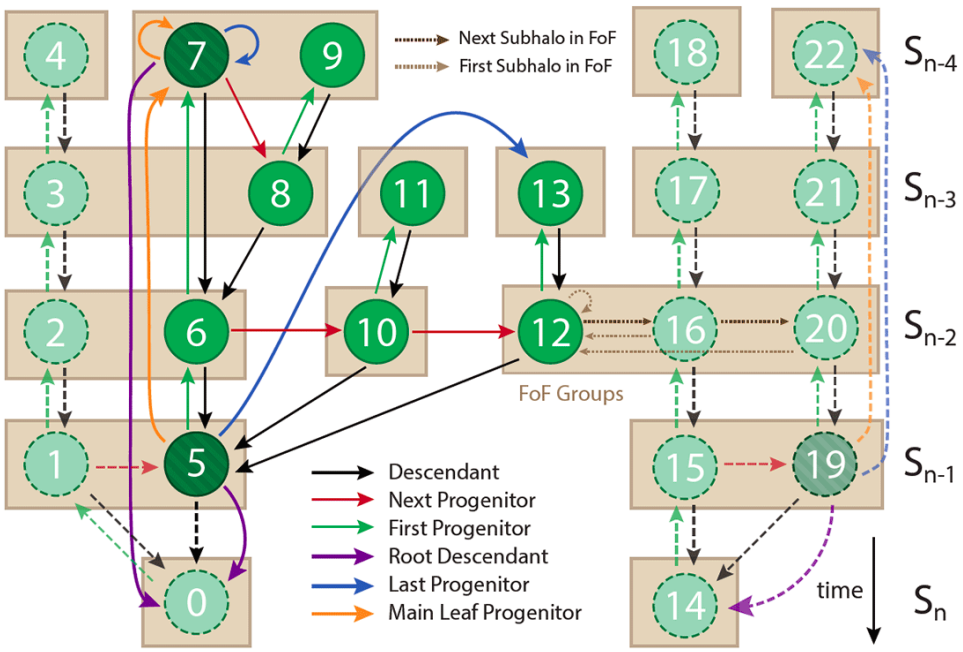

Figure 4.2: Schematic diagram of the merger tree structure, which connects subhalos across different snapshots in the simulation. Each row indicates a single snapshot, with time increasing downwards. Green circles represent subhalos (the nodes of the merger tree), while beige boxes indicate their parent FoF groups. The descendant (black arrows), first progenitor (green arrows), and next progenitor (red arrows), are shown for all subhalos. [Credit: The IllustrisTNG project official website]

the mass history of any particular galaxy or halo can be robustly compared across simulations. Knowledge of all the subhalo descendants, along with the definition of the first progenitor, determines the merger trees. Taking all together, merger trees are constructed as follows. First, a linked-list is created for the whole simulation, assigning to each subhalo five 'key' subhaloes:

i) First progenitor: The progenitor of the subhalo which has the most massive history behind it.

ii) Next progenitor: The subhalo which shares the same descendant as the subhalo in question, which has the next largest mass history behind it.

iii) Descendant: The unique descendant of the subhalo in question.

iv) First subhalo in FoF group: The main subhalo (the one with the most massive history behind it) from the same FoF group as the subhalo in question.

v) Next subhalo in FoF group: The next subhalo from the same FoF group, in order of decreasing mass history.

Secondly, each tree is defined as a set of subhaloes that are connected by progenitor/descendant links or by belonging to the same FoF group. Two subhalos belong to the same tree if and only if they can be reached successively following the pointers described above. The resulting trees are completely independent from each other, allowing easy parallelization of computational post-processing tasks. Fig. 4.2 shows a schematic diagram of the structure of the `SubLink` merger trees, in which the main associations, namely the 'first progenitor', 'next progenitor' and 'descendant' are indicated by green, red and black arrows respectively. The number inside each circle represent the unique ID of the corresponding subhalo. In this example, the main progenitor branch of the subhalo 0 is composed of the subhalos 1-4,

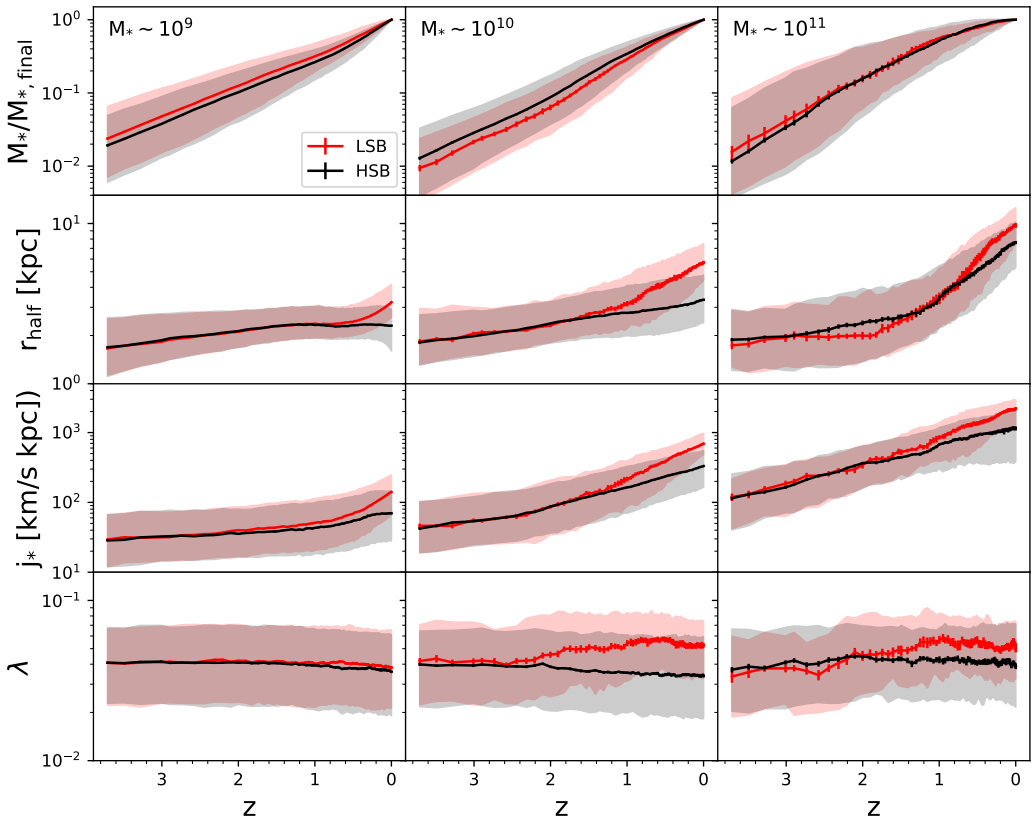

Figure 4.3: Median evolutionary tracks for the fraction of the final stellar mass (top row), galaxy size (second row), stellar specific angular momentum (third row) and halo spin (bottom row) for IllustrisTNG galaxies. The columns from left to right correspond to different stellar mass bins at $z = 0$, corresponding to (0.7-1.4)$\times 10^{9,10,11}$ $M_\odot$. The shaded regions indicate the 16th to 84th percentile ranges, while the red and black lines correspond to LSBGs and HSBGs, respectively. The progenitors of LSBGs become systematically larger and acquire higher stellar specific angular momentum than the progenitors of HSBGs at $z \sim 0.5$–1.5. The segregation in the halo spin parameters of LSBG and HSBG progenitors takes place at an earlier redshift, around $z \sim 2$. [Credit: Pérez-Montaño et al. (2022)]

while the main progenitor of 5 is composed of the subhalos 6 and 7, but the 5-7 branch is the next progenitor of 0. The full progenitor history, and not just the main branch, requires following both the first and next progenitor links. In this way the user can identify all subhalos at a previous snapshot which have a common descendant.

4.2 Size, mass and angular momentum evolution

Fig. 4.3 shows the median values of the current-to-final stellar mass ratio ($M_*/M_{*,\mathrm{final}}$, top row), the radius containing half of the total stellar mass (second row), the specific angular momentum of the stellar component (third row) and the halo spin parameter (bottom row) as a function of redshift for LSBGs (red lines) and HSBGs (black lines). The panels from left to right include galaxies selected according to their $z = 0$ stellar mass in three different intervals of $(0.7 - 1.4) \times 10^9$, 10^{10} and 10^{11} $M_\odot$. The evolutionary tracks are built taking into account the values of $M_*, r_{\mathrm{half}}, j_*$ and λ of a given subhalo at $z = 0$, and then we follow the evolution of these quantities by linking the current subhalo with its corresponding 'First progenitor' at every snapshot, such that the evolution follows the main branch of the current $z = 0$

subhalo.

From the first row in Fig. 4.3, we can observe that there is no significant difference in the stellar mass formation history between LSBGs and HSBGs, implying that both populations of galaxies may follow, in principle, similar stellar assembly processes. On the second row of Fig. 4.3, we plot the median values of the redshift evolution of $r_{\rm half}$, which show a clear bifurcation at $z \sim 0.5$–1.5, where LSBGs begin to exhibit larger radii than HSBGs, resulting in the more extended radii observed at $z = 0$ in LSBGs (see Fig. 3.1). A similar behaviour is found by Martin et al. (2019), who found a particular divergence in the effective radii between LSBGs and HSBGs. Similar to what we observe in the second row of Fig.4.3, these authors found that the evolution of the effective radii is not abrupt, but relatively smooth with time, supporting the idea that large radii found in LSBGs today are unlikely to be the result of violent events at early epochs. Fig. 4.4 shows the effective radii evolution of the main progenitors of LSBGs and HSBGs in the sample of Martin et al. (2019), in which it is observed that the former are consistently larger on average.

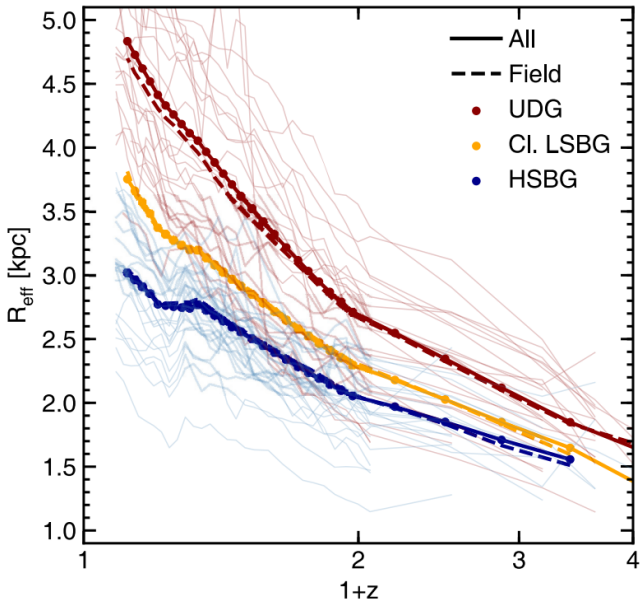

Figure 4.4: The redshift evolution of effective radii in the galaxy sample of Martin et al. (2019). Solid blue, orange, and red-coloured points show the redshift evolution of the median effective radii of the HSBG, LSBG, and UDG populations, respectively. [Credit: Martin et al. (2019)

Looking at the third row of Fig. 4.3, we find a similar divergence at $z \sim 1.5$ for all mass ranges when we examine the evolution of j_*, which in principle could be responsible for the increase of $r_{\rm half}$ for LSBGs. As mentioned before, a smooth transition is observed in the increasing values of j_*, so major mergers may not be the main mechanism responsible for the increase in angular momentum during the formation of LSBGs in our sample. Di Cintio et al. (2019) argued that major merger configurations such as coplanar mergers are capable of increasing the angular momentum of a galaxy. However, these authors also found that, aside from mergers, different phenomena such as the direction of the angular momentum of gas accreted through cosmic time is crucial in determining the final galactic morphology, such that LSBGs are formed out of gas flowing in with similar angular momentum as the already accreted material.

Finally, the fourth row of Fig. 4.3 shows the spin parameter evolution of the parent haloes of LSBGs and HSBGs, in which we observe that both follow a similar behaviour at early epochs ($z \lesssim 2$), and then exhibit a divergence of nearly a factor of 2 in their median values, as previously found by different authors (e.g., Pérez-Montaño & Cervantes Sodi 2019; Kulier et al. 2020; Salinas & Galaz 2021), especially for

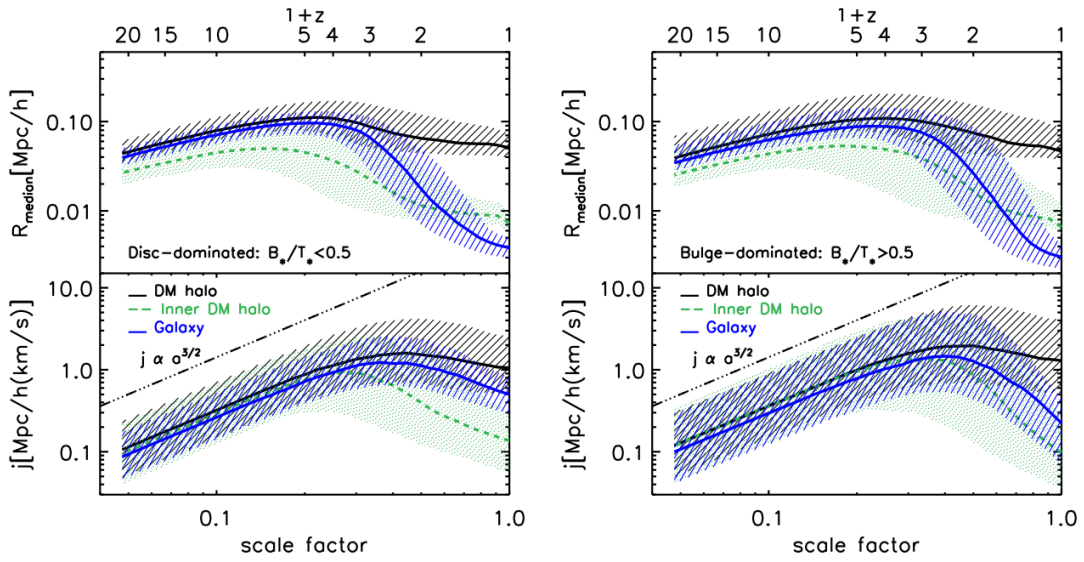

Figure 4.5: Evolution of the median radius (top) and the specific angular momentum (bottom) of three galactic components down to $z = 0$; dark matter halo (black), 'inner' dark matter halo (green) and the whole galaxy (blue). In the bottom panels, the dot–dashed lines show the prediction of specific angular momentum growth according to the linear tidal torque theory before turnaround. It can be observed that at $z \lesssim 2$, the angular momentum of the dark matter halo has no significant evolution after this 'turnaround' epoch, remaining almost constant up to $z = 0$ [Credit: Zavala et al. (2016)].

galaxies in the regime of intermediate and high stellar masses. In the case of the less massive galaxies, the differences in λ become only sligthly noticeable, but still statistically significant, suggesting that other mechanisms might play a more important role, such as supernovae-driven galactic outflows (Di Cintio et al. 2019). Interestingly, we observe that the bifurcation in the values of λ occurs at a slightly earlier redshift than in the case of $r_{\rm half}$ and j_*, at about $z \sim 2$, which suggests that the increase in the spin parameter may have a causal effect on the evolution of other physical properties of the LSBG population, such as their stellar angular momentum and, consequently, their sizes. It is important to point out that the redshift at which this bifurcation occurs happens later than the 'turnaround' epoch, in which the halo evolution is affected mainly by accretion processes and mergers, which are typical in a hierarchical Universe (White 1984; Zavala et al. 2016). After this, the halo spin parameter exhibits very weak evolution. This 'turnaround' is defined as the moment in which protogalaxies gain angular momentum through tidal torques from their environment until maximum expansion, and subsequently collapse into virialized structures that preserve their angular momentum (Doroshkevich 1970; White 1984; Catelan & Theuns 1996a,b). Afterwards, the specific angular momentum is approximately conserved. After turnaround, the specific angular momentum evolution of the different components diverges. While the whole dark matter halo conserves most of its specific angular momentum, the inner dark matter halo, by contrast, loses $\sim$ 90 % of it (Zavala et al. 2016). Bottom panels of Fig. 4.5 shows the evolution of the DM angular momentum in the galaxy sample employed by Zavala et al. (2016) drawn from the EAGLE cosmological simulation, divided between disk-dominated (left) and bulge-dominated (right) galaxies according to their stellar bulge-to disk ratio. Black solid lines correspond to the evolution of the whole DM halo, and indicate that the evolution of the specific angular momentum follows the behaviour predicted by tidal torque theory until turnaround, and then the specific angular momentum remains nearly constant.

4.3 Star Formation Histories

To further understand the origin of the different present-day properties shown by LSBGs and HSBGs, particularly their extended nature, in Fig. 4.6 we show their resolved star formation histories in different radial intervals. Looking at the first row in Fig. 4.6, we did not find any clear difference between the sSFRs of LSBGs and HSBGs all the way down to $z = 0$, as previously pointed out in Section 3.2, except for objects with stellar masses around $M_* \sim 10^{11}\,\mathrm{M}_\odot$. This is qualitatively in a good agreement with what was found by Martin et al. (2019), in which LSBGs and HSBGs share essentially identical star formation histories, as can be seen in Fig. 1.16.

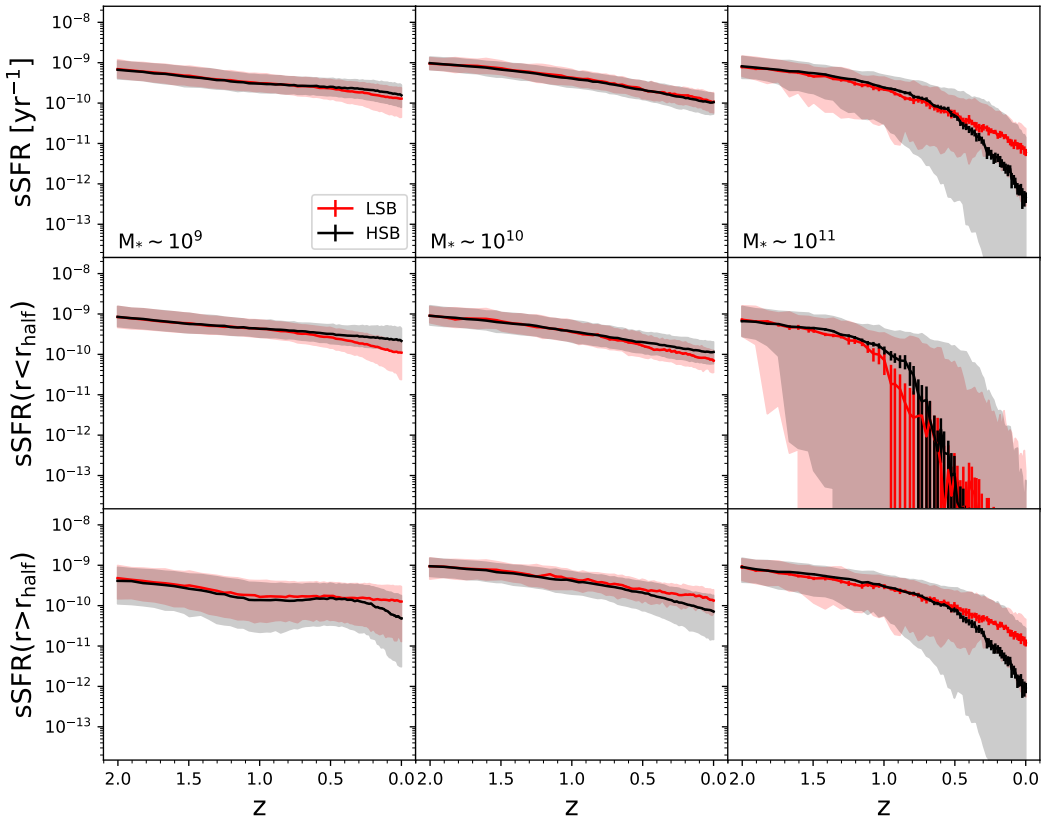

Figure 4.6: Evolution of the total sSFR (top row), the sSFR within one effective radius (middle row), and the sSFR beyond one effective radius (bottom row). The columns from left to right correspond to different stellar mass bins at $z = 0$, corresponding to (0.7-1.4)$\times 10^{9,10,11}$ $\mathrm{M}_\odot$. We do not observe significant differences between the total sSFRs for galaxies with $M_* \approx 10^9$–10^{10} $\mathrm{M}_\odot$, but we do observe that the sSFR tends to be less intense in the inner regions and more active in their outer parts of LSBGs, especially since $z \sim 1.5$, where r_{half} becomes larger for LSBGs, supporting the idea that LSBGs form most of their stars in the outer parts of their disks. [Credit: Pérez-Montaño et al. (2022)]

However, given the more extended spatial distributions of LSBGs, we explore whether differences in the sSFR arise when considering the inner and outer regions of the galaxies in our sample. The middle row of Fig. 4.6 shows the redshift evolution of the sSFR measured within r_{half} (i.e. the "inner" sSFR). This is obtained by the sum of the individual star formation rates of all gas cells in a given subhalo, but only of those within the stellar half mass radius. Similarly, the bottom row shows the sSFR measured beyond r_{half} (i.e. the "outer" sSFR), obtained simply by the difference between the total sSFR and the "inner" sSFR. We observe that, for galaxies with stellar masses between $\sim 10^9$ and $\sim 10^{10}\mathrm{M}_\odot$ (corresponding to the first two columns in Fig. 4.6), the "inner" sSFR (middle row) is less intense for LSBGs than for

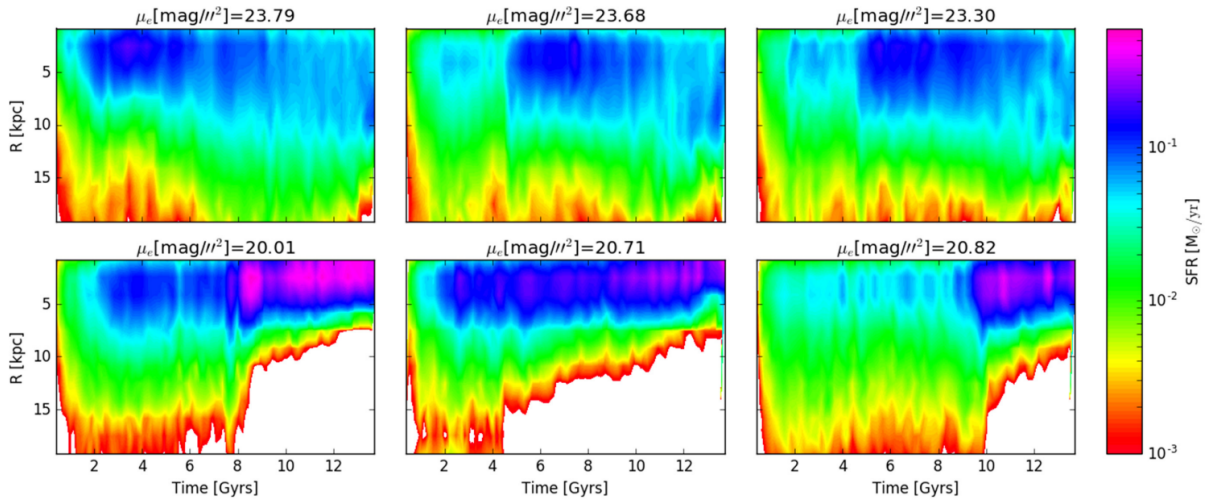

Figure 4.7: Star formation rates of NIHAO galaxies across cosmic time (evolving time) for LSBGs (top row) and HSBGs (bottom row). It can be noted that HSBGs tend to form most of their new stars within the inner 5 kpc, with no young stars found at radii larger than ∼10 kpc, whereas in LSBGs the star formation of younger stars is spread through the whole disk, up to 20 kpc. [Credit: Di Cintio et al. (2019)].

HSBGs at low redshift ($z < 1.5$). The opposite is observed when we look at the "outer" sSFR of the galaxies in our sample, as shown in the bottom row of the same figure, i.e., there is a more intense star formation activity in the outer regions of LSBGs when compared to HSBGs. To complement these results, we repeated the same analysis considering the regions within and beyond two times $r_{\rm half}$, finding a similar behaviour[2]. These results are consistent with those found by observational studies, such as Boissier et al. (2003), in which the star formation histories of LSBGs do not present strong star formation episodes, but remain relatively constant across the cosmic time. Interestingly, this latter result together with ours is in contrast with Pontzen & Governato (2012), where the authors proposed that LSBGs presented high star formation efficiencies at their center in the early stages of their evolution. In Martin et al. (2019), the authors found that LSBGs experience a steady loss of their star-forming gas due to the mechanisms that form LSBGs, such as tidal interactions. In our sample we found that LSBGs have systematically higher amounts of star-forming gas when compared to HSBGs. This could be an indication that tidal interactions are probably injecting this gas to the galaxies, rather than stripping it in the galaxies in our sample, and this would explain why the star formation is more intense in the outer regions of LSBGs.

Similarly, our findings are in good agreement with previous studies employing simulations (e.g., Zhu, et al. 2018; Di Cintio et al. 2019) where LSBGs are able to form through the accretion of high angular momentum material that promotes star formation at large radii. In the galaxy sample of Di Cintio et al. (2019), the authors found that LSBGs have more extended and flat HI gas profiles, with densities of $\Sigma \sim 10$ M$_\odot$ pc^{-2} all the way to radii of 13-15 kpc, while in HSBGs such density is found at 4-5 kpc, producing different signatures in the star formation histories. In Fig. 4.7 the authors present 2D histograms of the radial star formation history as a function of cosmic time (evolving time), where different colors represent different SFRs. It is observed that HSBGs (bottom panels) tend to form most of their new, young stars within the inner 5kpc from their galactic center. LSBGs, by contrast, are able to form new stars through the disk, out to ∼ 20 kpc. Our results also agree with those of Genel et al. (2018), who found that quenched galaxies at the massive end in TNG100 display a slower size growth, similar to our massive HSBG sample. Furthermore, Gupta et al. (2021) found that massive, spatially extended galaxies at $z = 2$ quench later than normal-sized galaxies, which is consistent with our finding that massive LSBGs retain a higher sSFR than HSBGs down to $z = 0$. In Gupta et al. (2021), the authors employed TNG100

[2]Figure not shown

to demonstrate a strong connection between the onset of star formation quenching and the stellar size of galaxies. Fig. 4.8 shows the stellar mass build-up (left-handed panel) and star formation histories (middle and right-handed panels) of the galaxies in their sample, divided between extended (defined as those galaxies with stellar sizes 1σ above the stellar mass-size relation) and 'normal' massive galaxies. It is observed that both, extended and normal galaxies have similar sSFR distributions, up to $z = 2$. Afterwards, it is observed that the star formation in the extended galaxies quench later than in normal-size galaxies.

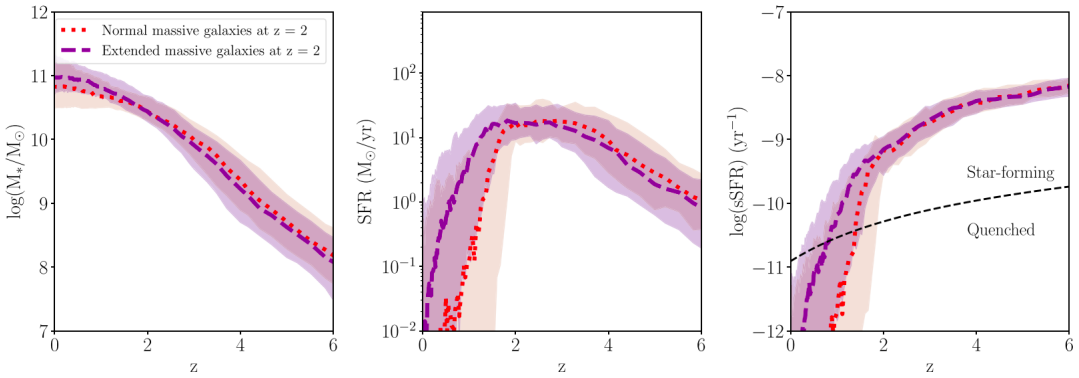

Figure 4.8: Redshift evolution of the stellar mass (left), star formation rate (middle), and specific star formation rate (right) of the extended and normal-sized massive galaxies. We observe that the star formation in extended galaxies (purple) quenches later than in normal-sized (red) galaxies. The cutoff for quenched galaxies is indicated by the dashed black curve adopted from Tacchella et al. (2019). [Credit: Gupta et al. (2021)]

Chapter 5

Environment characterization at different scales

After analyzing the main intrinsic properties of LSBGs at $z = 0$ in our sample, the next natural step is to analyze the impact of the environment on the formation and evolution of these galaxies. The results in Chapters 3 and 4 may suggest that the high angular momentum and stellar mass accretion phenomena rather than mergers are most likely to be the main mechanisms that guide the formation of an extended component, which is responsible for the observed properties such as the large radii that LSBGs present in the current epoch. A detalied analysis of the environment at different scales would allow us to reinforce our hypothesis, revealing clues on which of the mechanisms have the most impact on galaxy evolution in our sample. In this chapter, our objective is to study the environment in which these galaxies reside at $z = 0$, going from small to larger scales. The natural starting point from our study includes the small scales comparable with galaxy groups and their hosting DM halo. Then we move to group scales, allowing us to explore the overdensities around these galaxies, to finally complete our study with the large-scale structures of the Universe, implementing different statistics that allow us to characterize the environment at different scales. Although these statistics most certainly present strong correlations, the variance among them is significant, and their implementation will allow us to construct a complete picture. In the present chapter, we attempt to dig deeper in our study, with the main goal of determining the role that the environment plays in the formation and evolution of LSBGs in our simulated sample.

5.1 Small scales: Dark Matter Halos

In this section we will consider only central galaxies to perform our analysis, given that most of the properties studied here are well-defined only for central galaxies. We remind the reader that central galaxies are defined in our sample as the most massive galaxy of a given FoF group, as mentioned in sec. 2.2.2. In Chapters 3 and 4, we found that LSBGs are formed within halos of marginally smaller stellar-to-halo mass ratio, but higher spin parameter than HSBGs, as seen in Figs. 3.12 and 3.9. We replot these median values in the upper and middle panels of the first column in Fig. 5.1, which shows the median values of M_*/M_{200} and λ as a function of M_*. As in previous sections, the red and black lines correspond to the median values found for LSBGs and HSBGs, respectively, and the shaded area encloses the region delimited by the 16th and 84th percentiles of the given distributions. Again, the error bars represent the statistical significance of the median, and are obtained by performing a Bootstrap re-sampling, with 1000 random realizations derived from the original samples. In this figure, we have extended our previous analysis by separating our galaxies by morphology, according to their $\kappa_{\rm rot}$ values, following the criteria mentioned in Chapter 2, i.e., we consider as spiral (elliptical) galaxies those with $\kappa_{\rm rot}$ larger (smaller) than 0.5. We can visualize this segregation in the 2nd and 3rd columns of Fig. 5.1. It can be observed that despite their morphology, we find similar trends when compared with the full sample, i.e., LSBGs have slightly smaller stellar-to-halo mass ratios and higher spin parameter than their

HSBGs counterparts. These differences are not surprising in the case of spiral galaxies, due to the fact that many observational studies of LSBGs found that LSBGs are mainly disk-dominated systems, and therefore the study of their angular momentum and spin parameter indicates that LSBGs are galaxies with high angular momentum (McGaugh, Bothun & Schombert 1995; Zhong et al. 2008; Galaz et al. 2011; Pérez-Montaño & Cervantes Sodi 2019; Salinas & Galaz 2021). The interesting fact is that, in our sample, even elliptical galaxies are found to have higher values of their spin parameter when compared to HSBGs, reinforcing our previous hypothesis.

We now extend our study towards further properties of the DM halos in which LSBGs reside, such as their halo concentration index, the triaxiality of halos and the alignment between the stellar and dark components of the angular momentum. We present a detailed analysis of these properties in the following subsections.

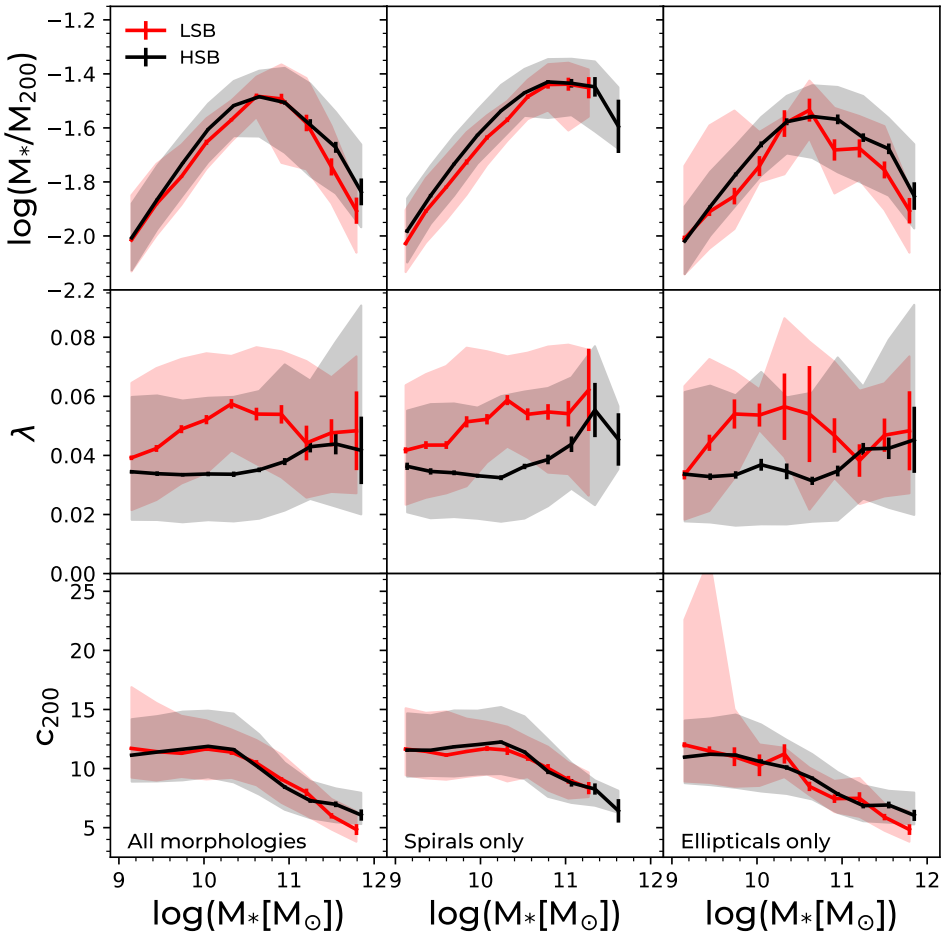

Figure 5.1: The median values of main halo properties hosting central LSBGs and HSBGs, namely the stellar-to halo mass fraction (top row), the spin parameter (middle row) and halo concentration index (bottom row). At fixed stellar mass, the main differences between both galaxy populations are found in λ, regardless of their morphology, suggesting that the formation of LSBGs is more likely to be caused by variations in the angular momentum of the halos, rather than variations in their density, characterized by c_{200}, as one of the mechanisms highlighted by McGaugh (2021). [Credit: Pérez-Montaño et al. (in prep.)]

5.1.1 Halo concentration index

In a recent review by McGaugh (2021), the author points out that the variations in the size of the galaxies, and consequently the formation of LSBGs, could have one of two causes: variations in the spin parameter of the halo, or variations in the density of the DM halos. We have shown in the middle panel of Fig. 5.1 that there is a significant difference in the median values of the spin parameter λ, which may suggest that the first mechanism highlighted by McGaugh (2021), the variations in the spin parameter, is the one that induces the formation of LSBGs in our sample. However, it is not possible to affirm that this is "the main" mechanism without studying the second scenario proposed by McGaugh (2021). To do so, in the lower panel of Fig. 5.1 we plot the median values of the halo concentration index c_{200} of our synthetic sample. This concentration index in our sample is computed as

$$c_{200} = \frac{R_{200}}{R_s}, \tag{5.1}$$

where R_{200} is the radius in which the enclosed average density is 200 times the critical density of the Universe, and R_s is computed by fitting a Navarro-Frenk-White (Navarro, Frenk, & White 1996) profile to the DM density profile. This data is obtained from the post-processed data catalogs from Anbajagane, Evrard, & Farahi (2022). We observe no significant differences in the median values between LSBGs and HSBGs, even if we segregate our galaxies by morphology. Therefore, we can conclude that for the galaxies in our sample, the differences between LSBGs and HSBGs are due to the variations in the spin parameter. This is consistent with our previous findings presented in Chapter 4, in which we tracked back the evolution of the spin parameter of the galaxies in our sample, finding a cause-consequence relation between the variations of λ and the variation of other properties, such as the size of our galaxies. Interestingly, our findings seem to be in contrast with Kulier et al. (2020). These authors found that LSBGs tend to inhabit slightly more concentrated halos than HSBGs, but this trend seems to be reversed or non-existent if their sample is divided by their mean surface brightness (see the lower right-hand panel of Fig. 1.18). The authors found that this is probably due to the fact that, for galaxies in EAGLE, the concentration index is strongly correlated with the mean stellar age of the central galaxy and its star formation rate (Matthee et al. 2017; Matthee & Schaye 2019). Given that in Kulier et al. (2020) the central galaxies of halos with larger concentrations are older, it is expected to find LSBGs residing in halos with high concentration index. In our case, as shown in Chapter 3, there is no significant difference in the stellar ages of central galaxies between LSBGs and HSBGs, so it would be natural to find no differences in the concentration indices of halos in TNG100.

5.1.2 Halo Geometry

The halo geometry is a very important property to study, given that it could provide interesting clues about different processes in the formation and evolution of galaxies. Let a, b and c be the axes sizes of a dark matter halo. Depending on the ratio between them, the halos can be classified as *prolates* ($a > b = c$), *oblates* ($a = b > c$), *triaxials* ($a > b > c$) and *spherical* ($a = b = c$). Fig. 5.2 provides an illustrative example of the characteristic shapes of these dark matter halos. Taking this into account, we continue the study of the dark matter halo configuration by analyzing the geometry of the halos in which LSBGs and HSBGs reside. Fig. 5.3 shows the intermediate-to-major axis ratio $q = b/a$ and the minor-to-major axis ratio $s = c/a$ of the dark matter halos, which are taken from the supplementary catalog of Anbajagane, Evrard, & Farahi (2022). In this catalog, the components a, b and c correspond to the eigenvalues of the quadruple tensor of the particle positions, and satisfy that $a > b > c$. Dotted lines delimit the regions in which the halos are classified as tri-axial, prolate, oblate and spherical, according to Li et al. (2018). The density contours show that most of the galaxies in our sample (around 91% of them) present values of q and s closer to 1, implying that most of the galaxies reside within nearly-spherical halos, regardless of their morphology. By contrast, 6% of the galaxies in our sample reside within halos with oblate geometry, while 3% live within prolate halos. Only 4 galaxies in our sample are found in triaxial halos.

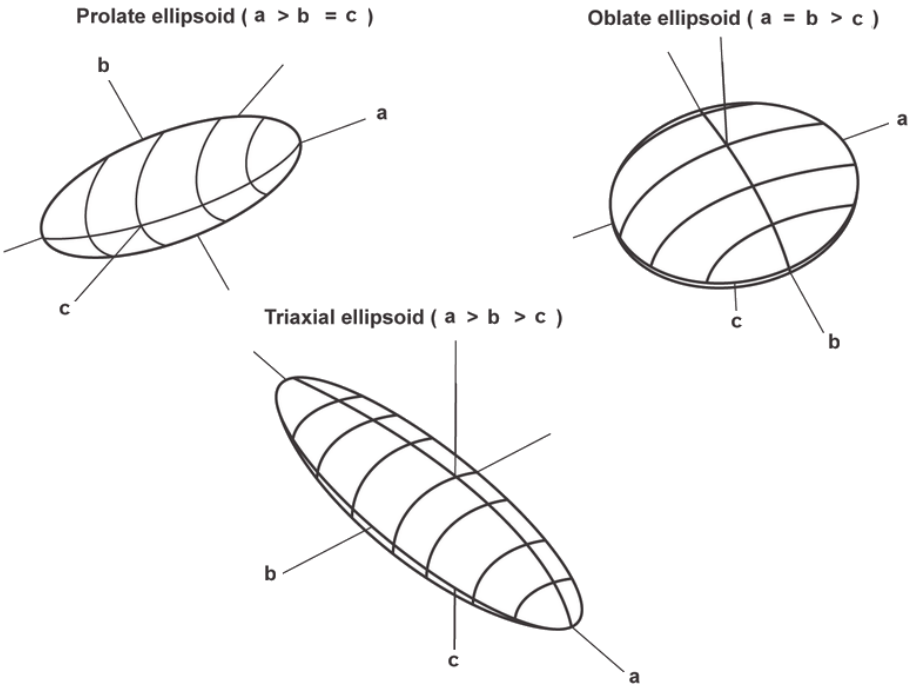

Figure 5.2: Illustrative example of the shape of the dark matter halos, according to their axis ratios. [Credit: Downloaded from https://www.researchgate.net/figure/Schematic-depiction-of-prolate-oblate-and-triaxial-magnetic-susceptibility-ellipsoids_fig2_232815665, edited by Luis Enrique Pérez Montaño.]

Together with the density contours, in Fig. 5.3 we also plot the distributions of q and s along the corresponding axes, segregated by LSBGs and HSBGs. Within them we observe a small but statistically significant difference in the distributions of q and s, in which both axis ratios in LSBGs are closer to 1 than in HSBGs. The p-values < 0.01 obtained from a Kolmogorov-Smirnov (KS) test performed over LSBGs and HSBGs distributions allow us to reject the null hypothesis that these were extracted from the same population.

It is well known that there is a strong correlation between the geometry of the halos and the stellar mass of the galaxies that reside within them. In order to exclude any mass-dependence on the resulting trends, we construct three different sets of control samples as follows: for a given LSBG, we look for an HSBG counterpart controlling only by stellar mass, such that $\Delta \log M_* < 0.05$ between them. We built three different pairs of control samples for this purpose: one for all central galaxies in our sample, regardless of their morphology (referred as 'CS1'), and two more pairs of control samples segregated into spiral ('CS2') and elliptical galaxies ('CS3'). By construction, the number of LSBGs and HSBGs in each pair of control samples is the same. Once again, a KS-test was performed in each pair of control samples to accept the hypothesis that the galaxies are drawn from the same distribution. Table 5.1 summarizes the number of galaxies in each pair of control samples, as well as the corresponding $p-$value obtained after performing the KS-test. The results obtained for the geometry of the halos of the galaxies in each pair of control samples are very similar to the ones obtained for the full sample (without controlling the stellar mass) at the top panel of Fig. 5.3, that is, most of the galaxies reside within quasi-spherical DM haloes, with LSBGs showing q and s values closer to 1 than HSBGs. The lower panels of Fig. 5.3 follow the same format as in the top panels, but considering only the three pairs of control samples (CS1, CS2 and CS3).

In Li et al. (2018), the authors employed a sample of galaxies drawn from the 'original' Illustris suite,

Morphology Name	All morphologies CS1	Spirals CS2	Ellipticals CS3
Number of paired galaxies	3,172	2,069	762
p-value	0.998	0.8342	0.971

Table 5.1: Number of galaxies and the corresponding p-values of the resulting KS test performed in each pair of control samples (LSBGs and HSBGs). By construction each LSBG has associated a HSBG counterpart of similar stellar mass $\Delta \log M_* < 0.05$), implying that the number of LSBGs and HSBGs in each pair of control sample is the same. We remind the reader that only central galaxies are included in this analysis.

finding that most massive galaxies ($M_* > 10^{11}\mathrm{M}_\odot$) are preferentially found within prolate halos. In our sample, by contrast, most of the galaxies are found preferentially in halos with spherical geometry. This could be explained by the stellar mass range we consider in our sample, as was mentioned in Chapter 2. The galaxies in our sample have $10^9 < M_* < 10^{12}\mathrm{M}_\odot$, not including the most massive systems. The interesting fact is that Li et al. (2018) found that most of the galaxies living within prolate halos have experienced major 'dry' mergers in the past. The absence of galaxies living in prolate halos could be an indication that most of the galaxies in our sample, particularly those corresponding to LSBGs, have not experienced these 'dry' mergers. This argument, together with the fact that LSBGs are mostly gas-rich systems (as showed in Chapter 3), reinforces the hypothesis that the formation of an extended component around galaxies could be mainly due to the accretion of material coming from another gas-rich galaxy, in line with previous studies (Zhu, et al. 2018; Di Cintio et al. 2019, Zhu et al. submitted). This result could also arise if the galaxy has been fed through filaments in a configuration such that the accreted gas has an angular momentum vector parallel to the one of the galaxy, in order to form a gas disk that could eventually form stars, leading to the formation of the extended structure characteristic of LSBGs. Similarly, Athanassoula, Machado, & Rodionov (2013) found that the halo geometry has a strong impact over the baryonic component of the galaxies, particularly, they found that less spherical halos favour the early formation of stellar bars. This result is in agreement with the results of Fig. 5.3, in which the departure from spherical halos in HSBGs will explain the absence of stellar bars in our sample of LSBGs (Chim et al. in prep.)

5.1.3 Angular Momentum Alignment

We continue our previous analysis of the DM halos of LSBGs discussed in Chapter 3 by turning our attention to the alignment of the angular momentum vectors of both, stellar and dark matter components. Different studies employing numerical simulations have shown previously the existence of an alignment between stellar and dark matter angular momentum vectors (e.g. Bailin et al. 2005; Bett et al. 2010; Velliscig et al. 2015). With this premise, it is important to explore in deital the alignment of the angular momentum vectors between the stellar and dark matter components, due to the fact that the existence of this alignment could provide some interesting clues towards the understanding of the galaxy/halo evolution, as well as the processes involved in it, as mentioned in Chapters 3 and 4. The existence of such an alignment is the result of a natural combination of two phenomena: the common origin and co-evolution of the protogalaxy and its corresponding protohalo, and the dynamical response of the halos to the assembly of the baryonic disk.

In Chapter 2, we pointed out that eq. 2.1 is employed to compute the specific angular momentum of the stellar component of the galaxies in our sample, which allowed us to obtain not only the magnitude of j_*, but also its direction. In order to compute the angular momentum of the dark matter component, we employ a modified version of eq. 2.1, namely

$$\vec{j_{200}} = \frac{\vec{J_{200}}}{M_{200}} = \frac{\sum_i m_i \vec{r_i} \times \vec{v_i}}{\sum_i m_i}. \tag{5.2}$$

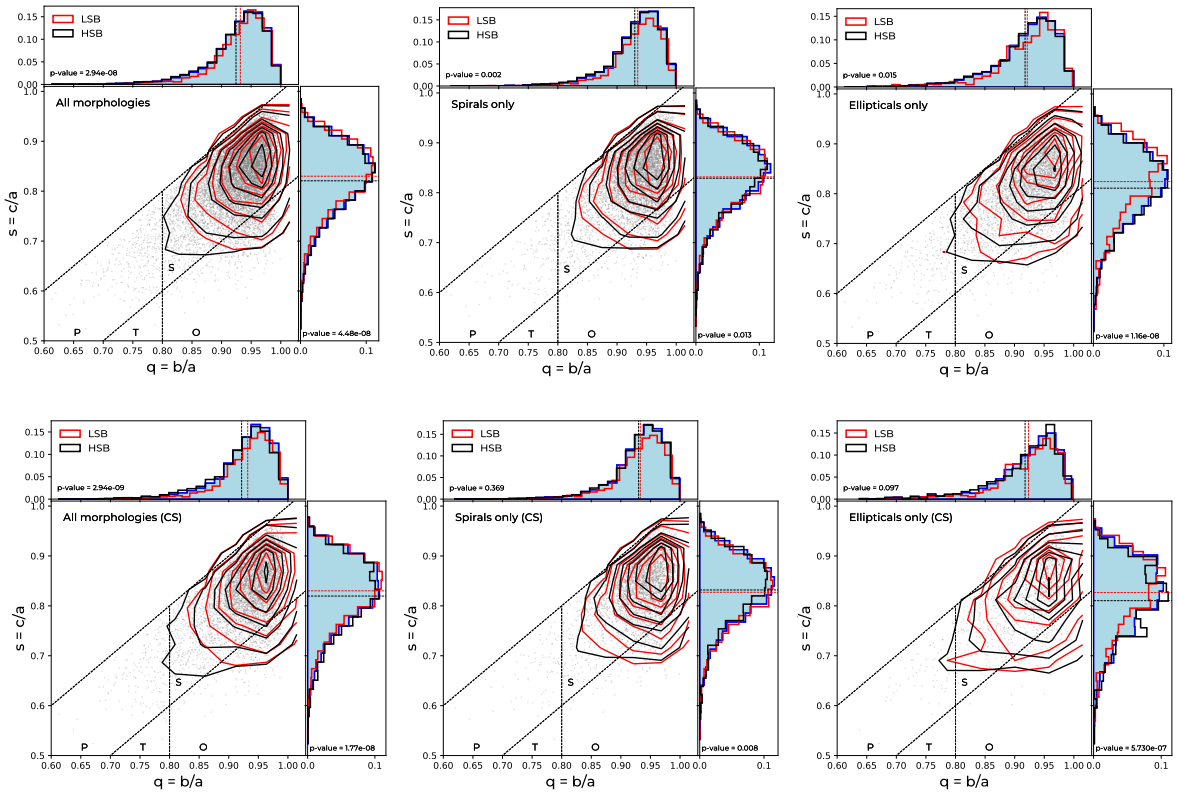

Figure 5.3: *Top row:* The axis ratios of the DM halos for all galaxies in the sample (left), spirals (medium) and ellipticals (right). Dotted lines enclose the regions where the halo shapes are considered as prolate (P), tri-axial (T), oblate (O) and spherical (S). *Bottom row:* Same as above, but for each pair of control samples (CS1, CS2 and CS3, respectively). From this figure, we observe that not only LSBGs, but also HSBGs, are found in nearly spherical halos. The departure from spherical halos in HSBGs is larger than in the case of LSBGs. [Credit: Pérez-Montaño et al. (in prep.)]

This equation provides the main halo's angular momentum $\vec{j}_{200}$ by considering, not the stars, but the DM particles within R_{200}. As in the case of the stellar component, each dark matter particle of the configuration has associated to it a position and a velocity vector, but in this case, the mass of each dark matter particle is the same for all considered in our calculation, with a given value of $7.5 \times 10^6 M_\odot$. Once we implement eq. 5.2, we obtain both, the magnitude and the direction of, j_{200}. Finally, we compute the alignment of both components by simply using the dot product between $\vec{j}_*$ and $\vec{j}_{DM}$

$$cos(\theta_{*,\mathrm{DM}}) = \frac{\vec{j}_* \cdot \vec{j}_{200}}{\|\vec{j}_*\| \|\vec{j}_{200}\|}, \tag{5.3}$$

where θ is the angle between $\vec{j}_*$ and $\vec{j}_{200}$. To visualize the alignment between the two components, Fig. 5.4 shows the median values of $\theta_{*,\mathrm{DM}}$ as a function of the stellar mass, considering the full sample of central galaxies (left-hand panel). The dashed line highlights the 45° angle between the angular momentum vectors of both components. From this figure, we can observe that the median values of $\theta_{*,\mathrm{DM}}$ are systematically lower for LSBGs than in the case of HSBGs, implying that both components are more strongly aligned than for HSBGs. To complement this study, we can also observe that this trend is similar even if we divide our sample into spiral and elliptical galaxies. Interestingly, from the three panels, we observe that the median values of $\theta_{*,\mathrm{DM}}$ are found mostly under 45°, with the corresponding distributions $\theta_{*,\mathrm{DM}}$ in LSBGs being narrower, and presenting median values smaller than the case of HSBGs. This trend allows us to conclude that the stellar angular momentum vector in LSBGs is more

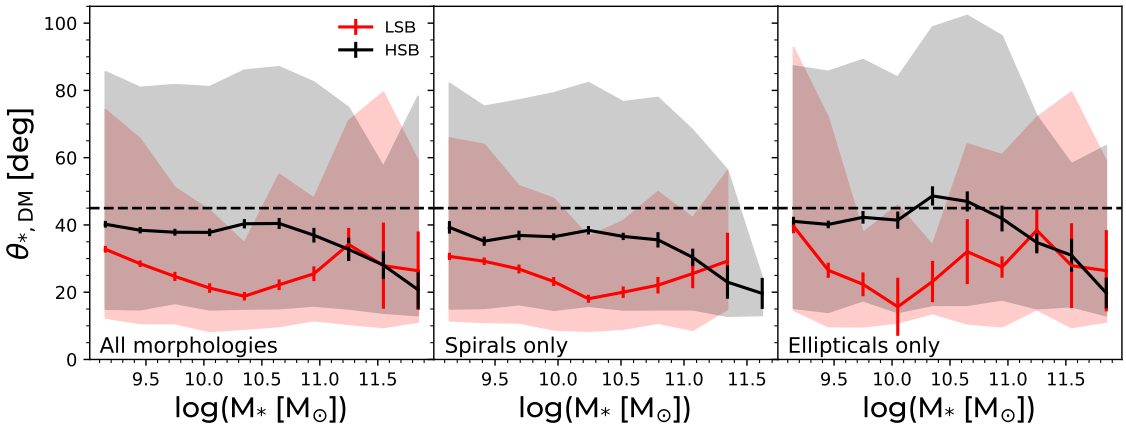

Figure 5.4: The alignment between stellar and halo angular momenta, represented by the angle between both angular momentum vectors. The distributions of $\theta_{*,\mathrm{DM}}$ are found to be narrower than the ones obtained for HSBGs, with median values closer to zero, indicating a stronger alignment between components in LSBGs than in HSBGs. This stronger alignment between both components in LSBGs is reminiscent of the angular momentum conservation j/j_{200} shown in Fig. 3.9 (see Chapter 3) [Credit: Pérez-Montaño et al. (in prep.)]

aligned with the dark matter component than for the case of HSBGs. This result reinforces our hypothesis on the impact of the stellar angular momentum in galaxy evolution. Aligned components will favor a scenario in which the total angular momentum is highly conserved, while a misalignment will imply that most of the total specific angular momentum will be 'lost' due to the angular momentum components pointing in different directions. The alignment between both components will cause both vectors to be added in the same direction, implying that there is no cancellation of angular momentum when they are added vectorially. The angular momentum alignment has been found to be important in the formation mechanisms of LSBGs, as highlighted by Di Cintio et al. (2019). These authors found that, aside from mergers, the alignment of the angular momentum of accreting gas through cosmic time is crucial in determining the final galactic morphology, such that LSBGs are formed out of gas flowing in with similar angular momentum as the already accreted material (Zhu et al., submitted). This demonstrates that the alignment between baryonic angular momentum that is infalling into the protogalaxy is an important factor in creating LSBGs. With respect to the alignment of the stellar and dark components, Bullock, et al. (2001) showed that halos with a misaligned angular momentum distribution may be less likely to host extended galaxies, such as the case of HSBGs in our sample, which have been shown to be less extended than LSBGs as previously mentioned in Chapter 3.

5.2 LSBGs within groups.

We scale up our analysis to the next level, more specifically, focusing our interest in the analysis of the environment around LSBGs at the scale of groups and clusters. This is important given that, as mentioned in Chapter 1, many previous works have studied the environment of LSBGs at this level, in order to quantify, for example, how isolated these galaxies are. We recall the work performed by Rosenbaum et al. (2009), who found that for galaxies between $z = 0.01 - 0.1$, the average number of neighbours within a sphere of a given radius is systematically lower in LSBGs than in HSBGs, as seen in Fig. 1.13. Similarly Galaz et al. (2011) found that LSBGs tend to lack neighbouring galaxies within a sphere of ~ 0.5 Mpc. Finally in Pérez-Montaño & Cervantes Sodi (2019), we found that around $\sim 70\%$

of LSBGs in a volume-limited sample are isolated galaxies, while about 60% of HSBGs are isolated[1].

In extragalactic astronomy, several studies have been focused in the properties of the galaxies residing in groups, and how the interactions between them affect their observed properties, such as morphology (Tempel et al. 2011; Pearson et al. 2021), star formation rates (Balogh et al. 1998; Raichoor & Andreon 2012; Barsanti et al. 2018)[2], or even nuclear activity (Marshall et al. 2018; Mishra & Dai 2020; Eckert et al. 2021). According to simple theoretical considerations, the number of galaxies in a given group/cluster is expected to increase towards the center. However, such arguments typically neglect dynamical processes within group or cluster environments, such as tidal stripping and galaxy harassment, which are modeled self-consistently in cosmological simulations. Taking this into account, in order to study the impact of the groups in which LSBGs reside on their their observed properties, we quantify the fraction of satellite LSBGs as a function of the distance r to the center of its corresponding host group. In our study, we consider the 'center' as the spatial coordinates of the most gravitationally bounded particle of the central galaxy in a given group. For each group, we first identify the central galaxy, corresponding to the most massive within it, and then for the rest of the satellite galaxies, we calculate the 3D distance to the central one. Given the wide distribution of halo sizes in our sample, to obtain a better understanding of our results, we will focus on the "relative" distance to the center of a given group. To do so, we normalize the obtained distance by the characteristic "group size" R_{200}, defined as the radius containing 200 times the critical density. We perform this experiment for every group in our sample (i.e., with at least two galaxies), and finally obtain the net fraction of LSBGs within different r/R_{200} bins.

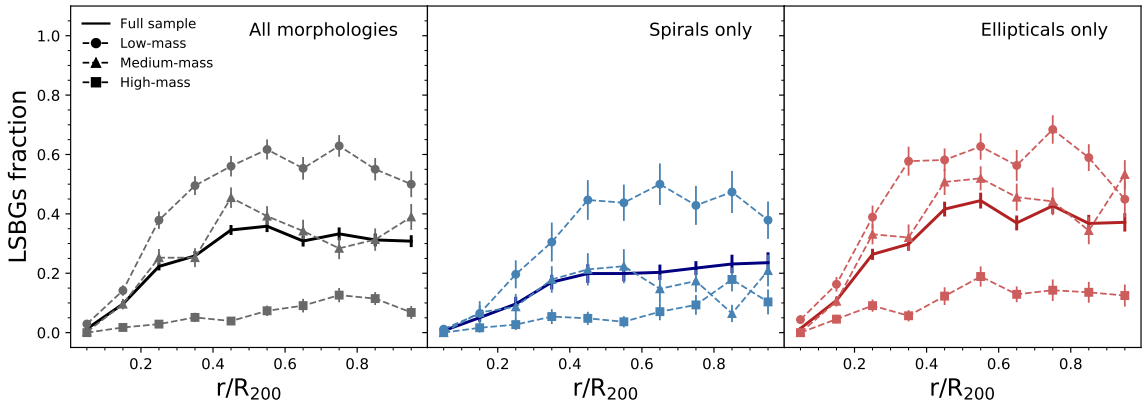

Figure 5.5: The fraction of LSBGs as function of the normalized distance to the center of their corresponding group r/R_{200}, segregated by morphology within three different mass intervals. In general terms, we observe that the fraction of LSBGs increases as we move away from the center of galaxy groups. At $r/R_{200} > 0.4$, the fraction of spiral LSBGs is nearly half of the fraction of elliptical ones, suggesting that close interactions may have transformed them into ellipticals and implying that spiral and elliptical LSBGs may have followed different formation mechanisms. [Credit: Pérez-Montaño et al. (in prep.)]

The result of this exercise is presented in Fig. 5.5, in which we plot the net LSBGs fractions against the normalized distance r/R_{200}, including galaxies of all morphologies (left-hand panel), spirals (middle panel) and ellipticals (right-hand panel). Different line-styles indicate different mass ranges, whereas solid lines include all the galaxies considered in the corresponding analysis. The segregation of the galaxies in our sample by stellar mass is done by ranking all the satellite galaxies by M_* and dividing the full distribution in three sub-samples, such that every sub-sample contains the same number of galaxies, but each group has different median values of M_* (named 'low', 'medium', and 'high'). We choose this procedure rather than imposing lower and upper limits of stellar mass in every sub-sample because, as

[1] In Pérez-Montaño & Cervantes Sodi (2019), galaxy groups were identified from the Yang et al. (2007) groups catalog, in which "isolated" galaxies are those with no assigned neighbours, according to Yang et al. (2005) method.
[2] Despite other studies find the opposite, e.g. Laganá & Ulmer 2018; Contini et al. 2019

mentioned in Chapter 2, the number of LSBGs at stellar masses larger than $M_* = 10^{11.5}\mathrm{M}_\odot$ in our simulated sample is quite small, biasing the interpretation of our results at those stellar mass ranges.

In general terms, the three panels exhibit a similar behaviour: the fraction of LSBGs increases with r/R_{200}, confirming that LSBGs tend to reside in low-density environments, such as the outer part of groups and large clusters. From the solid line in the left-hand panel of Fig. 5.5 when no morphological segregation is done, we note that most of the satellite LSBG population are not in the center of galaxy cluters, but they are found in the outer regions of such clusters. This indicates that LSBGs are either not formed in the center of galaxy clusters, or they are destroyed once they reach the central regions. When we observe the sample segregated by stellar mass (dotted-lines), we note that the fraction of LSBGs is larger for low-mass galaxies (circles) than in the case of high-mass galaxies (squares), as previously found in Chapter 2. If we focus on the low-to-intermediate mass galaxies, we clearly see that the fraction of LSBGs depends on the distance to the center of the galaxy cluster, as there is an absence of LSBGs close to the center. For the case of high-mass galaxies, such dependency is not observed. This suggests that these galaxies are massive enough to "survive" violent events. However, when we segregate our sample between spiral and elliptical galaxies, the fraction of spiral LSBGs decreases faster than in the case of ellipticals, suggesting that LSBGs at the center of galaxy clusters are more likely to be early-type galaxies. We note that the fraction of spiral LSBGs is nearly constant at 20% for $r/R_{200} > 0.4$, while the fraction of elliptical LSBGs is almost twice the fraction of spirals. Moreover, the fraction of LSBGs of intermediate masses is larger for elliptical galaxies than spiral ones. This result could be not only an indication that the formation of LSBGs depends strongly on the distance to the center of a given group and on morphology. The absence of spiral LSBGs with intermediate masses may suggest that these galaxies could be subject to interactions, resulting in the excess of satellite elliptical LSBGs we observe in our sample. This may be an indicative of different formation scenarios of LSBGs: spiral LSBGs may form by secular evolution, while elliptical LSBGs may form by different mechanisms of galaxy interactions such as mergers, even when both galaxy populations reside away from the center of their corresponding groups.

This scenario seems to be in line with what is reported by Kulier et al. (2020), where the authors point out that LSBGs are further away from their closest neighbour than HSBGs, implying that the former are generally more isolated not because they formed in low-density environments, but due to the destruction of their closest neighbors. This eventually leds to the formation of the extended disks found in LSBGs. In the top panel of Fig. 5.6, solid lines show the median nearest-neighbor distances of LSBGs (blue) and HSBGs (red) from Kulier et al. (2020), in which neighbours are defined as any galaxy with $M_* > 10^9\mathrm{M}_\odot$. When all the galaxies are considered, we observe that LSBGs tend to be farther from their nearest neighbour galaxy than HSBGs. By contrast, for central galaxies (second panel) it is observed that LSBGs and HSBGs have similar distributions of nearest neighbours, whereas for satellite galaxies (third panel), HSBGs tend to be closer to their nearest neighbour, and the difference is more pronounced in the bottom quartile (indicated by dashed lines) than in the top quartile, suggesting that neighbour galaxies of LSBGs are less likely to be very close to them. Finally, in the bottom panel of Fig. 5.6 dashed lines show the fraction of LSBGs and HSBGs that are satellite galaxies, as a function of stellar mass. From this panel we observe that a large fraction of HSBGs are satellite galaxies (which is consistent with the results found in Fig. 5.5, where the fraction of satellite LSBGs is less than 40%). However, considering satellite galaxies with an 'infall' time larger than 8 Gyrs (dash-dotted lines), reminding that the infall time was defined in section 3.4 as the time in which a satellite galaxy crosses the virial radius of its current host for the last time, the fraction of LSBGs and HSBGs is quite similar, implying that HSBGs are probably satellites that were accreted in the past. Thefore, combining the information of the four panels, the authors conclude that LSBGs and HSBGs do not form in very different environments, but the encounters with other massive galaxies tend to disrupt LSBGs. It is important to note that this hypothesis is only related to the formation of satellite LSBGs. An extended analysis of the impact of the environment on the formation and evolution of LSBGs considering both central and satellite galaxies will be discussed in the following sections.

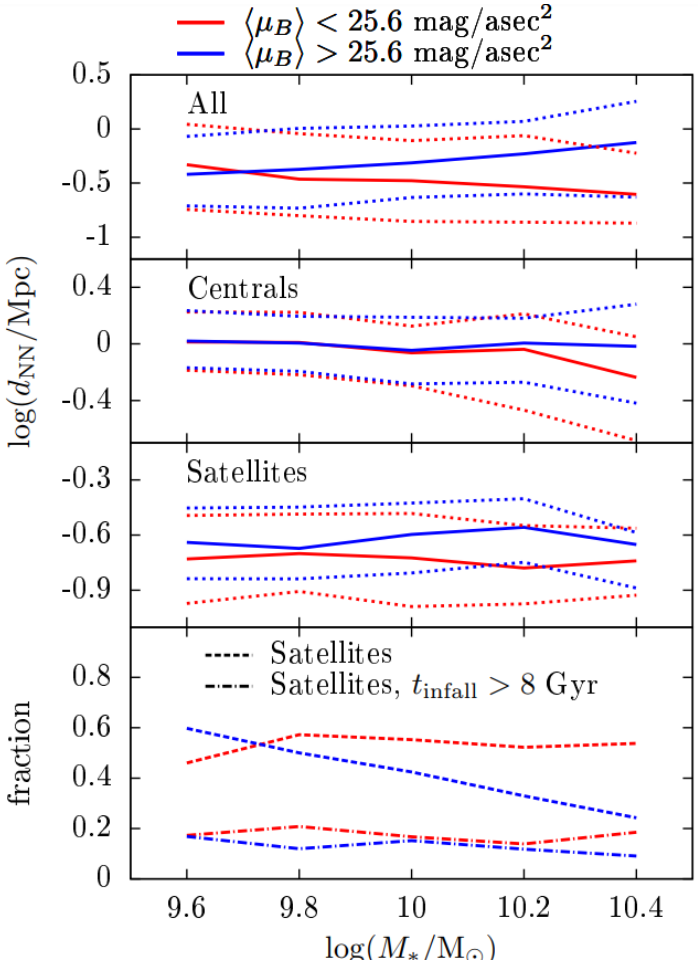

Figure 5.6: Median (solid lines) and quartiles (dashed lines) of the distribution of nearest neighbour distances d_{NN} for LSBGs (blue) and HSBGs (red) in EAGLE. First, second and third panel correspond to all galaxy population, centrals and satellites, respectively. The bottom panel shows the fraction of LSBGs and HSBGs that are satellites in each stellar mass bin. Doted-dash lines show the same, but for satellite galaxies that fell into their host halo after 8 Gyrs. [Credit: Kulier et al. (2020)]

5.3 Local overdensity

The results presented in the previous section allowed us to have a first approach to how companion galaxies have an impact on LSBG population, particularly the fraction of LSBGs within large galaxy groups/clusters. However, this characterization is limited to satellite galaxies only. In order to study the influence of galaxy companions on central ones, in Fig. 5.7 we show the $\ln(2+\delta) - M_*$ plane for the galaxies in our sample, divided by central (upper panels) and satellite (lower panels) galaxies. Colored lines represent different iso-contours of constant LSB fraction $f_{\rm LSB}$, defined as the number of LSBGs within each square bin in the plane, divided by the total number of galaxies in such a bin. Once again, contours are obtained by dividing the parameter space into 10×10 bins, applying a spline kernel to obtain a smooth transition. A minimum of fifteen galaxies per bin is required to estimate the LSBGs fraction. The density field δ calculation is based on the 5th nearest neighbour of a given galaxy, considering only those with an r-band absolute magnitude < -19.5 (Vogelsberger et al. 2014). From Fig. 5.7 we observe that the location of satellite galaxies in the $ln(2+\delta) - M_*$ plane extends to larger densities when compared to central galaxies.

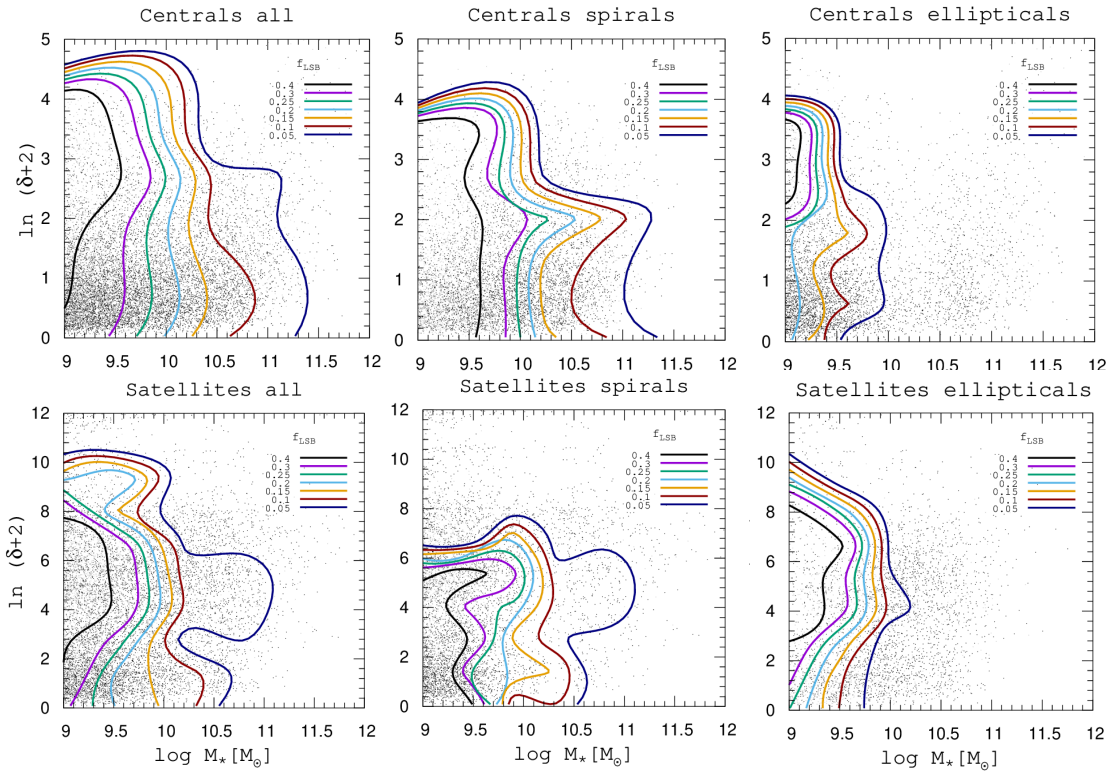

Figure 5.7: *Top row:* Iso-contours of constant LSBGs fraction $f_{\rm LSB}$ in the $\ln(2+\delta) - M_*$ plane for central galaxies in our sample, segregated by morphology. The fraction of central spiral LSBGs does not depend on the density/environment, which could be considered as an indication of secular evolution. By contrast, for central ellipticals, the fraction of LSBGs grows with density. Given that galaxies in high-density environments have many interactions, this could indicate that elliptical LSBGs are formed mainly due to mergers and flybys. *Bottom row:* Same as the top row, but for satellite galaxies. In this case, satellite spiral LSBGs populate the low-density regime, reflecting their isolated nature. The fewer interactions these galaxies experience, the higher the probability of evolving as LSBGs. On the other hand, for satellite elliptical galaxies the LSBGs fraction is maximum at intermediate densities, highlighting the importance of galaxy interactions in their formation. [Credit: Pérez-Montaño et al. (in prep.)]

We also observe from this figure that the fraction of central LSBGs does not exhibit a strong dependency with the environment. At fixed stellar mass, the values of $f_{\rm LSB}$ remain nearly constant when the density increases. This result suggests that central LSBGs are probably formed in low-density environments, evolving as LSBGs due to secular processes and accretion of material from close companions. On the other hand, for satellite galaxies, at fixed stellar mass we observe that these galaxies tend to inhabit environments of intermediate density. When we segregate satellite galaxies between spirals and ellipticals, we do find a difference: spiral galaxies are found in low-density environments while ellipticals are found in medium/high densities. This indicates that the formation of satellite spiral LSBGs is favoured in low density environments with minor interactions, which allow them to "survive" as LSBGs. In contrast, for elliptical satellite LSBGs, their abundance is increased at intermediate densities, highlighting the importance of galaxy interactions in their formation.

Interestingly, this result seems to be in line with previous studies focused on the main mechanisms that favor the formation of the so-called *Ultra-Diffuse Galaxies* (UDGs) in low/high density environments (Amorisco & Loeb 2016; Sales et al. 2020; Benavides et al. 2021; Marleau et al. 2021; Jones et al.

2021). The main conclusion drawn from these works is the existence of two sub-populations of UDGs: the ones that are formed in the field, and the ones formed within large galaxy clusters. Another interesting conclusion is about the different mechanisms that may form them. The morphological properties of observed UDGs seem not to be compatible with spiral galaxies, due to the transition from disks to spheroids caused by interactions with the cluster via ram pressure stripping and tidal interactions (Koda et al. 2015), which could explain the lower number of spiral LSBGs found in groups observed in Fig. 5.5. Sales et al. (2020) argued that the tidal stripping of the stellar components could drastically reduce their stellar mass, with their sizes remaining constant as shown in Fig. 5.8, implying that galaxies that experience strong tidal stripping could be transformed into galaxies with lower surface brightness than expected. The origin of cluster UDGs has two main mechanisms: first, UDGs are just "normal" LSBGs that have entered into a galaxy cluster (*born* UDGs). Second, UDGs that were formed gradually due to their excessive loss of stellar mass through tidal interactions (*tidal* UDGs). It is not unreasonable to argue that these mentioned mechanisms can also explain the formation of LSBGs in the galaxy groups of our sample due to their large variety of sizes and morphologies (as seen in secs. 2 and 3). Moreover, in our work we have excluded the UDG population due to resolution effects at the low-mass end of TNG100, but this could be taken as an indication that some "classical" LSBGs found are evolving in that direction, being transformed to UDGs. This last conclusion is not surprising, given that Sales et al. (2020) employ a sample of galaxies drawn from TNG100, as in our case.

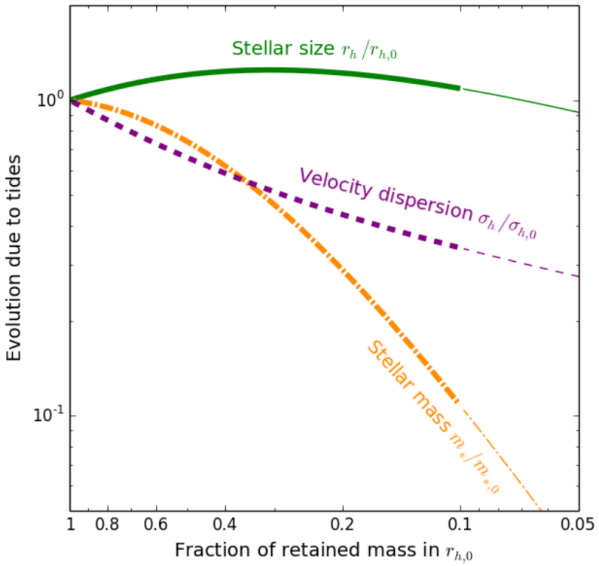

Figure 5.8: The evolution of stellar mass (orange), the half-mass radius (green), and stellar velocity dispersion (purple) for a selected galaxy undergoing tidal disruption. We observe from this figure the main effect of tidal stripping on the stellar component, gradually reducing its stellar mass while keeping its size approximately constant. This is an indication that strong stripping could lead to the formation of systems with lower surface brightness. [Credit: Sales et al. (2020)]

As presented in sec. 5.2, there is a noticeable difference between the fraction of LSBGs when galaxies are segregated by morphology. To complement this previous finding, in Fig. 5.7 we also present the $\ln(2+\delta) - M_*$ plane for central and satellite galaxies, but separating our sample between spiral (middle panels) and elliptical (righ-hand panels) galaxies. In the upper-middle panel of Fig. 5.7, we observe that, for central spiral galaxies, at fixed stellar mass the fraction of LSBGs remains constant when the density increases, except for high-mass galaxies. In the case of elliptical central galaxies (upper right panel) the fraction of LSBGs rises slightly with the density, especially for those galaxies in the low-mass regime. Note that for spiral galaxies, the contours enclose a large range of stellar masses, whereas for elliptical galaxies, the contours only enclose galaxies with stellar mass $M_* < 10^{9-10}\mathrm{M}_\odot$. This is a

good indicator that even when LSBGs are found with different morphologies and stellar masses, massive elliptical galaxies like the ones found in the center of large clusters are not part of the LSBGs population. Taken together, our results indicate that spiral LSBGs are less exposed to interactions than ellipticals, implying that the evolution of the latter is mainly the result of the high-density environments in which these galaxies reside, where processes such as mergers, stripping, and redistribution of their components due to tidal torques are responsible for their nature. More recently, in Zhu et al. (in prep.) we employ TNG100 to explore the origin of the extended disks found in 'giant' LSBGs. We find evidence that giant LSBGs are extended disks without any major mergers since $z = 1$. They have not been disturbed for a long time on a cosmological scale, i.e., they are 'long lived' galaxies. Moreover, the redshift distribution of the last major merger peaks at $z \sim 0.3$ for 'giant' LSBGs, whereas for "normal" galaxies, the peak is found at $z = 0.1$. Therefore, the relatively isolated environment is one of the key parameters that explain the formation mechanism of extended disks. A recent study performed by Saburova et al. (2022) confirmed these latter results, with the aid of a simulated 'giant'LSBGs sample drawn from EAGLE, which reproduces accurately the volume density of these galaxies found in the Subaru HSC Strategic Survey (Aihara et al. 2019), finding that giant extended disks experienced zero major mergers since $z = 3$, indicating that 'giant' LSBGs can be formed via minor mergers and accretion.

In the case of satellite galaxies, we observe that spiral LSBGs populate the low-density regime, indicating that these galaxies are found in relative isolation, implying that spiral galaxies found in groups have higher probabilities to be part of the LSBG population when they are exposed to fewer interactions, they are located in the outskirts of the groups or are recently incorporated to them. Moreover, at high densities, the "absence" of spiral LSBGs indicate that these could be completely destroyed and/or transformed into an elliptical due to interactions. On the other hand, elliptical galaxies populate the region of intermediate densities, where the fraction of LSBGs rises with density, reaches a maximum, and then starts to decrease. This implies that the environment plays an important role on the formation of elliptical LSBGs, as in the case of central galaxies. This result complements the scenario discussed in sec. 5.2. The relative isolation in which LSBGs reside is extensively pointed out by different authors across the literature (Rosenbaum et al. 2009; Galaz et al. 2011; Pérez-Montaño & Cervantes Sodi 2019; Tanoglidis et al. 2021), however, this does not neccessarily imply that LSBGs are formed within low-density environments. Galaxy mergers and encounters with nearby, low-mass galaxies are also a feasible scenario of LSBGs formation due to the accretion of stellar and gas components, promoting the formation of a faint, extended component around massive galaxies. Therefore, it is plausible that LSBGs may have been formed in "normal" or even high density environments (as proposed by Martin et al. (2019)), but eventually LSBGs are found to be isolated due to the fact that their close neighbours have already been ripped out, similarly to what was found in Kulier et al. (2020).

5.4 Two-point correlation function

Another way to characterize the environment in which galaxies reside, is by calculating the two-point correlation function (tpcf) $\xi(r)$ of a galaxy sample. The tpcf (Peebles 1980) is a very common way to measure the probability of finding a galaxy within a distance r of a reference galaxy. It is well known that galaxies are not precisely randomly distributed in the Universe, as they tend to be *clustered*. In other words, the highest probability to find a galaxy occurs just in the vicinity of another galaxy or group of galaxies (Rubin 1954).

In this section, we characterize the spatial distribution of LSBGs in our sample by computing the two-point correlation function. To do so, we employ the `Halotools` package (Hearin et al. 2017)[3], an open-source specialized Python package that allows the building and testing of galaxy-halo connection models. `Halotools` allows the creation of mock universes starting from dark matter halo catalogs drawn from a given cosmological simulation. The package is able of creating mock obseervations of a synthetic galaxy population, allowing the direct comparison with real observations. We employed the `mock-observables`

[3]Available for download at https://halotools.readthedocs.io/en/latest/index.html

sub-package which allows a detailed analysis of halo catalogs and point data. We use the `tpcf` command from the `mock-observables` sub-package to calculate the real space two-point correlation function, with a Davis & Peebles (1983) statistical estimator:

$$1 + \xi(r) = \frac{DD(r)}{DR(r)}, \tag{5.4}$$

where $DD(r)$ is the number of original sample pairs with separations equal to r, $DR(r)$ is the cross-count sum of all pairs within an interval Δr, where one pair member belongs to the original sample and the other is part of a random data set. We apply the `tpcf` command over the spatial coordinates of the galaxies in our sample to calculate the "cross-correlation" function of both, LSBGs and HSBGs, with respect to the full sample of galaxies in TNG100, that is, all the simulated galaxy population found in TNG100, regardless if they are included or not in the LSBGs/HSBGs samples employed in this work. Hereafter, this later will be refereed as "Full-TNG100".

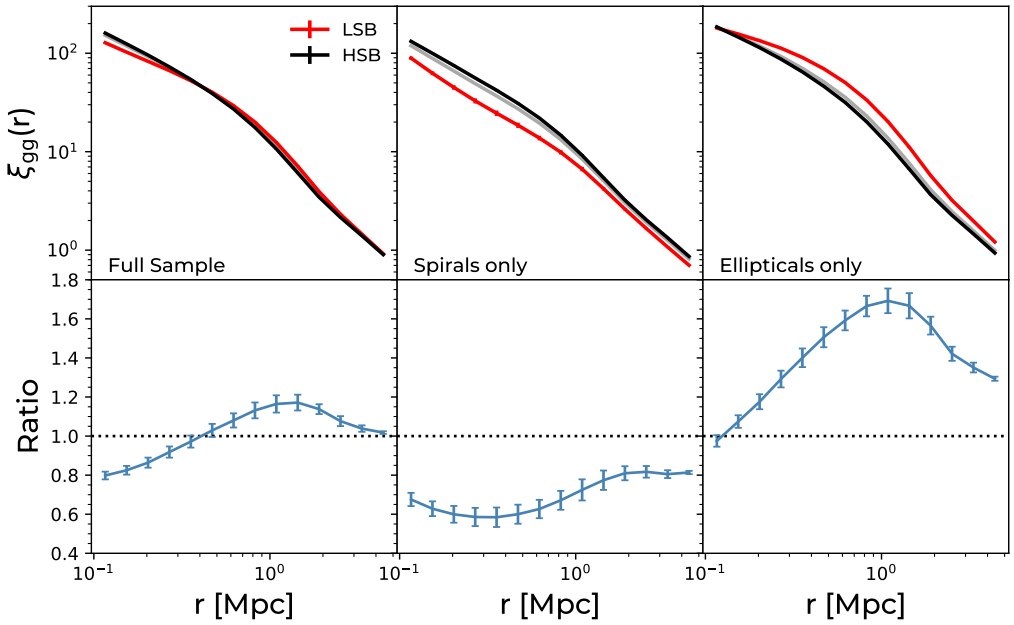

Figure 5.9: *Top row:* The two-point correlation function of LSBGs (red) HSBGs (black) and both (gray) with respect to the Full-TNG100 galaxy population. Error bars represent the dispersion around the values obtained for $\xi(r)$, and are computed with a boostrap re-sampling method, in which we calculate the tpcf over 100 random samples drawn from the original. *Bottom row:* The LSBGs-to-HSBGs ratio of the corresponding values of $\xi(r)$ on each bin. When no morphological segregation is considered (left-hand panels), LSBGs seem to be less clustered than HSBGs up to $r \lesssim 0.4$ Mpc, where the trend is inverted. However, when looking at galaxies of similar morphology, spiral LSBGs are found to be systematically less clustered than HSBGs at different scales, while the opposite is found for ellipticals. Therefore, the relative isolation of spiral LSBGs seems to be a key factor in the 'survival' of their low surface brightness nature. Conversely, elliptical LSBGs are most likely to be a product of the interaction with other galaxies. [Credit: Pérez-Montaño et al. (in prep.)]

The upper panels of Fig. 5.9 show the resulting tpcf of LSBGs, HSBGs, and both (red, black and gray lines, respectively), with respect to the Full-TNG100. The upper-left panel of Fig. 5.9 corresponds to the cross-correlation functions of all the galaxies in our sample, regardless of their morphology. We can observe a clear transition in which LSBGs are less clustered at $r \lesssim 0.4$ Mpc, and beyond this value the trend is inverted. The lower-left panel shows the LSBGs-to-HSBGs ratio of $\xi(r)$, which allows us to observe with more clarity the scales at which the tpcf for LSBGs lies above the one for HSBGs. This

result implies that at small scales, the former are found in relative isolation when compared with HSBGs, but then at larger scales LSBGs seems to be slightly more clustered. This difference is the result of the inclusion of galaxies of all morphological types and the different formation channels between spiral and elliptical galaxies, as suggested by the results found in sec. 5.2 and 5.3. The spatial distribution of LSBGs has been previously studied by Bothun et al. (1993) and Mo, McGaugh, & Bothun (1994). These authors showed that LSBGs are less strongly clustered than HSBGs, and that both galaxy populations follow the same large scale structure, but HSBGs adhere more strongly to it.

Particularly Mo, McGaugh, & Bothun (1994) investigated the clustering properties of LSBGs in the galaxy density field by calculating the cross-correlation functions between LSBGs drawn from the Palomar Observatory Sky Survey (POSS) sample (Schombert et al. 1992) and "trace" galaxies in complete galaxy samples, namely the CfA (Huchra et al. 1983) and IRAS galaxies redshift surveys (Strauss et al. 1992), allowing the authors to compare the amplitudes and shapes of the correlation functions of LSBGs and of 'normal' galaxies. The authors found a similar shape, but lower amplitudes of the cross-correlation functions in the case of LSBGs, implying that LSBGs are embedded in the same large-scale structures as normal galaxies, but the former are significantly less strongly clustered. Fig. 5.10 shows the average cross-correlation function between the POSS sample, the CfA (left-hand panel) and IRAS (right-hand panel) galaxies. In both cases the cross-correlation function is indicated by circles, while the autocorrelation of CfA and IRAS is indicated by empty triangles. With these results, the authors proposed a simple hierarchical model in which LSBGs are formed in halos with no close interactions with other halos, reproducing the deficit of LSBG companions and therefore, the low amplitude of the correlation function, suggesting that LSBGs are on average younger than normal galaxies. According to Mo, McGaugh, & Bothun (1994), halos with low initial density are formed at late epochs, and their model found that LSBGs are formed within those halos. Therefore, LSBGs should be relatively young. Similarly, Tanoglidis et al. (2021) obtained the cross-correlation function between LSBGs and HSBGs drawn from the DES galaxy survey (Abbott et al. 2018) with an external catalog of low-redshift galaxies from 2MPZ (Bilicki et al. 2014), finding a lower amplitude of clustering for LSBGs at angular scales less than $\sim 0.1°$.

As we have shown in sec. 5.3, the density of the local environment of LSBGs is statistically different for late-type and early-type galaxies, showing that early-type galaxies are preferentially found in medium-density environments, while late-type galaxies are most likely to be located in low-density environments. Therefore, these trends will be reflected in the amplitude of the correlation function. Moreover, some previous studies (e.g., Mo et al. 1992; Zehavi et al. 2011) have made emphasis on the differences found in the correlation function between early-type and late-type galaxies. These studies have found that early-type galaxies (elliptical galaxies) are in general more clustered than late-type galaxies (spiral galaxies). Taking this into account, in order to perform a deeper analysis in our results, Fig. 5.9 also shows the cross-correlation function of the galaxies in our sample, segregated between spiral (middle panel) and elliptical (right-hand panel) galaxies. We can observe from Fig. 5.9 a different behaviour in the cross-correlation function found between LSBGs and HSBGs when only spiral/elliptical glaxies are considered.

For spiral galaxies, we observe that LSBGs are systematically less correlated than HSBGs at different scales, which reflects that these systems are in general more isolated than their HSBG counterparts, which is in a goood agreement with we found on Fig. 5.7: Spiral LSBGs may have formed due to secular evolution, rather than external violent processes. We also note that, at larger scales, (about 1 Mpc), the difference between LSBGs and HSBGs is reduced, but there is not an overlap between them. The lower middle panel shows with more detail this trend. On the other hand, elliptical LSBGs exhibit a larger correlation than HSBGs, implying that these galaxies are more exposed to interactions that play an important role in their formation, which is also consistent with what we found in sec. 5.3, where the fraction of LSBGs increases with density. Therefore, we can conclude that elliptical LSBGs are more likely to be formed via external processes, such as mergers, ram-pressure stripping or tidal torques. The fact that these elliptical LSBGs are more correlated is a good reflection of the high-density environments in which these galaxies reside.

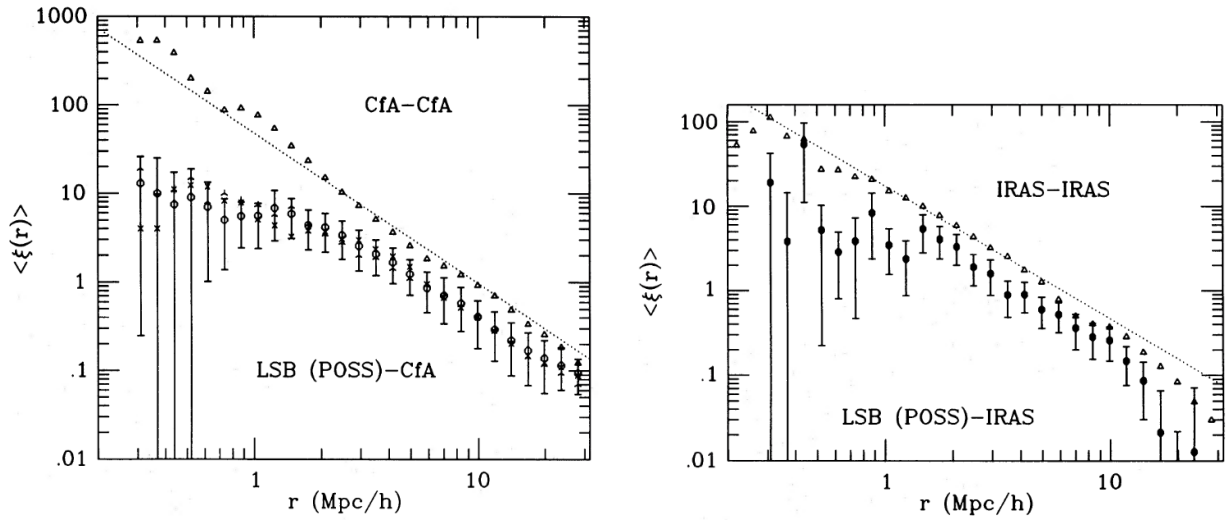

Figure 5.10: The average cross-correlation function between the POSS sample and the observational samples of 'normal' galaxies from CfA (left) and IRAS (right). For each panel, circles denote the cross-correlation between galaxy samples, whereas triangles represent the autocorrelation of a given sample. The straight line corresponds to a differential correlation function $\xi(r) = (6h^{-1}\mathrm{Mpc/r})^{1.7}$, which is approximately the redshift-space autocorrelation function obtained by Davis & Peebles (1983). The amplitude ratios are found to be $A_{LSB-CfA}/A_{CfA-CfA} \approx 0.4$ and $A_{LSB-IRAS}/A_{IRAS-IRAS} \approx 0.6$. [Credit: Mo, McGaugh, & Bothun (1994)]

It is important to point out that the calculation of the cross-correlation function is made by taking into account both central and satellite galaxies. Another important consideration of this analysis is that, given that the cross-correlation function has a strong dependency on the stellar mass of the galaxies considered, in order to suppress any mass dependencies in the interpretation of our results, we tested our implementation of the tpcf calculation over a new set of control samples obtained with the same procedure described in sec. 5.1.2, controlling by mass but now including both, central and satellite galaxies. Once again, we built three different pairs of control samples for this purpose: one for all the galaxies in our sample regardless of their morphology (CS4), and two more pairs of control samples segregated into spiral (CS5) and elliptical galaxies (CS6). A similar KS-test was performed in each control sample to test the hypothesis that the galaxies are drawn from the same distribution. Table 5.2 summarizes the number of galaxies in each pair of control samples, as well as the corresponding $p-$value obtained after performing the KS-test.

Morphology Name	All morphologies CS4	Spirals CS5	Ellipticals CS6
Number of paired galaxies	5,754	3,027	2,432
p-value	0.922	0.995	0.927

Table 5.2: Number of galaxies and the corresponding p-values of the resulting KS test performed in each pair of control samples (LSBGs and HSBGs). By construction each LSBG has associated a HSBG counterpart of similar stellar mass ($\Delta \log(M_*) < 0.05$). Each pair of control samples includes both central and satellite galaxies.

The upper panels of Fig. 5.11 show the `tpcf` of the three different set of control samples constructed for this purpose. We can observe that, for the full sample (left-hand panels), the tpcf does not exhibit the transition found in Fig. 5.9, but it shows that LSBGs are in general less-correlated than HSBGs at different scales. These differences are reduced when increasing r, but these remain without an overlap

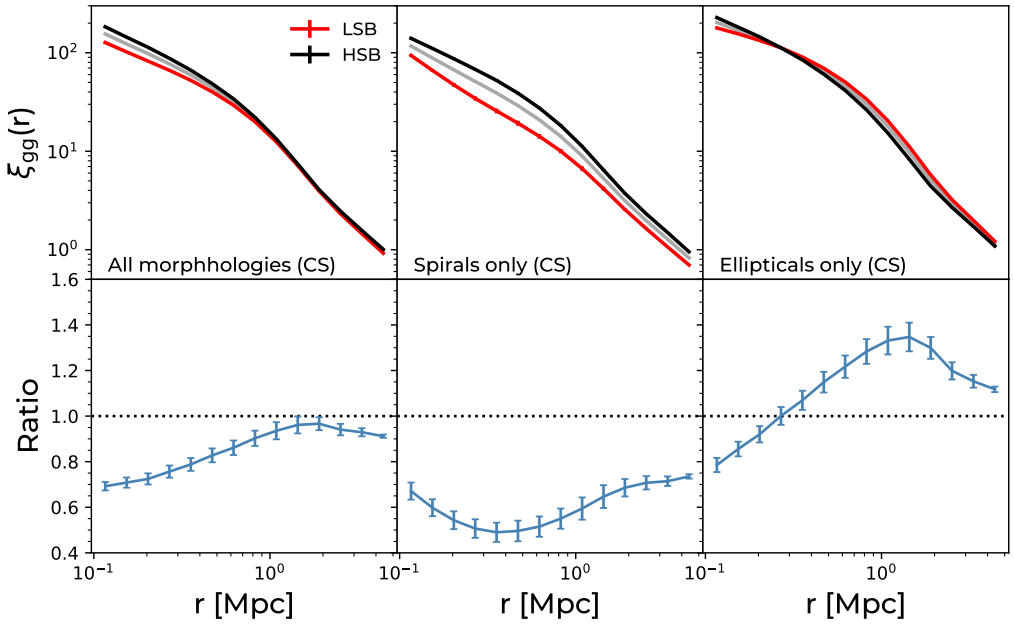

Figure 5.11: Same as in Fig. 5.9, but considering the galaxies in the three pairs of control samples (namely CS4, CS5 and CS6, respectively), which allows to compensate any dependency of the results with stellar mass. In this case, we do not observe a transition between the value of $\xi(r)$ when no morphological segregation is considered. Spiral and elliptical galaxies in control samples follow the same trends as before, where spiral (elliptical) LSBGs are less (more) clustered than HSBGs, reinforcing our previous hypothesis. [Credit: Pérez-Montaño et al. (in prep.)]

between them, allowing us to affirm that, regardless of their morphology, LSBGs are in general less correlated than their HSBGs counterparts of similar stellar mass, which could be interpreted as an indicator of the relatively isolated nature of these galaxies. When we observe the cross-correlation of the control samples segregated by morphology (middle and right-hand panels), we do not observe any important difference with the results presented in Fig. 5.9 for the full sample. Therefore, we can conclude that the differences found in the values of the cross-correlation function of our galaxy sample are mainly due to the LSBG nature of these systems, rather to difference in their stellar mass, which is important due to the fact that LSBGs in our sample are in general less massive than HSBGs, as found in Chapter 3 (Pérez-Montaño et al. 2022) and therefore, less correlated. The differences between elliptical LSBGs and HSBGs in the control samples are found to be quite smaller than when we consider all the elliptical galaxies in our sample, but this could be due to the fact that high-mass elliptical HSBGs are excluded from our control sample by construction, given that the population of elliptical LSBGs in our sample is quite small.

5.5 Large-scale structure

To finally perform a full study of the environment at larger scales, we explore the distribution of LSBGs in our sample with respect to the large scale structure (LSS) of the Universe, i.e., to the patterns of galaxies and matter on scales much larger than individual galaxies or groupings of galaxies, with the aim to find any evidence of a strong influence of it over the formation and evolution of LSBGs in TGN100. The LSS distribution of the galaxies in our sample is drawn from Duckworth, Tojeiro, & Kraljic (2020) and Duckworth et al. (2020), which provide a post-processed identification of the topology of the cosmic web employing the `DisPerSE` code (Sousbie 2011; Sousbie, Pichon, & Kawahara 2011). They identify topological structures such as peaks, voids, walls and filaments. `DisPerSE` uses a set of discrete points (or

galaxies) to estimate the density field and the cosmic web. In this catalog, each point corresponds to a galaxy with $M_* > 10^{8.5}\mathrm{M}_\odot$, and the code is designed to be able to recover the galaxy distribution from an observational survey. This catalog provides the cosmic web distances to the nearest cosmic web structure of a given type. Fig. 5.12 shows the 2D discrete distribution of ∼350,000 particles obtained by projecting a $10h^{-1}$ Mpc slice of a larger $50h^{-1}$ Mpc $N-$body simulation at $z = 0$, in which the identification of the filamentary structure was obtained with the methodology employed by `DisPerSE`[4].

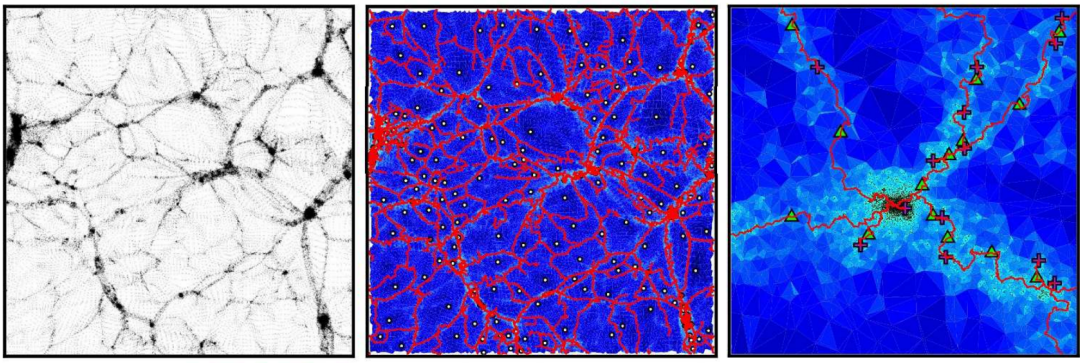

Figure 5.12: The projected filamentary structure obtained from a slice of an $N-$body cosmological simulation. The left-hand panel corresponds to the initial discrete distribution, while the middle panel ilustrates the filamentary structure (red) traced by the code and the minima (white circles) identified. The right-hand panel is a zoom over a halo from the upper middle part of the initial distribution, where green triangles and purple crosses represent saddle-points and maxima, respectively. [Credit: Sousbie (2011)]

The left-hand panel of Fig. 5.13 shows the cumulative distribution function of the distance to the closest of these large-scale structures, segregated between central/satellite galaxies, and spiral/elliptical morphologies. The type of galaxy considered is specified on the $y-$axis of the corresponding row. The structures studied in this work include the distance to the nearest void, node, and filament, as well as the nearest 1 and 2 saddle points, corresponding to the critical points where one/two dimensions are collapsing. We can observe that there is no significant difference between LSBGs and HSBGs in many of them, but there are some relevant exceptions when looking at panels with number 7, 12, 13, 17 and 18. In the right-hand panel, we plot the difference between both distributions, to help us visualize and identify those significant differences and/or fluctuations on the cumulative distributions. We point out these differences in the following paragraphs.

For central elliptical galaxies, we found that LSBGs are slightly closer to nodes than HSBGs (panel 7), which is in good agreement with the results previously mentioned. The closer the galaxy to the node, the closer it is to the center of galaxy clusters. This is another indication that elliptical LSBGs are more likely to be found in high-density environments, where they are subject to many interactions. These favours a scenario in which elliptical LSBGs may have formed due to closer encounters with other galaxies, as well as the accretion of low-mass companions. In contrast, for central spiral galaxies we did not find a significant difference between LSBGs and HSBGs (panels 1-5). This latter is in agreement with many observational studies that fiund no impact of the LSS. This is important for our analysis, given that we do not focus exclusively on late-type LSBGs (e.g., Mo, McGaugh, & Bothun 1994; Pérez-Montaño & Cervantes Sodi 2019), but extend the analysis to the full population of LSBGs. However, including objects in the dwarf regime (Román & Trujillo 2017), typically characterized by early-type morphologies would require a different analysis due to resolution limitations.

[4]Further details on the identification of the large-scale structure and the theory behind the algorithm employed in `DisPerSE` is available on the corresponding papers of Sousbie (2011) and Sousbie, Pichon, & Kawahara (2011)

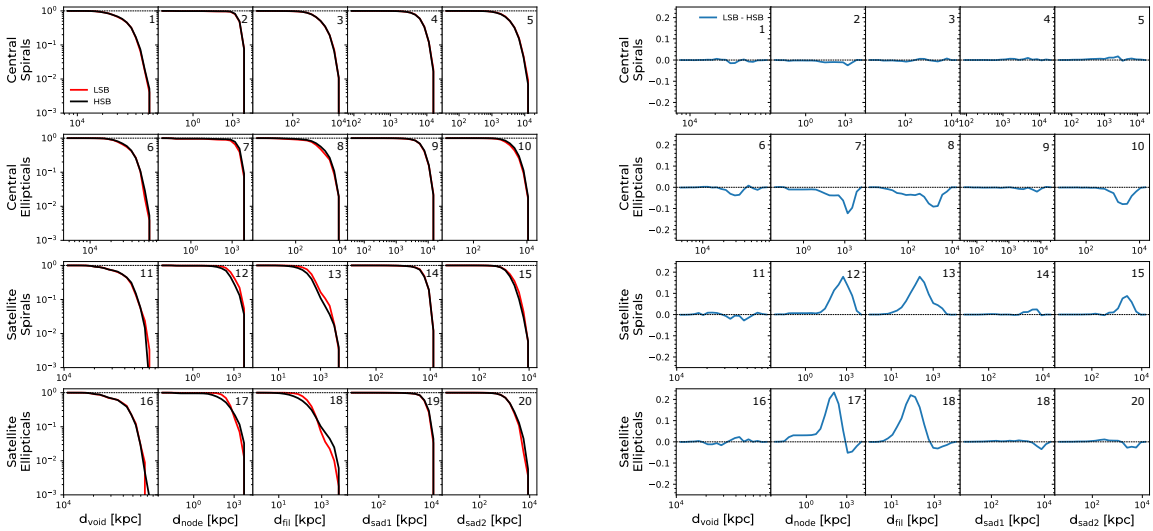

Figure 5.13: *Left panel:* Cumulative distributions of the distance to the nearest large-scale structure for LSBGs and HSBGs, segregating the sample by central/satellite galaxies, and by morphology. *Right panel:* The corresponding δ between cumulative distributions, that allows us to identify easily the difference between both distributions, when there are any. [Credit: Pérez-Montaño et al. (in prep.)]

In the case of satellite galaxies, spiral LSBGs are found to be further away from nodes than HSBGs (panel 12) and, consequently, further away from the center of galaxy clusters. This suggests that the evolution of these galaxies is driven by secular evolution, rather than by galaxy interactions. We observe also that spiral LSBGs are slightly further from nodes than elliptical LSBGs (panel 17), which is consistent with what we found in Figs. 5.5 and 5.7, where most of them are preferentially located in low-density environments. On the other hand, elliptical satellite LSBGs are found also further from nodes than HSBGs, but they seem to be closer to nodes than spiral LSBGs. This corroborates what we showed in Fig. 5.5 when studying the fraction of LSBGs as a function of the distance to the center of the galaxy groups and clusters, where the fraction of LSBGs increases as we move further from the center of galaxy clusters, and the fraction of elliptical LSBGs is larger at all radii. This is also in good agreement with the results in Fig. 5.7, where we found that the fraction of elliptical LSBGs increases with density.

Turning our attention to the distance to the nearest filament (3rd column), the most significant differences are found for satellite galaxies, as we expect from the fact that central galaxies are most likely to be closer to the nodes (and consequently to the center of galaxy clusters). We observe that LSBGs are located further away from filaments than HSBGs, regardless of their morphology. Previous observational studies (Rosenbaum et al. 2009; Pérez-Montaño & Cervantes Sodi 2019) have found a similar trend. A possible explanation of this finding is provided by Rosenbaum et al. (2009), who suggest that galaxies formed in low density environments (such as LSBGs) can "migrate" towards the outer regions of filaments. These authors argue that the isolation of LSBGs found in intermediate and small scales must have a strong impact on their evolution, given that tidal encounters and mergers naturally favour the triggering of star formation episodes, which are not typically found in LSBGs (Boissier et al., 2003). Taking this into account, these authors results provide a scenario in which the observed isolation of LSBGs takes place over scales of $\sim$ 5Mpc, corresponding to the typical size of the large-scale filaments (e.g. White et al. 1987; Doroshkevich et al. 1997). Therefore, LSBGs must have formed within void regions of the large-scale structure, but most of them have migrated to the edges of the filaments because of gravitational infall, while others are still found within voids, in which they have formed.

In order to eliminate any dependence on the stellar mass of our results about the cumulative distribution

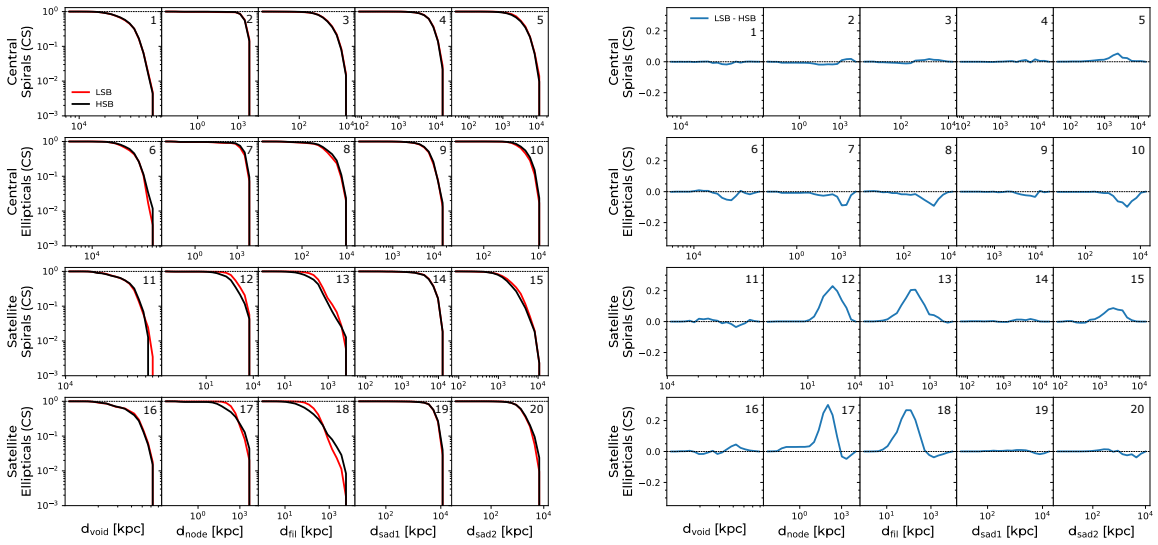

Figure 5.14: Same, as in Fig. 5.13, but considering only galaxies in the corresponding set of control samples (CS7, CS8, CS9 and CS10 in each row, respectively). No significant differences are found with respect to galaxies in the full sample. [Credit: Pérez-Montaño et al. (in prep.)]

of the distance to the nearest structure of the cosmic web, we performed a similar analysis over four sets of control samples following the same procedure described in secs. 5.1.2 and 5.4. In this case, apart from controlling by stellar mass, we also control by galaxy type, i.e., segregating between central and satellite galaxies, as well as morphology. It is well known that low-mass systems are preferentially located close to filaments or nodes rather than voids, so this dependency could strongly affect the interpretation of our results. Fig. 5.14 shows the cumulative distributions and the corresponding differences between the cumulative distributions of LSBGs and HSBGs, for our four sets of control samples. We observe that these are not significantly different from the ones obtained for the full sample. Therefore, the differences found are directly linked to the LSBG nature of these systems, rather thant to their stellar mass.

Galaxy type	Centrals		Satellites	
Morphology	Spirals	Ellipticals	Spirals	Ellipticals
Name	CS7	CS8	CS9	CS10
Number of paired galaxies	2,070	763	863	1,669
$p-$value	0.896	0.955	0.999	0.973

Table 5.3: Number of galaxies and the corresponding p-values of the resulting KS test performed in each pair of control samples (LSBGs and HSBGs). By construction each LSBG has associated a HSBG counterpart of similar stellar mass (Δ log(M_*) < 0.05). For this set of control samples, a segregation between central and satellite galaxies is performed, as well as by morphological type.

It is important to point out that, even when in most of the cases we found no significant differences related to the large-scale distribution between LSBGs and HSBGs, this does not imply that the large-scale structure does not have a strong influence on galaxy properties. In a recent study, Das, Pandey, & Sarkar (2022) studied the major interactions in filaments and walls using a large sample of galaxies drawn from the SDSS, in order to understand the influence of large-scale environments on galaxy interactions. The authors conclude that large-scale structures such as filaments and sheets have a fundamental role in galaxy

interactions, whereby the color $u-r$ and the SFRs of interacting galaxies are not only affected by the local density, but also by the large-scale morphological environment. They found that galaxy pairs with a projected separation < 50 kpc are more star-forming in filaments than pairs hosted in walls. Similarly, at smaller pair separations, galaxy pairs within wall-like structures are significantly redder than galaxy pairs in filaments. We can observe these results in Fig. 5.15, which shows the cumulative median color (top row) and SFR (bottom row) of major galaxy pairs[5] as a function of projected separation for three different magnitude bins. $D1$ and $D2$ characterize the geometric environment around galaxies as filaments and walls, respectively. These results highlight that the most immediate environment, established by the current interaction with the nearest neighbor, clearly has a greater impact on color and SFR than the large-scale structure within which the galaxies reside.

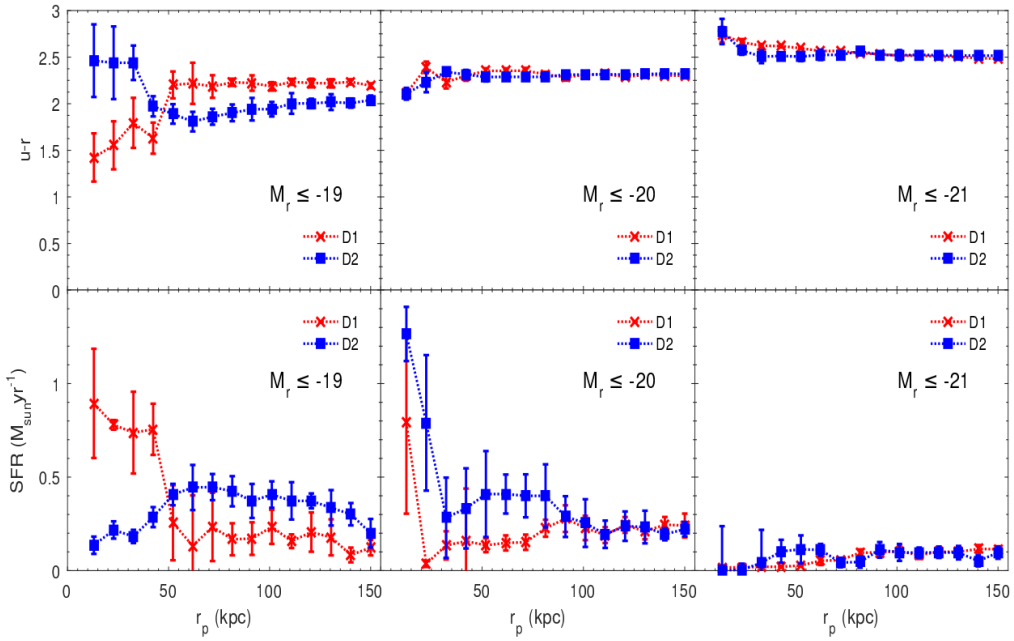

Figure 5.15: Cumulative median colour $u-r$ (top) and SFR (bottom) of major pairs as a function of their projected separation for three magnitude bins. Major pairs residing in filaments and walls in each panel are represented by red and blue symbols, respectively. [Credit: Das, Pandey, & Sarkar (2022)]

However, with respect to the role of the cosmic web over halo properties, in a recent work by Goh et al. (2019), the authors employed the Bolshoi-Planck ΛCDM cosmological simulation (Klypin et al., 2016; Rodríguez-Puebla et al., 2016) to study the effects of the local environment and the cosmic web (namely filaments, walls and voids) over some key properties of DM halos such as the spin parameter, the concentration index, the halo shape, the last major merger, among others. They found that there is no significant difference between the halo properties in filaments, walls or voids at the same environmental density, as seen in Fig. 5.16, where the median values of the mentioned halo properties are plotted as function of the local density for galaxies residing in different structures of the cosmic web, like small walls (blue) and voids (gray). Therefore, this latter should be the main factor affecting halo properties. Since we have already mentioned that the main mechanism for the formation of LSBGs is due to variations in the properties of the halos that contain them, and in particular the spin parameter, those results, together with what we mentioned in Chapter 3 about finding no differences in color and SFR between LSBGs and HSBGs, indicate that the large-scale structure of the universe, although it actually does affect the evolution of galaxies, does not represent a key factor for the "path" that galaxies will follow to become LSBGs or HSBGs. In a recent study performed by Kuutma et al. (2020), the authors found that filamentary structure has a very limited effect on the properties of galaxies in groups, and that the

[5]Defined by the authors as those pairs with $1 \leq M_1/M_2 < 3$

properties of these galaxies depend mostly on their local environment density field. Therefore, we can conclude that, if there is a difference in the LSS distribution between LSBGs and HSBGs, it does not seem to be significantly strong (reaching a maximum of 20% in the most appreciable case, as seen in the right hand panels of Figs. 5.13 and 5.14), allowing us to conclude that the environment on a large scale is not as important as group membership and, of course, the galaxy's own halo.

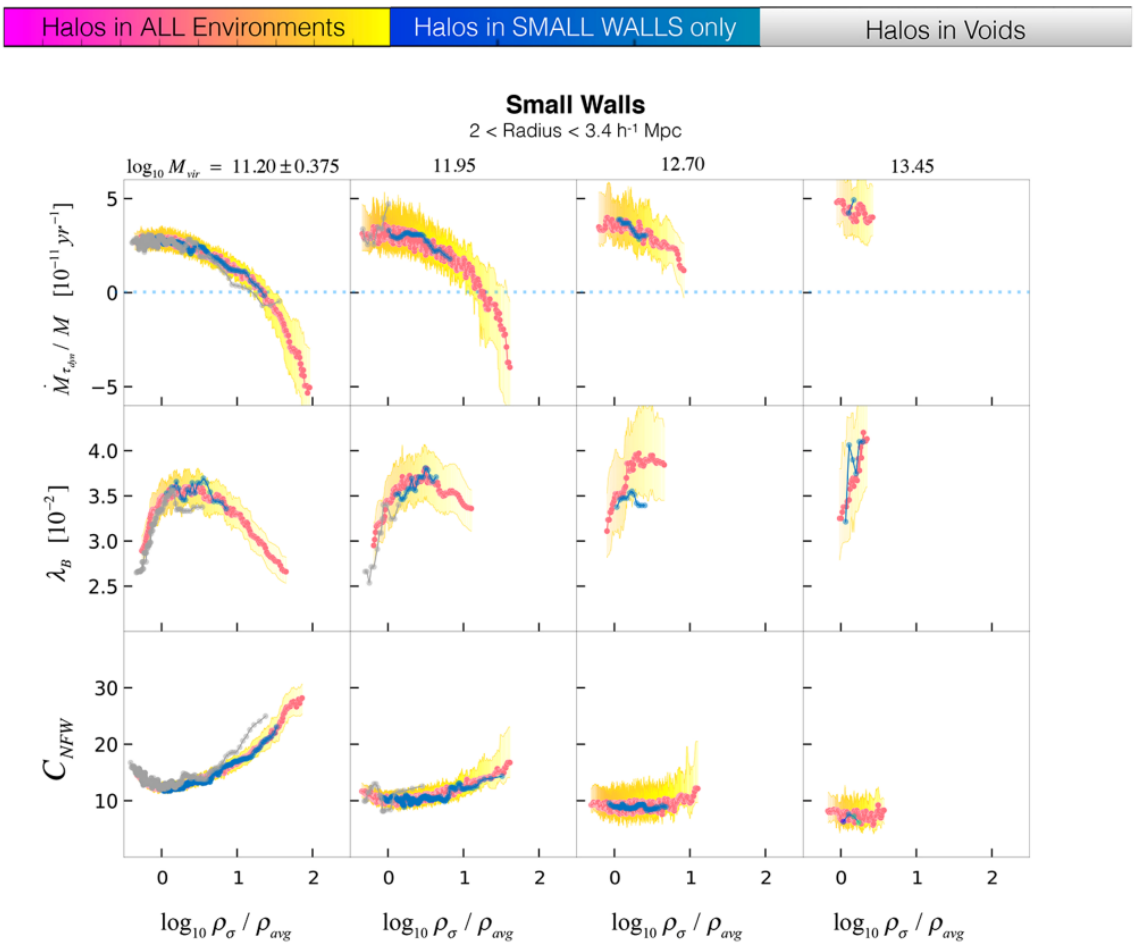

Figure 5.16: Specific mass accretion rate (top row), spin parameter (medium row) and concentration index (bottom row) of DM halos in different web environments, including all (purple dots enclosed by the yellow dispersion), small walls (blue dots), and voids (grey dots) as a function of density. For all these plots, the halo properties seem to be unaffected by the cosmic environment, and they seem to be controlled instead by the local density. [Credit: Goh et al. (2019)]

Chapter 6

Dicussion and Conclusions

In the present work, we employed a sample of simulated galaxies drawn from the IllustrisTNG project, which allowed us to study the main properties of the LSBGs population at $z = 0$, identifying the main differences with respect with their HSBGs counterparts. Our sample was built by considering galaxies with stellar masses in the range $M_* > 10^9$ $M_\odot$, segregating the galaxy population between LSBGs and HSBGs according to their $r-$band surface brightness, considering the flux of those stellar particles within the projected radius r_{50} that contains half of the total luminosity, and considering the galaxies to be placed as 'face-on', in order to avoid any effect of dust extinction. This last consideration does not have a strong impact on the galaxy population segregation, as found by previous studies (Kulier et al. 2020).

We adopted a kinematic criterion (Sales et al. 2010; Sales, et al. 2012) to characterize the morphology of the galaxies in the sample, finding that LSBGs with 10^9–10^{11} $M_\odot$ present predominantly disk morphologies (Fig. 2.6). The fraction of LSBGs found in our sample is high ($\sim 40\%$) for galaxies in the low-mass regime ($10^9 < M_* < 10^{10.5} M_\odot$), and decreasing when increasing the stellar mass. At M_* $\sim 10^{10.5}$ $M_\odot$, the fraction of LSBGs exhibit a clear upturn and increases for galaxies in the high-mass regime. This high fraction of LSBGs found in our sample at low masses is in a good agreement with previous observational studies (Dalcanton et al. 1997; Galaz et al. 2011), while the upturn identified at $M_* \sim 10^{10.5}$ $M_\odot$ is also reported in Kulier et al. (2020), who attributed this to the formation of the most massive LSBGs via accreted stellar mass from mergers, which forms an extended, faint component around these galaxies.

The analysis of the distributions of the main physical properties of the galaxies in our sample (Fig. 3.1) indicates that LSBGs are systematically fainter and with lower SFRs than HSBGs. We also found that LSBGs are less massive and more extended, as frequently found in the literature, mainly focused in observational studies of the local Universe (e.g., Zhong et al. 2008; Galaz et al. 2011; Pérez-Montaño & Cervantes Sodi 2019). After pointing out that LSBGs are less massive than HSBGs, we explored the differences between the two populations of galaxies at fixed stellar mass, in order to eliminate any co-dependency with the mass in the interpretation of our results. With this procedure, we found no differences in the current star formation rates between LSBGs and HSBGs.

The study of the atomic, molecular and total neutral gas content allowed us to conclude that these quantities are substantially higher for LSBGs, which results in a higher baryonic-to-total mass ratio for galaxies with low surface brightness, in good agreement with what it was found by Kulier et al. (2020). With respect to the molecular gas, previous observational studies (Mihos, Spaans, & McGaugh 1999; Cao et al. 2017) have pointed out that LSBGs present a lack of molecular gas, which would explain the low SFRs found in LSBGs. Interestingly this is in contrast with what we found in the LSBGs population in our sample, in which not only the atomic, but also the molecular gas is found in higher fractions in LSBGs than in the case of HSBGs. Although our galaxies generally contain more gas, as long as it remains diffuse, no significant higher level of star formation activity is seen. It has been found in the literature that LSBGs are DM-dominated systems (Pickering et al. 1997; McGaugh, Rubin, & de Blok

2001; Swaters et al. 2003; Kuzio de Naray & Spekkens 2011; Pérez-Montaño & Cervantes Sodi 2019), however in our simulated galaxy sample LSBGs present only a marginally smaller stellar-to-halo mass fraction when compared with HSBGs. This aparent difference between theory and observations could be a consequence ot the stellar/halo mass estimation, which in TNG100 corresponds to the total stellar and dark matter particles enclosed in R_{200}, whereas the estimations from observational studies are restricted to those regions easily traced by a baryonic component, typically much smaller than R_{200}. Our results are also consistent with Zhu et al. (in prep.), in which the rotation curves of a sample of 'giant' LSBGs in TNG100 show little differences in their dark matter mass distributions when compared with a control sample of galaxies with similar stellar mass.

Exploring the assembly and merger histories, we found that the fraction of stellar mass accreted via mergers, $f_{\mathrm{ex-situ}}$, is slightly higher for LSBGs than in HSBGs at the low-mass regime, where the ex-situ stellar fraction contribution is less than 40%. On the other hand, massive LSBGs also exhibit larger ex-situ stellar fractions, but the contribution reaches up to 80%. This later result supports the scenario in which the extended nature of massive LSBGs is highly affected by accreted stellar mass, as pointed out in Kulier et al. (2020). We also find that, for galaxies between 10^9 and 10^{10} $M_{\odot}$, LSBGs experienced their last major merger more recently than HSBGs, indicating that both, smooth accretion and major mergers are relevant in the formation mechanisms of LSBGs. In the work of Di Cintio et al. (2019), the authors proposed that coplanar mergers are able to increase the angular momentum in galaxies, which eventually is translated into a decrease of the surface brightness of galactic disks. Other theoretical studies confirm that interactions between massive galaxies and a less-massive, gas-rich companion are more likely to produce 'giant' LSBGs, such as Malin-1, the archetypical example of this sub-population of galaxies (Zhu, et al. 2018, Zhu et al. submitted). We also found that the DM halos of LSBGs assembled half of their final mass at more recent epochs than HSBGs, in good agreement with what was found by Pérez-Montaño & Cervantes Sodi (2019), supporting the idea that LSBGs could be a population of less evolved systems than their HSBGs counterparts.

The galactic angular momentum and the halo spin parameter (Fig. 3.9) are the two physical parameters that play an important role in the formation of LSBGs, which present substantially higher median values of their specific stellar angular momentum, j_*, and halo spin parameter, λ, than HSBGs. This is in a good agreement with those classical studies (Dalcanton et al. 1997; Jimenez et al. 1998; Mo, Mao & White 1998; Boissier et al. 2003; Salinas & Galaz 2021) that propose the formation os LSBGs within dark matter halos with high values of λ. In recent years, studies using cosmological hydrodinamical simulations have found similar correlations with the halo spin (e.g., Kulier et al. 2020), but also weaker correlations (Jiang et al. 2019) or even opposite trends (Martin et al. 2019). We found that LSBGs not only present higher λ and j_* values, but also a higher 'retention fraction' (j_*/j_{200}) of angular momentum than HSBGs; however, this latter result is a consequence of their late-type morphologies, as previously found in Rodriguez-Gomez et al. (2022). Taking all these findings into account, we can argue that the high angular momentum in these galaxies is the main agent responsible for the low surface brightness nature of these systems. These fundamental differencies in the angular momentum and spin parameter between LSBGs and HSBGs are also reported in observational studies (Pérez-Montaño & Cervantes Sodi 2019; Salinas & Galaz 2021).

We also studied the mass and accretion rate of the SMBHs at the centres of our galaxies, finding that LSBGs have less massive SMBHs than the ones found in HSBGs, and with lower accretion rates. This could be the result of the high angular momentum and spin parameter found in LSBGs. This high angular momentum would prevent the material to flow towards the inner regions of these galaxies and fuel the SMBHs, as proposed by Cervantes-Sodi et al. (2011). A similar result was also found by Rodriguez-Gomez et al. (2022) employing the TNG100 simulation: a less efficient gas inflow towards the galactic center is attributed to those systems with higher angular momentum. The lower occurence of stellar bars in this galaxy population seems to be another key factor that contributes to the low accretion rates and SMBHs masses, as has been previously pointed out by previous studies (Honey et al. 2016; Cervantes Sodi & Sánchez García 2017). Galactic bars promote the redistribution of the stellar, gas, and dark matter components of the galaxies, and the transference of gas that can be used as fuel for the

SMBHs.

Related to the redshift evolution of the galaxies in our sample, we have employed the `SubLink` merger trees (Rodriguez-Gomez et al. 2015) to characterize the main branch of our $z = 0$ LSBGs and HSBGs. This allows us to trace back the evolution of the physical properties of the parent halos in which these two population of galaxies reside nowadays. We found that LSBGs and HSBGs have similar stellar mass formation histories, but other properties such as their sizes, exhibit a smooth but clear bifurcation in their evolutionary tracks at $z \sim 0.5 - 1.5$, in which the half-mass radius is increased for the case of LSBGs. A similar behavior is found when analyzing the evolutionary track of the specific angular momentum and spin parameter (Fig. 4.3), but the divergence in the latter occurs at slightly higher redshift, about $z \sim 2$, which suggests that the increase in the spin parameter may have causal effects on other physical properties of LSBGs, such as their size, specific angular momentum, and resolved star formation.

Analogously, we have explored the evolution of the sSFR in the galaxies of our sample, in order to further understand the origin of the extended nature of LSBGs. Given that we did not find a clear difference in the sSFR between LSBGs and HSBGs, we studied the evolutionary tracks of the resolved star formation histories within and outside $r_{\rm half}$, respectively. At low redshift ($z < 1.5$), the central sSFR in galaxies with stellar masses of $10^9 - 10^{10}$ $M_\odot$ is less intense for LSBGs than for HSBGs, whereas the "outer" sSFR is more intense (Fig. 4.6). This result is very consistent with what was found by Zhu, et al. (2018) and Di Cintio et al. (2019). According to these authors, LSBGs are formed from the accretion of high angular momentum material that promotes star formation at larger radii. In a recent study, Wright et al. (2021) proposed that an increase in halo spin parameter can cause a redistribution of the star formation activity to the outskirts of galaxies, which reduces the central star formation rate, a phenomenon that might explain the resulting evolutionary tracks found in our sample.

In a recent review, McGaugh (2021) pointed out that the main differences between LSBGs and HSBGs, such as their sizes and naturally the surface brightness, can be explained by two different hypotheses: variations of the spin parameter of the dark matter halo, and variations of the halo density (McGaugh & de Blok, 1998), which is characterized by the halo concentration index c_{200}. To test this hypotheses, we compared the median values of λ and c_{200} as a function of stellar mass of LSBGs and HSBGs, annd found that the typical value of the spin for LSBGs, regardless of their morphological type, is systematically larger than the one presented by HSBGs, while the concentration indexes of both subsamples are indistinguishable (Fig. 5.1). Our results clearly supports the hypothesis that the valye of λ is the key parameter that determines the low surface brightness nature of these systems. However, other studies such as Kulier et al. (2020) found that LSBGs are more likely to inhabit more concentrated halos. The authors argue that this is probably due to the strong correlation found between the age of central galaxies and their star formation rates for galaxies in EAGLE, such that older galaxies reside within more concentrated halos. Given that we found no difference in the stellar ages of central LSBGs and HSBGs, no differences are expected in the values of c_{200} for galaxies in TNG100. We also explored the geometry of the dark matter halos inhabited by the galaxies in our sample, finding that they tend to be more spherical for LSBGs than for their high surface brightness counterparts, although the distribution of their axis ratios are not dramatically different (Fig. 5.3).

Different authors have pointed out the existence of an alignment between stellar and dark matter angular mometum vectors, a natural consequence of the common origin and co-evolution of proto-galaxies together with their associated proto-halo, and the dynamical response of the alignment to the assembly of the baryonic disk (e.g., Bailin et al. 2005; Bett et al. 2010; Velliscig et al. 2015). We computed the specific angular momentum of the dark matter component in a similar way as for the stellar component, considering all the dark matter particles enclosed in R_{200}. We calculated the dot product between $\vec{j}_*$ and $\vec{j}_{200}$ to obtain the angle between both components, and found that the median values of $\theta_{*,\rm DM}$ are systematically lower in LSBGs than in HSBGs, which indicates a stronger alignment between both components in LSBGs. Aligned components will favour total angular momentum conservation. In a previous work by Bullock, et al. (2001), the authors study the angular momentum profiles of a sample of halos drawn from an N-body simulation. In such work, the authors studied the alignment of the angular

momentum throughout different "shells" within the whole halo volume. They conclude that halos with misaligned angular momentum distributions are unlikely to host large disk galaxies, such as the HSBGs population in our simulated sample.

Extending our analysis to larger scales, we studied the impact of the group environment in which LSBGs reside. It is well known that the properties of galaxies residing in groups are affected by the interactions between them, such is the case of morphology (Tempel et al. 2011; Pearson et al. 2021) and star formation rates (Raichoor & Andreon 2012; Barsanti et al. 2018). We quantified the fraction of satellite LSBGs as a function of the 3D distance to the center of its corresponding group, that is, to the central galaxy, normalized by the characteristic main halo size R_{200}. We found that the fraction of LSBGs increases with the distance to the center of the group (Fig. 5.5), indicating that the external parts of the groups are more favorable for the formation and/or preservation of LSBGs. For low/medium mass galaxies the fraction of LSBGs depends on the distance to the center of the group, but for high-mass galaxies such dependency is not observed, suggesting that these galaxies are massive enough to "survive" violent events. Interestingly, we noted a lack of spiral LSBGs at $r/R_{200} > 0.4$, compared to elliptical galaxies. This could be indicative of different evolutionary scenarios: LSBGs with spiral morphologies are most likely to "survive" and remain as LSBGs when they inhabit less-dense environments with no violent interactions. These eventually destroy the disks, or transform them into spheroids. This scenario is in good agreement with what was found by Kulier et al. (2020), who found that LSBGs are further away from their closest neighbour than HSBGs, implying that the former are not only formed in isolated environments, but may also be formed in denser environments, where massive galaxies accrete their neighbours. Such close encounters tend to disrupt LSBGs, leading to the formation of galaxies with an extended stellar component. The transition from disks to spheroids caused by interactions via ram pressure stripping and tidal interactions could explain the lower number of spiral LSBGs found within galaxy groups (Koda et al., 2015).

To complement this previous analysis, in order to study the impact of the host groups on LSBGs evolution not only of satellites, but also of central galaxies, we characterized the environment by the density field δ computed by Vogelsberger et al. (2014), which is based on the distance of any given galaxy to its 5th nearest neighbour with an $r-$band absolute magnitude < -19.5. We explored the fraction of LSBGs in the stellar mass vs density plane, finding that, at fixed stellar mass, the fraction of central LSBGs does not exhibit a strong dependency with the environment. This suggests that the environment is not a key factor for the formation and/or evolution of central LSBGs. In the case of central galaxies with spiral morphologies, these are preferentially found in low-density environments, due to the fact that they are likely destroyed by close, violent events. By contrast, satellite LSBGs are found in environments with a wider density range, with satellite spirals populating the low-density regime, and elliptical satellites found in higher densities. Mechanisms such as the tidal stripping of the stellar component can drastically reduce the stellar mass of LSBGs, while keeping their sizes constant, such that galaxies with a strong tidal stripping can be transformed into galaxies with a lower surface brightness than expected for a given stellar mass. This latter scenario was proposed by Sales et al. (2020) to explain the origin of UDGs within clusters, especially the ones that have been 'born' within them. The authors employed a sample of UDGs drawn from TNG100, so we can argue that a similar mechanism is expected to occur in our LSBGs sample, even when galaxies with $M_* < 10^9 \mathrm{M}_\odot$ are not included in the current work. These mechanisms would also explain the formation of LSBGs in galaxy groups given the variety of sizes and morphologies found in our sample. Taken altogether, our results indicate that the environment has different effects depending on the morphology of the galaxies, i.e., spiral LSBGs have been less exposed to strong interactions than elliptical LSBGs. This implies that the evolution of elliptical LSBGs is intimately linked with high-density environments, where mergers, tidal interactions and ram-pressure stripping phenomena are responsible of their nature. These findings are in good agreement with what was found by Zhu et al. (submitted) and Saburova et al. (2021), who concluded that the abscence of major mergers between $z = 1 - 3$ is crucial for the survival of large stellar disks.

Another interesting way to characterize the environment is by calculating the tpcf of a galaxy sample. We employed the open-source python package `Halotools` (Hearin et al. , 2017) to compute the cross-

correlation function of LSBGs and HSBGs with respect to the full TNG100 galaxy population. Previous studies (Bothun et al. 1993; Mo, McGaugh, & Bothun 1994) had found that LSBGs are less strongly clustered than HSBGs, a trend we confirmed in our galaxy sample at scales of $r \lesssim 0.4$ Mpc (Fig. 5.9). Above this limit, we found a stronger clustering in LSBGs. This change in the amplitude of $\xi(r)$ is mainly due to the fact that spiral LSBGs are the ones that dominate the low-density regime, whereas elliptical LSBGs are more likely to reside in high-density environments. This result is in a good agreement with the results of Einasto (1991), Mo et al. (1992) and Zehavi et al. (2011), who found that late-type galaxies are in general less clustered. To eliminate any mass dependence in the interpretation of our results, we repeated this experiment over three sets of control samples, in which for each LSBG, an HSBG counterpart of similar mass (and when needed, similar morphology) is assigned (Fig. 5.11). When no morphological segregation is considered, LSBGs are found to be less clustered than HSBGs at all scales. However, when we divide our galaxies by morphology, spiral LSBGs are systematically less clustered than HSBGs, while the opposite is observed for elliptical LSBGs. In this latter case, the difference between LSBGs and HSBGs is reduced when only elliptical galaxies are considered, probably due to the fact that high-mass elliptical HSBGs are excluded from our control sample by construction, given that the population of high-mass elliptical LSBGs in our sample is quite small, making them difficult to associate in pairs. The clustering on scales smaller than $1h^{-1}$ Mpc is due to pairs of galaxies within the same parent halo, which is better known as "the one-halo term" (i.e. Peacock & Smith (2000) and Benson et al. (2000)). On the other hand, the clustering on scales larger than a typical halo($\sim 1-2h^{-1}$ Mpc) corresponds to pairs of galaxies in separate halos, also known as "two-halo term". With this in mind, our results indicate that LSBGs are less clustered in scales $< 1h^{-1}$ than in those $> 2h^{-1}$ (that is, LSBGs are less clustered within a given halo), indicating that LSBGs do not have close neighbours within their virial radius. This result highlights that processes of galaxy formation and evolution depend on the environment, at least in scales within 1-2 Mpc, which are comparable with the mean size of galaxy clusters (Einasto, 1991). The existence of such a morphology-density relation is strongly related to galaxy interactions, which lead to the formation of elliptical galaxies and the disruption of less-massive stellar disks via mergers and ram-pressure stripping.

Finally, we studied the distribution of our galaxy sample within the filamentrary large-scale structure. For each galaxy, we studied the distance to the nearest cosmic web structure, namely voids, walls, filaments, nodes, and saddle points. These distances were drawn from the catalogues of Duckworth, Tojeiro, & Kraljic (2020) and Duckworth et al. (2020), where the authors employed the `DisPerSE` code (Sousbie 2011; Sousbie, Pichon, & Kawahara 2011) to identify the cosmic web distribution. We segregated our galaxy sample between central/satellite galaxies, and considered spiral/elliptical morphologies (Fig. 5.13). We found no significant differences between LSBGs and HSBGs in many of them, but for counted exceptions. We found that elliptical LSBGs are in general closer to nodes than elliptical HSBGs, meaning that most of central elliptical galaxies are closer to the center of their residing galaxy cluster, making them subject to many galaxy interactions which are responsible of their nature. By contrast, no differences are found between spiral LSBGs and HSBGs, in line with previus observational studies (e.g., Mo, McGaugh, & Bothun 1994; Pérez-Montaño & Cervantes Sodi 2019; Román & Trujillo 2017). This result highlights the importance of the environment in the morphology of LSBGs, since the fact that elliptical LSBGs are found in denser environments (such as nodes) implies that interactions are the main responsible for their nature, in contrast with spirals, whose "excess" of interactions could even destroy them.

In the case of satellite galaxies, LSBGs are located further away from their closer filament than HSBGs with the same morphology, in good agreement with observational studies (Rosenbaum et al. 2009; Pérez-Montaño & Cervantes Sodi 2019). These authors argued that galaxies formed in low density environments (such as LSBGs) can "migrate" towards the outer regions of filaments. Therefore, LSBGs must have formed within void regions of the large-scale structure, but most of them have migrated to te edges of the filaments due to gravitational infall. The very little differences found in the large-scale structure distribution between LSBGs and HSBGs (about 20% in the most representative case) allow us to affirm that the large-scale structure of the Universe has a very minor role in the determination of the low surface brightness nature of the galaxies in our sample. In a recent study perfomed by Kuutma et al.

(2020), the authors found that filamentary structure has a very limited effect on the properties of galaxies, particularly in the brightest group galaxies (BGGs, and that the properties of these galaxies depend mostly on their local environment density field. Even when large-scale structures have a fundamental role in galaxy interactions that affect some properties of galaxies, such as their SFRs and color (Das, Pandey, & Sarkar, 2022), they will equally affect LSBGs and HSBGs.

6.1 Summary

Altogether, our main results can be summarized as follows:

(i) LSBGs are found to be less massive, more gas-rich, more extended than HSBGs, and mostly exhibit late-type morphologies.

(ii) LSBGs have less massive BHs and lower BH accretion rates than HSBGs, probably due to their higher angular momentum, that prevents the material to fall towards the central regions of the galaxy.

(iii) The DM haloes of LSBGs assemble half of their final mass in slightly more recent times than HSBGs, reaffirming, together with their younger stellar populations, the hypothesis that LSBGs are marginally younger objects.

(iv) At fixed stellar mass, LSBGs exhibit systematically higher halo spin parameters and angular momentum 'retention fractions' than HSBGs. The combination of these two parameters results in a higher stellar specific angular momentum, determining their low surface .

(v) LSBGs are formed within marginally more massive DM halos with larger amounts of baryonic material, mainly in the form of non-star-forming gas, than those of HSBGs.

(vi) Studying the redshift evolution of the main properties of the galaxies in our sample, the values of λ and j_* show a clear bifurcation between LSBGs and HSBGs at $z \sim 2 - 1.5$ and, as a consequence, the star formation activity seems to be affected. Around $z \sim 1 - 0.5$, LSBGs and HSBGs have similar star formation histories, but then both populations diverge, especially when we compare the star formation activity in their inner and outer regions. The star formation activity of LSBGs is more extended than the one present in HSBGs.

(vii) The differences in the halo spin parameter distributions between LSBGs and HSBGs are most likely to be the main responsible agent of their nature, rather than the density concentration of the DM halo.

(viii) The specific stellar angular momentum j_* of LSBGs has a stronger alignment with the dark matter component j_{200} than in HSBGs, and a narrower distribution.

(ix) Spiral LSBGs are most likely to be formed and in low-density environments, which allow them to 'survive' as LSBGs trough cosmic time. By contrast, elliptical LSBGs may have formed by violent encounters and mergers that extend their stellar component over large areas. This is reflected in the cross correlation function found for LSBGs and HSBGs of different morphologies.

(x) LSBGs not necessarily are born within low-density environments. The accretion and destruction of their close companions by massive galaxies are probably a key factor of their relative isolation.

(xi) There is not a significant difference in the distance to the closest large-scale structure (nodes and filaments) between LSBGs and HSBGs, except for counted exceptions (nodes and filaments), when studying the large-scale structure impact on their observed properties.

In summary, our results indicate that LSBGs tend to be systems with high amounts of angular momentum and cold gas, probably as a result of the higher spin parameter of their host haloes, as predicted in the classical framework of galaxy formation for these kind of galaxies. While the total sSFRs of LSBGs and HSBGs do not differ significantly, the spatial distribution of the sSFR is more extended in the case of LSBGs, being higher in the outer regions than in HSBGs. Although we find that mergers also favour the formation of LSBGs, their effect becomes more important at the massive end, in the regime of so-called *giant* LSBGs (e.g. Zhu, et al. 2018, Zhu et al., in prep.). On the other hand, environmental effects are believed to be more important for the formation of the so-called *Ultra Diffuse Galaxies* (UDGs) (e.g. Tremmel et al. 2020; Benavides et al. 2021), at even fainter surface brightnesses. In upcoming work, it will be interesting to explore the combined effect of mergers and environment on our sample

of LSBGs. Finally, our results motivate future studies of LSBGs using deeper galaxy surveys, such as Euclid and LSST, as well as more direct comparisons between observations and simulations.

According to the proposed scenarios by McGaugh (2021), the formation mechanism of LSBGs is mainly dictated by the evolution of the angular momentum and spin parameter rather than through variations in halo density. The environment at group scales is a key factor for those phenomena that affect the evolution of the angular momentum (Einasto, 1991). These environment also affects morphology, and denser environments tend to produce elliptical HSBGs. The small differences in the distance to the nearest large-scale structure of the Universe between LSBGs and HSBGs indicates that this does not have a strong impact on the determination of low surface brightness. Even when the large-scale structure of the Universe has a significant impact on the general properties of galaxies, such as SFR and color (Das, Pandey, & Sarkar, 2022), it seems to affect both LSBGs and HSBGs equally, explaining the marginal differences found in the color and SFRs of the galaxies in our sample Pérez-Montaño et al. (2022).

Chapter 7

Future Work

Based on the main results of the current work, I am interested in studying the evolution of surface brightness μ_r as a function of redshift, by employing the SUBLINK Merger Trees (Rodriguez-Gomez et al. , 2015). For that purpose, an alternative definition of μ must be adopted for comparison with the definition employed in Pérez-Montaño et al. (2022), given that the definition employed was related with the surface brightness within the effective radius which encloses half the total luminosity, and this quantity is expected to change with time due to the expected evolution of galaxy sizes and consequently, the effective radius. The best choice is to compute the surface brightness of the galaxies by considering the flux of the stellar particles within a fixed circular aperture (e.g., 2-5 kpc), or the extrapolated value at the center of the galaxy using an analytic profile (i.e., exponential). The main goal of this procedure is to determine the key factors that affect the evolution of the surface brightness, such as number of mergers before and after $z = 2$, and the redshift at which the differences in the evolutionary track of LSBGs and HSBGs arise. A possible morphology evolution could be followed by studying the kinematic criterion κ_{rot}, feedback mechanisms and stellar and gas redistribution. Looking at the evolutionary tracks of surface brightness will allow us to determine if LSBGs have always been LSBGs, if there is a transition from HSBGs to LSBGs, or if the galactic systems experience continuous transformations in their central surface brightness. Fig. 7.1 ilustrates an example of this behaviour with galaxies from the NIHAO simulation.

If this transition exists, the natural step is to determine if this transition occurs due to secular evolution in these galaxies, or a consequence of external processes and the influence of environment. We will calculate the spin parameter according to an alternative definition to the traditional one established by Peebles (1971), proposed by Bullock, et al. (2001), as well as the specific angular momentum of the stellar component of the galaxies in our sample. We will trace back the evolution of these two quantities using the SUBLINK merger trees, up to the redshift where the evolutionary track exhibits a clear bifurcation. I am interested in studying the main mechanisms responsible of this bifurcation in the evolution of λ, in order to establish if there is a relationship between merger parameters, such as stellar mass ratios, gas fractions, number of mergers, angular momentum alignment, etc., and the rising values of the spin parameter, which in turn has a direct impact on the surface brightness evolution. I am also interested in developing a more detailed study of the accretion histories and the growth of super massive black holes, and of the relation they hold with the angular momentum configuration. In addition to the changes in μ, I attempt to study changes in the morphology of the galaxies analyzed, as recent cosmological simulations have shown that galaxy morphology is not a fixed property, but fluctuates in time (Park et al., 2022).

Another idea I came up with, is to reinforce the hypothesis in which the formation of an extended component around LSBGs is due to the accretion of stars and gas coming directly from a close companion or trough filaments. To characterize this, I am interested in performing an analysis of the dynamics of the stellar component or, more specifically, in obtaining "angular momentum profiles" $j(r)$ of the stellar and gas components. This could allow in principle the identification of any difference in the angular momentum of the stars and gas between the inner regions and the outskirts. Differences could be

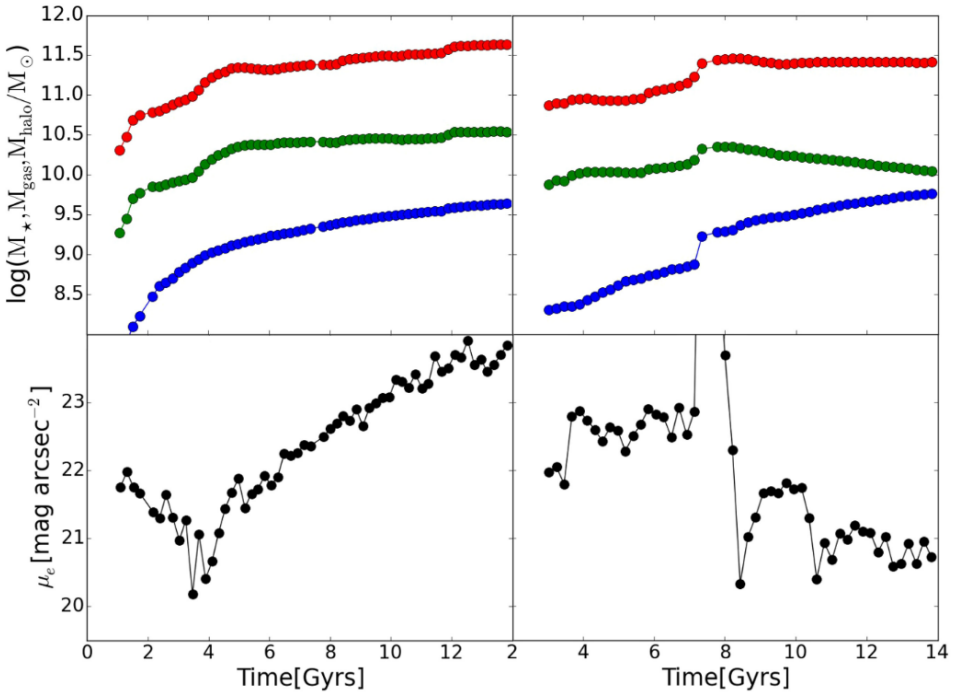

Figure 7.1: *Top row*: Halo (red), gas (green), and stellar (blue) mass accretion history comparison between an LSBG (left) and a HSBG (right) in the NIHAO simulation. *Bottom row*: Temporal evolution of the effective surface brightess. Mergers at $\sim$ 3.5 and 7 Myr can be identified, increasing or decreasing, respectively, the values of μ_e. [Credit: Di Cintio et al. (2019)]

indicative of an uncommon origin of these components, and of the main dynamical differences between both regions. Moreover, this exercise could be helpful to identify a possible "cut-off radius" in which the differences are more notorious. Another way to characterize this is by analyzing the ratio between the total angular momentum of the in-situ and ex-situ components (which are available on the TNG catalogues), allowing us to identify any difference between them (which is highly probable). I attempt to perform this experiment with the aid of TNG50.

I will continue to explore the formation of LSBGs, but now by focusing on the origin of the most extended components of massive galaxies ($M_* > 10^{12}$M$_\odot$). To do so, in Zhu et al. (in prep.) we study the population of the so-called 'giant' LSBGs in TNG100, in order to provide a feasible scenario that allows us to understand the origin of these very particular objects, based on those proposed by different authors across the literature. Fig. 7.2 shows the spin parameter distribution of the 'giant' LSBGs population in TGN100, which reinforces the hypothesis that these objects are formed within DM halos with larger values of λ than "classical" LSBGs. However, preliminary results indicate that this is not the only feasible scenario. This collaboration will allow us to complement the results drawn from this thesis, extending the analysis to the most massive low surface brightnes galaxies, providing a general picture of the main mechanisms invovled in the formation of such extended sources. Another current collaboration is related with the presence of galactic bars in LSBGs. Observationally, LSBGs are well known to be objects with no significant presence of galactic bars (Cervantes Sodi & Sánchez García, 2017). In Chim et al. (in prep.), we attempt to characterize this population by a close collaboration to understand the environment around barred galaxies in TNG100, especially those with low surface brightness.

Finally, I am interested in studying the star formation histories in LSBGs at different mass ranges, specifically, I intend to study the spatial distribution of their star formation. This could be an interesting follow-up to the current work, where we found that LSBGs have stronger star formation activity en the

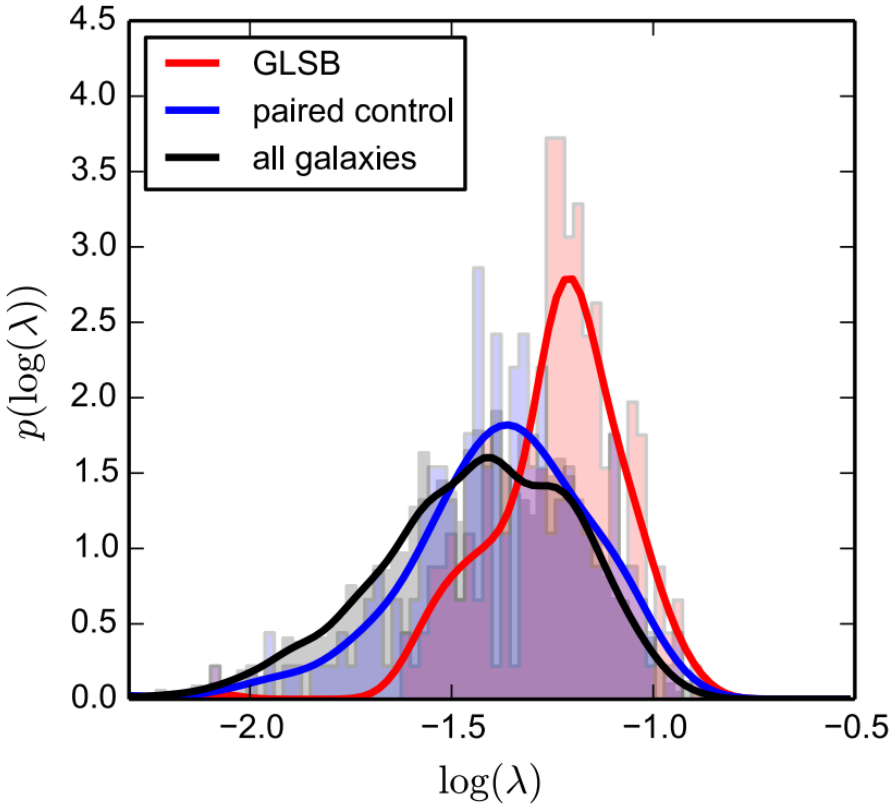

Figure 7.2: The spin parameter distribution of 'giant' LSBGs (red) in TNG100. These galaxies tend to reside in halos with higher spin parameter, with a median $\lambda = 0.06$ when compared to a control sample of galaxies with similar stellar masses, whose median value is $\lambda \sim 0.04$.[Credit: Zhu et al. (submitted)]

outskirts than HSBGs (Di Cintio et al., 2019). This experiment can be performed in both simulations, where star formation can be easily traced back with the aid of merger trees, and observations, in which we expect to find a radial colour gradient as a signature of SFH.

Bibliography

Abbott T. M. C., Abdalla F. B., Allam S., Amara A., Annis J., Asorey J., Avila S., et al., 2018, ApJS, 239, 18

Aihara H., AlSayyad Y., Ando M., Armstrong R., Bosch J., Egami E., Furusawa H., et al., 2019, PASJ, 71, 114

Amorisco N. C., Loeb A., 2016, MNRAS, 459, L51

Anbajagane D., Evrard A. E., Farahi A., 2022, MNRAS, 509, 3441

Athanassoula E., 2002, ApJL, 569, L83

Athanassoula E., Machado R. E. G., Rodionov S. A., 2013, MNRAS, 429, 1949

Avila S., Knebe A., Pearce F. R., Schneider A., Srisawat C., Thomas P. A., Behroozi P., et al., 2014, MNRAS, 441, 3488

Bailin J., Kawata D., Gibson B. K., Steinmetz M., Navarro J. F., Brook C. B., Gill S. P. D., et al., 2005, ApJL, 627, L17

Bakos J., Trujillo I., 2012, arXiv, arXiv:1204.3082

Balogh M. L., Schade D., Morris S. L., Yee H. K. C., Carlberg R. G., Ellingson E., 1998, ApJL, 504, L75

Barsanti S., Owers M. S., Brough S., Davies L. J. M., Driver S. P., Gunawardhana M. L. P., Holwerda B. W., et al., 2018, ApJ, 857, 71

Benavides J. A., Sales L. V., Abadi M. G., Pillepich A., Nelson D., Marinacci F., Cooper M., et al., 2021, NatAs, 5, 1255

Benson A. J., Cole S., Frenk C. S., Baugh C. M., Lacey C. G., 2000, MNRAS, 311, 793

Bett P., Eke V., Frenk C. S., Jenkins A., Okamoto T., 2010, MNRAS, 404, 1137

Bilicki M., Jarrett T. H., Peacock J. A., Cluver M. E., Steward L., 2014, ApJS, 210, 9

Boissier, S., Monnier Ragaigne, D., Prantzos, N., et al. 2003, MNRAS, 343, 653

Bondi H., 1952, MNRAS, 112, 195

Booth C. M., Schaye J., 2009, MNRAS, 398, 53

Booth C. M., Schaye J., 2010, MNRAS, 405, L1

Bothun G. D., Impey C. D., Malin D. F., Mould J. R., 1987, AJ, 94, 23

Bothun G. D., Schombert J. M., Impey C. D., Sprayberry D., McGaugh S. S., 1993, AJ, 106, 530

Boylan-Kolchin M., Springel V., White S. D. M., Jenkins A., Lemson G., 2009, MNRAS, 398, 1150

Brinchmann, J., Charlot, S., White, S. D. M., et al. 2004, MNRAS, 351, 1151

Bruzual G., Charlot S., 2003, MNRAS, 344, 1000. doi:10.1046/j.1365-8711.2003.06897.x

Bullock J. S., Dekel A., Kolatt T. S., Kravtsov A. V., Klypin A. A., Porciani C., Primack J. R., 2001, ApJ, 555, 240

Cao T.-W., Wu H., Du W., Lei F.-J., Zhu M., Wouterloot J., Parsons H., et al., 2017, AJ, 154, 116

Catelan P., Theuns T., 1996, MNRAS, 282, 455

Catelan P., Theuns T., 1996, MNRAS, 282, 436

Ceccarelli L., Herrera-Camus R., Lambas D. G., Galaz G., Padilla N. D., 2012, MNRAS, 426, L6

Cervantes-Sodi B., Hernández X., 2009, RMxAA, 45, 75

Cervantes-Sodi, B., Hernandez, X., Park, C., et al. 2011, ApJL, 735, L25

Cervantes-Sodi, B., Li, C., Park, C., & Wang, L. 2013, ApJ, 775, 19

Cervantes Sodi, B., & Sánchez García, O. 2017, ApJ, 847, 37

Chabrier G., 2003, PASP, 115, 763

Chambers K. C., Magnier E. A., Metcalfe N., Flewelling H. A., Huber M. E., Waters C. Z., Denneau L., et al., 2016, arXiv, arXiv:1612.05560

Cisternas M., Jahnke K., Inskip K. J., Kartaltepe J., Koekemoer A. M., Lisker T., Robaina A. R., et al., 2011, ApJ, 726, 57

Contini E., Gu Q., Kang X., Rhee J., Yi S. K., 2019, ApJ, 882, 167

Crain R. A., et al., 2015, MNRAS, 450, 1937

Dalcanton, J. J.,et al. 1997, ApJ, 482, 659

Das M., O'Neil K., Vogel S. N., McGaugh S., 2006, ApJ, 651, 853

Das A., Pandey B., Sarkar S., 2022, arXiv, arXiv:2209.14194

Davis M., Peebles P. J. E., 1983, ApJ, 267, 465.

Davis M., Efstathiou G., Frenk C. S., White S. D. M., 1985, ApJ, 292, 371

de Blok, W. J. G., & van der Hulst, J. M. 1998, A&A, 335, 421

de Blok, W. J. G., & van der Hulst, J. M. 1998, A&A, 336, 49

de Blok W. J. G., McGaugh S. S., Rubin V. C., 2001, AJ, 122, 2396

De Lucia G., Blaizot J., 2007, MNRAS, 375, 2

de Vaucouleurs G., 1959, *Handbuch der Physik*, 53, 311

de Vaucouleurs G., de Vaucouleurs A., Corwin H. G., Buta R. J., Paturel G., Fouque P., 1991

Di Cintio A., Brook C. B., Dutton A. A., Macciò A. V., Stinson G. S., Knebe A., 2014, MNRAS, 441, 2986

Di Cintio A., Brook C. B., Macciò A. V., Dutton A. A., Cardona-Barrero S., 2019, MNRAS, 486, 2535

Diemer B., et al., 2018, ApJS, 238, 33

Diemer B., et al., 2019, MNRAS, 487, 1529

Di Matteo T., Springel V., Hernquist L., 2005, Natur, 433, 604

Disney M. J., 1976, Natur, 263, 573

Dolag K., Borgani S., Murante G., Springel V., 2009, MNRAS, 399, 497

Doroshkevich A. G., 1970, Afz, 6, 581

Doroshkevich A. G., Fong R., Gottlober S., Mucket J. P., Muller V., 1997, MNRAS, 284, 633

Du, W., Wu, H., Lam, M. I., et al. 2015, AJ, 149, 199

Dubois Y., Devriendt J., Slyz A., Teyssier R., 2012, MNRAS, 420, 2662

Dubois Y., et al., 2014, MNRAS, 444, 1453

Duckworth C., Tojeiro R., Kraljic K., 2020, MNRAS, 492, 1869

Duckworth C., Starkenburg T. K., Genel S., Davis T. A., Habouzit M., Kraljic K., Tojeiro R., 2020, MNRAS, 495, 4542

Eckert D., Gaspari M., Gastaldello F., Le Brun A. M. C., O'Sullivan E., 2021, Univ, 7, 142

Efstathiou G., Barnes J., 1984, ASIC, 117, 361

Einasto J., 1965, TrAlm, 5, 87

Einasto M., 1991, MNRAS, 250, 802

Fall, S. M., & Efstathiou, G. 1980, MNRAS, 193, 189

Fall, S. M. 1983, Internal Kinematics and Dynamics of Galaxies, 100, 391

Fall, S. M., & Romanowsky, A. J. 2013, ApJL, 769, L26

Few C. G., Courty S., Gibson B. K., Kawata D., Calura F., Teyssier R., 2012, MNRAS, 424, L11

Freeman, K.C. 1970, ApJ, 160, 811

Friedli D., Benz W., 1993, A&A, 268, 65

Galaz G., Cortés P., Bronfman L., Rubio M., 2008, ApJL, 677, L13

Galaz, G., Herrera-Camus, R., Garcia-Lambas, D., & Padilla, N. 2011, ApJ, 728, 74

Gamow G., 1952, PhRv, 86, 251

Genel S., et al., 2014, MNRAS, 445, 175

Genel, S., Fall, S. M., Hernquist, L., et al. 2015, ApJL, 804, L40

Genel S., Nelson D., Pillepich A., Springel V., Pakmor R., Weinberger R., Hernquist L., et al., 2018, MNRAS, 474, 3976

Gnedin N. Y., Kravtsov A. V., 2011, ApJ, 728, 88

Goh T., Primack J., Lee C. T., Aragon-Calvo M., Hellinger D., Behroozi P., Rodriguez-Puebla A., et al., 2019, MNRAS, 483, 2101

Gurovich S., McGaugh S. S., Freeman K. C., Jerjen H., Staveley-Smith L., De Blok W. J. G., 2004, PASA, 21, 412

Gupta A., Tran K.-V., Pillepich A., Yuan T., Harshan A., Rodriguez-Gomez V., Genel S., 2021, ApJ, 907, 95

Häring N., Rix H.-W., 2004, ApJL, 604, L89

Haynes M. P., Giovanelli R., Martin A. M., Hess K. M., Saintonge A., Adams E. A. K., Hallenbeck G., et al., 2011, AJ, 142, 170

Haynes M. P., Giovanelli R., Kent B. R., Adams E. A. K., Balonek T. J., Craig D. W., Fertig D., et al., 2018, ApJ, 861, 49

Hearin A. P., Campbell D., Tollerud E., Behroozi P., Diemer B., Goldbaum N. J., Jennings E., et al., 2017, AJ, 154, 190

Henden N. A., Puchwein E., Sijacki D., 2020, MNRAS, 498, 2114

Hernandez, X. & Cervantes-Sodi B. 2006, MNRAS, 368, 351

Hernandez, X., & Gilmore, G. 1998, MNRAS, 294, 595

Hinshaw G., et al., 2013, ApJS, 208, 19

Hinz, J. L., Rieke, M. J., Rieke, G. H., et al. 2007, ApJ, 663, 895

Hohl F., 1971, ApJ, 168, 343

Honey, M., Das, M., Ninan, J. P., & Manoj, P. 2016, MNRAS, 462, 2099

Hopkins P. F., Cox T. J., Younger J. D., Hernquist L., 2009, ApJ, 691, 1168

Hoyle F., 1951, *Problems of Cosmical Aerodynamics*, International Union of Theoretical and Applied Mechanics, and International Astronomical Union, p. 195

Huang, S., Haynes, M. P., Giovanelli, R., & Brinchmann, J. 2012, ApJ, 756, 113

Huang, S., Haynes, M. P., Giovanelli, R., et al. 2014, ApJ, 793, 40

Hubble E. P., 1926, ApJ, 64, 321.

Huchra J., Davis M., Latham D., Tonry J., 1983, ApJS, 52, 89

Impey C. D., Sprayberry D., Irwin M. J., Bothun G. D., 1996, ApJS, 105, 209

Impey, C., & Bothun, G. 1997, ARA&A, 35, 267

Jackson R. A., Martin G., Kaviraj S., Ramsøy M., Devriendt J. E. G., Sedgwick T., Laigle C., et al., 2021, MNRAS.tmp. doi:10.1093/mnras/stab077

Jiang F., Dekel A., Kneller O., Lapiner S., Ceverino D., Primack J. R., Faber S. M., et al., 2019, MNRAS, 488, 4801

Jimenez, R., Padoan, P., Matteucci, F., et al. 1998, MNRAS, 299, 123

Jones M. G., Bennet P., Mutlu-Pakdil B., Sand D. J., Spekkens K., Crnojević D., Karunakaran A., et al., 2021, ApJ, 919, 72

Katz N., Weinberg D. H., Hernquist L., 1996, ApJS, 105, 19

Kazantzidis S., Abadi M. G., Navarro J. F., 2010, ApJL, 720, L62

Kennicutt R. C., 1989, ApJ, 344, 685

Kim, J. & Lee, J. 2013, MNRAS, 432, 1701

Kimm, T., Devriendt, J., Slyz, A., et al. 2011, arXiv:1106.0538

Klypin A., Yepes G., Gottlöber S., Prada F., Heß S., 2016, MNRAS, 457, 4340

Koda J., Yagi M., Yamanoi H., Komiyama Y., 2015, ApJL, 807, L2

Kulier A., Galaz G., Padilla N. D., Trayford J. W., 2020, MNRAS, 496, 3996

Kuutma T., Poudel A., Einasto M., Heinämäki P., Lietzen H., Tamm A., Tempel E., 2020, A&A, 639, A71

Kuzio de Naray, R., McGaugh, S. S., & de Blok, W. J. G. 2004, MNRAS, 355, 887

Kuzio de Naray, R., & Spekkens, K. 2011, ApJL, 741, L29

Laganá T. F., Ulmer M. P., 2018, MNRAS, 475, 523

Lee J., Yi S. K., Elahi P. J., Thomas P. A., Pearce F. R., Behroozi P., Han J., et al., 2014, MNRAS, 445, 4197

Lelli F., McGaugh S. S., Schombert J. M., 2016a, ApJL, 816, L14

Lelli F., McGaugh S. S., Schombert J. M., 2016b, AJ, 152, 157

Li H., Mao S., Emsellem E., Xu D., Springel V., Krajnović D., 2018, MNRAS, 473, 1489

Lim, S. H., Mo, H. J., Wang, H., & Yang, X. 2016, MNRAS, 455, 499

Lutz K. A., Kilborn V. A., Catinella B., Koribalski B. S., Brown T. H., Cortese L., Dénes H., et al., 2017, MNRAS, 467, 1083

Lutz K. A., Kilborn V. A., Koribalski B. S., Catinella B., Józsa G. I. G., Wong O. I., Stevens A. R. H., et al., 2018, MNRAS, 476, 3744

Lu S., Xu D., Wang S., Cai Z., He C., Xu C. K., Xia X., et al., 2022, MNRAS, 509, 2707

Martizzi D., Faucher-Giguère C.-A., Quataert E., 2015, MNRAS, 450, 504

Marleau F. R., Habas R., Poulain M., Duc P.-A., Müller O., Lim S., Durrell P. R., et al., 2021, A&A, 654, A105

Marshall M. A., Shabala S. S., Krause M. G. H., Pimbblet K. A., Croton D. J., Owers M. S., 2018, MNRAS, 474, 3615

Martin G., et al., 2019, MNRAS, 485, 796

Martinez-Valpuesta I., Shlosman I., Heller C., 2006, ApJ, 637, 214

Matthee J., Schaye J., Crain R. A., Schaller M., Bower R., Theuns T., 2017, MNRAS, 465, 2381

Matthews L. D., Gao Y., 2001, ApJL, 549, L191

Matthee J., Schaye J., 2019, MNRAS, 484, 915

McAlpine S., et al., 2016, A&C, 15, 72

McGaugh S. S., Bothun G. D., Schombert J. M., 1995, AJ, 110, 573

McGaugh, S. S., Bothun, G. D., & Schombert, J. M. 1995, AJ, 109, 2019

McGaugh S. S., de Blok W. J. G., 1998, ApJ, 499, 41

McGaugh S. S., Rubin V. C., de Blok W. J. G., 2001, AJ, 122, 2381

McGaugh S. S., 2021, SHPSA, 88, 220

Mihos J. C., Spaans M., McGaugh S. S., 1999, ApJ, 515, 89

Mishra H. D., Dai X., 2020, AJ, 159, 69

Mo H. J., Einasto M., Xia X. Y., Deng Z. G., 1992, MNRAS, 255, 382

Mo H. J., McGaugh S. S., Bothun G. D., 1994, MNRAS, 267, 129

Mo, H. J., Mao, S., & White, S. D. M. 1998, MNRAS, 295, 319

Mo H., van den Bosch F. C., White S., 2010, gfe..book

Navarro J. F., White S. D. M., 1993, MNRAS, 265, 271

Navarro J. F., Frenk C. S., White S. D. M., 1996, ApJ, 462, 563

Nelson D., et al., 2015, A&C, 13, 12

Nelson D., et al., 2018, MNRAS, 475, 624

Nilson, P. 1973. Uppsala general catalogue of galaxies. Acta Universitatis Upsaliensis. Nova Acta Regiae Societatis Scientiarum Upsaliensis - Uppsala Astronomiska Observatoriums Annaler, Uppsala: Astronomiska Observatorium, 1973.

O'Neil, K., Bothun, G. D., & Schombert, J. 2000, AJ, 119, 136

O'Neil K., Andreon S., Cuillandre J.-C., 2003, A&A, 399, L35

Pahre M. A., Ashby M. L. N., Fazio G. G., Willner S. P., 2004, ApJS, 154, 235

Pakmor R., Springel V., Bauer A., Mocz P., Munoz D. J., Ohlmann S. T., Schaal K., et al., 2016, MNRAS, 455, 1134

Park C., Lee J., Kim J., Jeong D., Pichon C., Gibson B. K., Snaith O. N., et al., 2022, ApJ, 937, 15

Peacock J. A., Smith R. E., 2000, MNRAS, 318, 1144

Pearson W. J., Wang L., Brough S., Holwerda B. W., Hopkins A. M., Loveday J., 2021, A&A, 646, A151

Peebles P. J. E., 1969, ApJ, 155, 393

Peebles P. J. E., 1971, A&A, 11, 377

Peebles, P. J. E. 1980. *The Large-Scale Structure of the Universe*, by Phillip James Edwin Peebles. Princeton University Press, 1980

Pérez-Montaño L. E., Cervantes Sodi B., 2019, MNRAS, 490, 3772

Pérez-Montaño L. E., Rodriguez-Gomez V., Cervantes Sodi B., Zhu Q., Pillepich A., Vogelsberger M., Hernquist L., 2022, MNRAS, 514, 5840

Pickering, T.E., et al. 1997, AJ, 114, 1858

Pillepich A., et al., 2018, MNRAS, 475, 648

Pillepich A., Nelson D., Springel V., Pakmor R., Torrey P., Weinberger R., Vogelsberger M., et al., 2019, MNRAS, 490, 3196

Planck Collaboration, et al., 2016, A&A, 594, A13

Pontzen A., Governato F., 2012, MNRAS, 421, 3464

Rahman, N., Howell, J. H., Helou, G., Mazzarella, J. M., Buckalew, B. 2007, ApJ, 663, 908

Raichoor A., Andreon S., 2012, A&A, 537, A88

Reines, A. E. 2022. Nature Astronomy 6, 26–34

Roberts M. S., Haynes M. P., 1994, ARA&A, 32, 115

Rodriguez-Gomez V., Genel S., Vogelsberger M., Sijacki D., Pillepich A., Sales L. V., Torrey P., et al., 2015, MNRAS, 449, 49

Rodríguez-Gómez V., et al., 2016, MNRAS, 458, 2371

Rodriguez-Gomez V., et al., 2017, MNRAS, 467, 3083

Rodríguez-Gómez, V., Snyder, G. F., Lotz, J. M., et al. 2019, MNRAS, 483, 4140

Rodriguez-Gomez V., Genel S., Fall S. M., Pillepich A., Huertas-Company M., Nelson D., Pérez-Montaño L. E., et al., 2022, MNRAS, 512, 5978

Rodríguez-Puebla A., Behroozi P., Primack J., Klypin A., Lee C., Hellinger D., 2016, MNRAS, 462, 893

Romanowsky, A. J. & Fall, M. 2012, ApJ, 203, 17

Román J., Trujillo I., 2017, MNRAS, 468, 703

Rosas-Guevara Y., Bonoli S., Dotti M., Zana T., Nelson D., Pillepich A., Ho L. C., et al., 2020, MNRAS, 491, 2547

Rosenbaum, S. D., Krusch, E., Bomans, D. J., et al. 2009, A&A, 504, 807

Rubin V. C., 1954, PhDT

Saburova A. S., Chilingarian I. V., Kasparova A. V., Sil'chenko O. K., Grishin K. A., Katkov I. Y., Uklein R. I., 2021, MNRAS, 503, 830

Saburova A. S., Chilingarian I. V., Kulier A., Galaz G., Grishin K. A., Kasparova A. V., Toptun V., et al., 2022, arXiv, arXiv:2209.09906

Sahu N., Graham A. W., Davis B. L., 2019, ApJ, 887, 10

Sales L. V., Navarro J. F., Schaye J., Dalla Vecchia C., Springel V., Booth C. M., 2010, MNRAS, 409, 1541

Sales, L. V., Navarro, J. F., Theuns, T., et al. 2012, MNRAS, 423, 1544

Sales L. V., Navarro J. F., Peñafiel L., Peng E. W., Lim S., Hernquist L., 2020, MNRAS, 494, 1848

Salinas V. H., Galaz G., 2021, ApJ, 915, 125.

Schawinski K., Simmons B. D., Urry C. M., Treister E., Glikman E., 2012, MNRAS, 425, L61

Schaye J., et al., 2015, MNRAS, 446, 521

Schombert J. M., Bothun G. D., Schneider S. E., McGaugh S. S., 1992, AJ, 103, 1107

Schombert, J., Maciel, T., & McGaugh, S. 2011, Advances in Astronomy, 2011, 143698

Sellwood J. A., 2000, ASPC, 197, 3

Shlosman I., Frank J., Begelman M. C., 1989, Natur, 338, 45

Sijacki D., Springel V., Di Matteo T., Hernquist L., 2007, MNRAS, 380, 877

Smith, J. A., Tucker, D. L., Kent, S., et al. 2002, AJ, 123, 2121

Somerville R. S., Davé R., 2015, ARA&A, 53, 51

Sousbie T., 2011, MNRAS, 414, 350

Sousbie T., Pichon C., Kawahara H., 2011, MNRAS, 414, 384

Sparre M., Springel V., 2017, MNRAS, 470, 3946

Springel V., White S. D. M., Tormen G., Kauffmann G., 2001, MNRAS, 328, 726

Springel V., Hernquist L., 2003, MNRAS, 339, 289

Springel V., Hernquist L., 2005, ApJL, 622, L9

Springel V., Di Matteo T., Hernquist L., 2005, MNRAS, 361, 776

Springel V., White S. D. M., Jenkins A., Frenk C. S., Yoshida N., Gao L., Navarro J., et al., 2005, Natur, 435, 629

Springel V., White S. D. M., Jenkins A., Frenk C. S., Yoshida N., Gao L., Navarro J., et al., 2005, Natur, 435, 629

Springel V., 2010, MNRAS, 401, 791

Springel V., et al., 2018, MNRAS, 475, 676

Srisawat C., Knebe A., Pearce F. R., Schneider A., Thomas P. A., Behroozi P., Dolag K., et al., 2013, MNRAS, 436, 150

Stewart, K. R., Brooks, A. M., Bullock, J. S., et al. 2013, ApJ, 769, 74

Strauss M. A., Davis M., Yahil A., Huchra J. P., 1992, ApJ, 385, 421

Subramanian S., Ramya S., Das M., George K., Sivarani T., Prabhu T. P., 2016, MNRAS, 455, 3148. doi:10.1093/mnras/stv2500

Swaters R. A., Madore B. F., van den Bosch F. C., Balcells M., 2003, ApJ, 583, 732

Tacchella S., Diemer B., Hernquist L., Genel S., Marinacci F., Nelson D., Pillepich A., et al., 2019, MNRAS, 487, 5416

Tanoglidis D., Drlica-Wagner A., Wei K., Li T. S., Sánchez J., Zhang Y., Peter A. H. G., et al., 2021, ApJS, 252, 18

Teklu, A. F., Remus, R.-S., Dolag, K., et al. 2015, ApJ, 812, 29

Tempel E., Saar E., Liivamägi L. J., Tamm A., Einasto J., Einasto M., Müller V., 2011, A&A, 529, A53

Tolman, R. C. 1930. Proceedings of the National Academy of Science 16, 511–520.

Tolman, R. C. 1934. Relativity, Thermodynamics, and Cosmology. Relativity, Thermodynamics, and Cosmology, Oxford: Clarendon Press, 1934.

Tremmel M., Wright A. C., Brooks A. M., Munshi F., Nagai D., Quinn T. R., 2020, MNRAS, 497, 2786

Tully R. B., Fisher J. R., 1977, A&A, 54, 661

Übler H., Naab T., Oser L., Aumer M., Sales L. V., White S. D. M., 2014, MNRAS, 443, 2092

Velliscig M., Cacciato M., Schaye J., Crain R. A., Bower R. G., van Daalen M. P., Dalla Vecchia C., et al., 2015, MNRAS, 453, 721

Vogelsberger M., et al., 2014, MNRAS, 444, 1518

Vogelsberger M., Marinacci F., Torrey P., Puchwein E., 2020, NatRP, 2, 42

von Weizsäcker C. F., 1951, ApJ, 114, 165

Vorobyov, E. I., Shchekinov, Y., Bizyaev, D., et al. 2009, A&A, 505, 483

Wang H., Mo H. J., Jing Y. P., Yang X., Wang Y., 2011, MNRAS, 413, 1973

Wang L., Dutton A. A., Stinson G. S., Macciò A. V., Penzo C., Kang X., Keller B. W., et al., 2015, MNRAS, 454, 83

Weinberg M. D., 1985, MNRAS, 213, 451

Weinberger R., et al., 2017, MNRAS, 465, 3291

Wiersma R. P. C., Schaye J., Smith B. D., 2009, MNRAS, 393, 99

Wiersma R. P. C., Schaye J., Theuns T., Dalla Vecchia C., Tornatore L., 2009, MNRAS, 399, 574

White S. D. M., 1984, ApJ, 286, 38

White S. D. M., Frenk C. S., Davis M., Efstathiou G., 1987, ApJ, 313, 505

Wyder, T. K., Martin, D. C., Barlow, T. A., et al. 2009, ApJ, 696, 1834

Wright A. C., Tremmel M., Brooks A. M., Munshi F., Nagai D., Sharma R. S., Quinn T. R., 2021, MNRAS.tmp.

Yang X., Mo H. J., van den Bosch F. C., Weinmann S. M., Li C., Jing Y. P., 2005, MNRAS, 362, 711

Yang X., Mo H. J., van den Bosch F. C., Pasquali A., Li C., Barden M., 2007, ApJ, 671, 153

York D. G., Adelman J., Anderson J. E., Anderson S. F., Annis J., Bahcall N. A., Bakken J. A., et al., 2000, AJ, 120, 1579

Zavala, J., Frenk, C. S., Bower, R., et al. 2016, MNRAS, 460, 4466

Zehavi I., Zheng Z., Weinberg D. H., Blanton M. R., Bahcall N. A., Berlind A. A., Brinkmann J., et al., 2011, ApJ, 736, 59

Zhong, G. H., Liang, Y. C., Liu, F. S., et al. 2008, MNRAS, 391, 986

Zhu Q., et al., 2018, MNRAS, 480, L18

Zinger E., Pillepich A., Nelson D., Weinberger R., Pakmor R., Springel V., Hernquist L., et al., 2020, MNRAS, 499, 768.

Zjupa, J., & Springel, V. 2017, MNRAS, 466, 1625